Tail Bridging vs. Patchiness: Models for the Interaction of Nucleosomes

Dissertation
zur Erlangung des Grades

"Doktor der Naturwissenschaften"

am Fachbereich Physik
der Johannes Gutenberg-Universität
in Mainz

Frank Mühlbacher
geb. in Würzburg

Mainz, den 12. Juli 2004

Zusammenfassung

Diese Arbeit beschäftigt sich mit der Wechselwirkung von Nukleosomkernen (NCPs). NCPs repräsentieren die erste Hierarchiestufe in der räumlichen Organisation der Erbinformation in eukaryotischen Zellen. Ein NCP besteht aus einem Kern aus acht Histonproteinen und einem Abschnitt von DNA, der ca. zwei mal um den Kern gewickelt ist. Jedes Histon hat ein Endstück, das zwischen die Windungen der DNA hindurchreicht.

In der vorliegenden Studie wurde diesen Proteinschwänze besondere Aufmerksamkeit zuteil, da experimentelle Studien einen starken Einfluß dieser Schwänze auf die NCP Wechselwirkung vermuten lassen [1, 2]. In diesen Experimenten kann eine Änderung der Konfigurationen der Schwänze bei einer Änderung der Salzkonzentration beobachtet werden [1]. Für vergleichbare Werte der Salzkonzentration kann eine Anziehung zwischen den NCPs belegt werden [2]. Dieser Beobachtung könnten zwei verschiedene Mechanismen zugrunde liegen: Wechselwirkung von Multipolen oder Anziehung durch Brückenbildung zwischen den NCPs durch die Schwänze. Frühere Studien belegen, daß beide Effekte zu Anziehung führen können.

Die Modelle, die gegenwärtig zur theoretischen Beschreibung und für Computersimulationen von einzelnen NCPs benutzt werden, stellen wir kurz vor. Da diese Modelle sich auf die Beschreibung des Histonkerns und der gewickelten DNA beschränken und die Schwänze vernachlässigen, führen wir ein neues Simulationsmodell ein. Hier wird der Histonkern mit der DNA durch eine geladene Kugel, die Histonschwänze durch auf der Kugeloberfläche befestigte geladene Ketten dargestellt.

Zunächst untersuchen wir den Parameterraum eines einzelnen NCPs. Da die elektrostatische Wechselwirkung mit dem Debye-Hückel Potenzial modelliert wird, muß zuerst die effektive Ladung bestimmt werden, die die experimentellen Ergebnisse optimal reproduziert. Im weiteren Verlauf werden diese Werte benutzt, um die Paarwechselwirkung zweier NCPs mittels ausführlicher molekulardynamischer Studien zu untersuchen.

Weiterhin wird die Monomerverteilung für das neue Simulationsmodell untersucht. Ein Definitionskriterium für Brücken wird aufgestellt und die Existenz von Brücken zwischen zwei Nukleosomkernen gezeigt. Es wird auch bewiesen, daß die Monomere die Brückenbildung bzw. die Kondensation an einer der Oberflächen einem Aufenthalt zwischen den Kugeln vorziehen.

Indem man zwischen Konfigurationen unterscheidet, die Brücken aufweisen bzw. die keine Brückenbildung zeigen, kann schließlich bewiesen werden, daß die Brücken zwischen den Kugeln tatsächlich für die beobachtete Anziehung verantwortlich sind.

Unser neues Modell kann als Model zur Untersuchung der Acetylierung (Ladungsreduktion) der Histonschwänze dienen. Die Reduzierung des Ladungsanteils der Schwänze, führt zur Abschächung und sogar zum Verschwinden der Anziehung. Eine vor kurzem durchgeführte MC Studie [3] legt nahe, daß dieser Effekt für das Auffalten der Chromatinfaser im Fall von acetylierten Histonschwänzen verantwortlich ist. In diesem Fall wäre der Mechanismus, der von der Acetylierung der Histonschwänze bis hin zur Bildung von Heterochromatin und damit zur Inaktivierung grösserer Teile des Erbguts führt, ansatzweise verstanden.

Abstract

The subject of this thesis are the interactions between nucleosome core particles (NCPs). NCPs are the primary storage units of DNA in eucaryotic cells. Each NCP consists of a core of eight histone proteins and a strand of DNA, which is wrapped around about two times. Each histone protein has a terminal tail passing over and between the superhelix of the wrapped DNA. Special emphasis was placed on the role of these tails, since experimental findings suggest that the tails have a great influence on the mutual attraction of the NCPs [1, 2].

In those experiments Mangenot et al. observe a dramatic change in the configuration of the tails when a certain salt concentration is reached. For comparable values of the salt concentration they also find evidence of mutual attraction between NCPs. This effect could possibly be explained by two different interactions: Charge patchiness and tail induced interactions. We present former studies, showing that both effects are capable to yield attractive interactions.

We will then briefly review the existing models used in the theoretical approaches and in simulations concerning single NCPs. Since these models focus on the description of the histone core and the wrapped DNA, but neglect the histone tails, we introduce the multi chain complex as a new simulation model. Here the histone core and the wrapping DNA are modelled via a charged sphere, while the histone tails are represented by oppositely charged chains grafted on the sphere surface.

We start by investigating the parameter space describing a single NCP. Since the electrostatic interactions are modelled via the Debye-Hückel potential, we will first determine the value of the effective charge, which gives results closest to experimental data. These values are subsequently used for a study of the pair-interaction of two NCPs via an extensive Molecular Dynamics study.

Two further models, the patch model and the single chain model, are derived from the multi chain model in order to distinguish the contributions to the attraction coming from the interaction of the charge patches and the tails, respectively. The resulting interactions are analyzed and compared. For both models attraction is found, however the interaction differs considerably in range. While the patch interaction is short ranged, the tail interaction has a larger range, similar to the case of the full chain model.

The monomer distribution of the full chain model is investigated. A defining criterium for bridges is established and the existence of tail bridges between the cores is demonstrated. It is also shown, that the monomers favor bridging and condensation on the surface of the opposite core over residing in the space between both cores.

Finally, by discriminating between bridging and non-bridging configurations, it can be shown that the effect of tail bridging between the spheres does indeed account for the observed attraction.

The full chain model can serve as a model to study the acetylation of the histone tails of the nucleosome. The reduction of the charge fraction of the tails, that corresponds to the process of acetylation, leads to a reduction or even the disappearance of the attraction. This supports the findings of a recent MC study [3], that suggested this effect to be responsible for the unfolding of the chromatin fiber in the case of acetylated histone tails.

In this case the acetylation of the histone tails leads to the formation of heterochromatin, and one could understand how larger regions of the genetic information could be inactivated through this mechanism.

Contents

Contents

List of Figures

List of Figures

List of Figures

Introduction

Since the dawn of life on earth, the story of evolution is also a story of the storage and management of information. This information is stored in huge molecules inside the cells.

It is thought, that all present-day cells, and therefore all living organisms, descend from one single cell which lived about 3.5 to 4 billion years ago. However, there are no fossils tracing back to these early states of live, rendering all statements about it speculative. The main difference between these cells appearing in the earliest stages in evolution and modern simple cells is probably the storage system of the genetic information. It is thought that evolution started with families of ribonucleic acid (RNA) capable to catalyze their own replication. It seems likely, that RNA also guided the primordial synthesis of proteins. In this picture these primitive enzymes allowed a more efficient biosynthesis of the original RNA. The RNA created a tool, in form of the protein, in order to optimize its reproduction. This would have translated into an advantage over competing molecules in the competition about nucleotides, the building blocks of RNA. This advantage, in turn, resulted probably in a wider spread of this certain molecule with respect to its competitors. The information of the sequence, that made up the protein, was stored in the RNA molecule coded in a certain sequence of nucleotides. Already at this point in prebiotic evolution, the genetic information was constituted by the instructions regarding the protein synthesis.

Presumably, the first cells were formed by spontaneous assembly of phospholipid molecules enclosing self-replicating RNA. With time, these cells became more efficient and complex, requiring also a larger amount of genetic information. Therefore the length of the RNA molecule became bigger and bigger, increasing the risk of breakage or defective replication. Desoxyribonucleic acid (DNA) fitted better to the needs of such a cell and replaced RNA as a carrier of the hereditary material. All present-day cells use DNA as the storage media for the genetic information. DNA is found in cells, unlike RNA, principally in the double-stranded form, composed of a pair of complementary polynucleotides. This structure makes DNA more robust and stable than RNA. In addition, it is also relatively easy to replicate and allows a repair mechanism using the intact strand as a template to correct the damages. In this new and safer system, the DNA provides the repository of the genetic information. The importance of RNA shifted primarily towards providing a connection between the DNA, which took over the primary genetic function, and proteins, which became the major catalysts. The enzyme RNA polymerase (RNAP) catalyzes here the synthesis of RNA in accordance to the information provided by the DNA. The RNA in turn is used to synthesize the desired proteins.

Introduction

Since the media of the genetic information is fixed now, the question arises, how the huge amount of DNA can fit into the cell. For bacteria, which are the oldest organisms still existing today, this task is relatively easy: The size of a bacterium is about $1-3\ \mu$m and its DNA has a length of about 1 mm only. In this case it is sufficient to pack it into supercoils and keep it inside the cytoplasma of the cell.

In the case of eucaryotic cells, which make up all higher life forms like animals and plants, things are more complicated. One single molecule of eucaryotic DNA has typically a length of a few centimeters and would form a coil of roughly 100 μm diameter. However that DNA is always contained inside the nucleus, a compartment of a size of about 10-20 μm. Due to the considerable length of these molecules (humans have, for instance, 46 chains, the chromosomes, per cell making up 2 m of DNA), also the question arises, how the access to the information stored in the DNA can be efficiently managed. To answer this question, one has to know that information in a cell is stored in a hierarchically ordered manner, which can be compared to the way information is stored in a library. There the information is given by huge one-dimensional strings of letters - comparable to the long DNA molecule. A book like reference [5] contains about 3 km text, so a library with 10000 books stores approximately $3 \cdot 10^4$ km text. How is it possible, that a user finds the part of information he needs? By knowing some markers of the desired information this task is easy: One can go to the appropriate shelf, take out the book and open it on the required page. This way of hierarchically structured order allows to store a large amount of data on relatively small space providing high accessibility to it at the same time. The handling of information in the cell is quite similar: Here the lowest hierarchical level is the nucleosome being the principal storage unit for DNA. A nucleosome core consists of the nucleosome core particle (NCP) and about 50 bps of linker DNA connecting to the next core. The core particle consists of a protein core with 147 bps DNA wrapped approximately two times around and will be discussed at length in section 1.1.

The DNA-protein complex resulting from the agglomeration of core particles and linker DNA is called chromatin. It is known to form higher ordered structures. In the case of low salt concentration it can be described with a "beads-on-a-string" model with the nucleosome core particles as beads and the linker DNA as string. Since the "beads" have a diameter of about 10 nm it is also referred to as the "10-nm-fiber" [6]. At higher salt concentrations this fiber folds into a thicker fiber with a diameter of about 30 nm [7]. There is still no agreement on the precise geometry of this fiber: The solenoid models [6, 8, 9] assume helical ordered nucleosomes connected by bent linker DNA. Due to the persistence of DNA, this model requires strong nucleosome-nucleosome attraction to hold the structure together. In the zig-zag or crossed-linker models [10–14] core particles located at the opposite side of the fiber are connected by straight linkers. In order to describe the structure levels above the 30 nm fiber appropriately, more research needs to be done. Fig. I.1 illustrates the hierarchical structure of the ordering. On the left side the DNA molecule is shown. In the first step it is wrapped around the octamer histone core, forming the 10 nm fiber. The 10 nm fiber can be organized into the 30 nm fiber and structures of higher order until the level of the whole chromosome is reached.
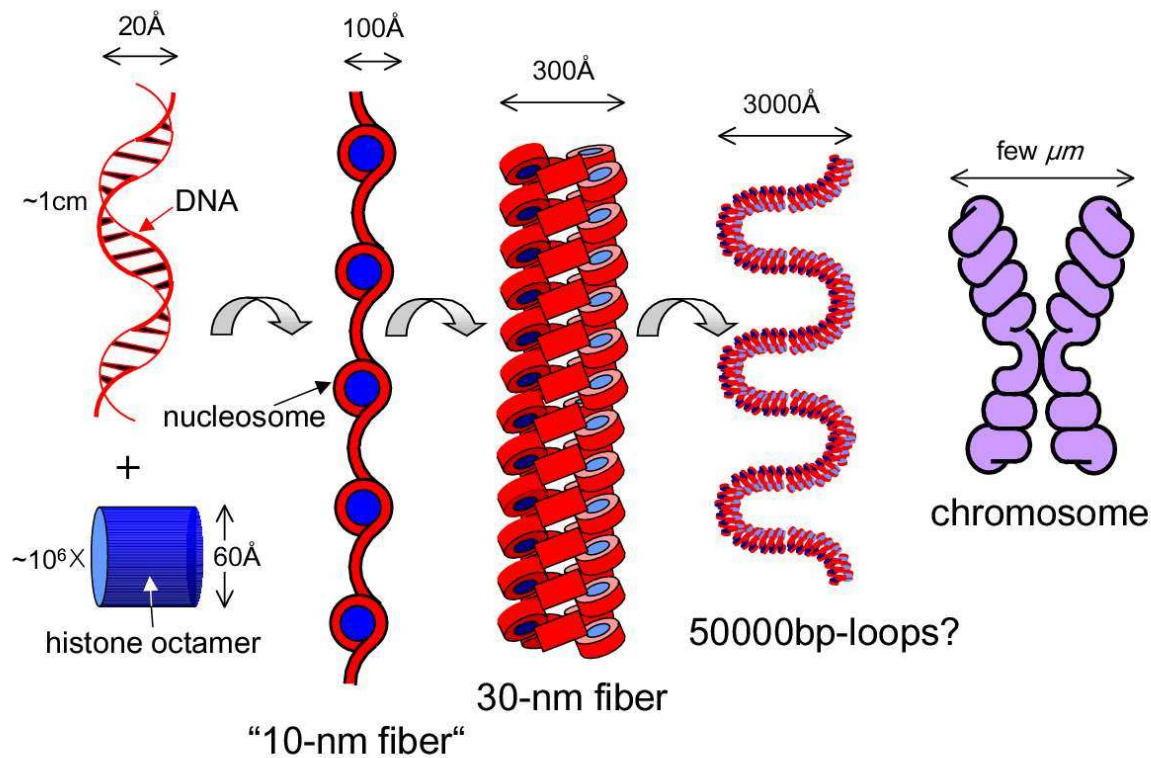
Figure I.1: Levels of organization of the DNA
From the left to the right the DNA gets compacted. The first step is the wrapping around the histone octamer giving rise to the 10 nm fiber. This fiber can be organized into the $30nm$ fiber and structures of higher order. In the chromosome a 10000 fold reduction of the size of the DNA molecule with an original contour length of about $1cm$ has been reached. (Taken from [15])

In a library, the user usually knows, for what information he is looking for. In the case of the genetic information, the 'user' comparable to the person looking for information in the library, is the RNAP molecule, which indiscriminately reads out information stored on the DNA. In order to regulate the use of the genetic information, the cell can prevent parts of the genome to be read out. Different ways of gene regulation are available to switch off either single genes or larger regions of chromatin [16].

In some cases the transcription of individual genes is suppressed by gene regulatory proteins. Typically these proteins bind to specific DNA sequences located close to the RNAP start site. In the case of prokaryotic cells, i.e. cells without a nucleus, the transcription is controlled by only one or two regulatory proteins. In eucaryotic cells this kind of gene regulation is much more complex, commensurate with the larger genom size and the large variety of cell types. For example the genom of Drosophila eve, a fruit fly, has binding sites for over 20 regulatory proteins. Some of these proteins activate transcription, while others repress it. These proteins can bind to special regulatory

sequences which are organized in a series of regulatory modules distributed along the DNA.

While single genes can be regulated using these regulatory proteins, also large sections of the genome can be switched off, using other means of regulation. Despite the fact, that nucleosomes do usually not present a serious obstacle to RNAP, higher-order DNA packaging plays a crucial role in the gene expression of eucaryotes [16]. In living cells the chromatin fiber is an extremely heterogeneous nucleoprotein filament. This heterogeneity also influences the structural characteristics of chromatin.
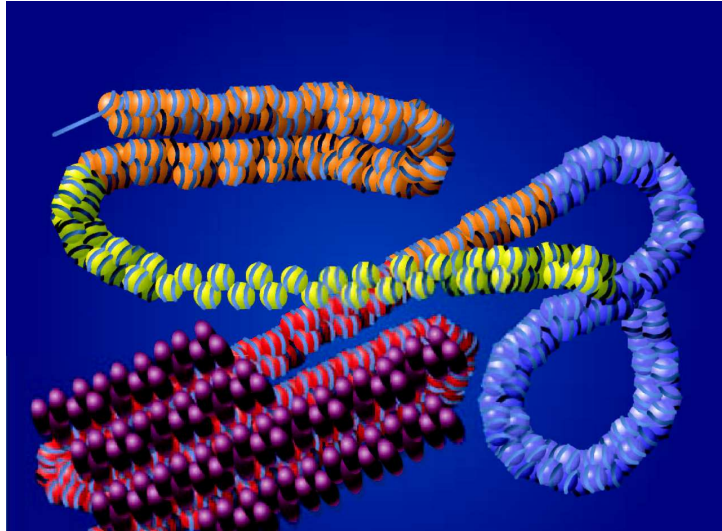
Figure I.2: Chromatin fiber heterogeneity

In vivo the chromatin fiber is extremely heterogeneous. Only decondensated parts of the fiber, shown by yellow nucleosomes in the figure, contain accessible information. The red, purple and blue regions correspond to condensation due to interactions with proteins and modifications of the histone proteins. (Taken from [17])

Fig. I.2 illustrates different conformations of the fiber due to biochemical histone modifications or the presence of nonhistone proteins. In this figure only the yellow nucleosomes form a filament containing active DNA. The other regions of the fiber are deactivated due to interactions with proteins and modifications of the histone proteins.[1]

In general chromatin can be classified into two cases: Heterochromatin, where the fiber is highly condensed, and euchromatin, where the fiber is less condensed. Active chromatin is always euchromatin. Facing the importance of chromatin condensation

---

[1]The yellow nucleosomes belong to a highly acetylated part of the chromatin fiber. In case of low acetylation or the presence of additional linker histones condensation can be observed, as it is shown by the orange part of the fiber. Regions which are deacetylated and methylated recruit nonhistone proteins that nucleate specialized structural domains. This kind of conformation can be found in the centomeric heterochromatin and is represented by the red part of the fiber with the purple proteins attached. In the blue region the histone protein H2A is replaced by H2AZ, producing a fully condensed 30-nm fiber.

with respect to gene regulation, the question about the reason for the condensation of chromatin arises. The mechanisms accountable for the formation of heterochromatin are not understood.

A recent MC study of the 30 nm fiber [3] suggests that the conformational properties of chromatin can be strongly affected by the interactions between the nucleosome cores. In the model used for these simulations, the NCPs are treated as flat cylinder objects with excluded volume and a short ranged attractive potential. The NCPs are connected via semiflexible and twistable linker DNA in the crossed linker fashion. By tuning the attractive potential to a minimal value of about -4 kT between the NCPs, a folding of the straight fiber into hairpins can be observed. In this conformation the NCPs are condensed at high densities at the expense of the fiber forming a tight loop. Similar loops can be observed in in vitro experiments [17, 18].
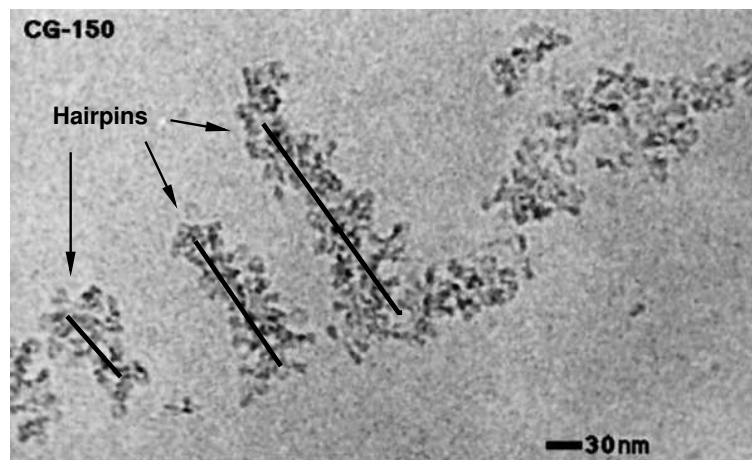
Figure I.3: Hairpins observed by cryoelectron microscopy
The image shows several regions of highly compacted chromatin. Apparently the fiber is condensed on itself forming a hairpin. (Taken from [18])

Fig. I.3 shows an image of highly compacted chromatin fibers forming a hairpin obtained with cryoelectron microscopy. The nucleosomes forming the fiber can be clearly distinguished.

For the cell it is most likely impossible to read the information stored on such a condensed section of the fiber, it is 'switched off' [17,19]. Such information management might explain phenomena like gene silencing. In a larger context they also have impact on the so-called epigenetics. This field deals with gene-regulating activity that does not involve changes of the DNA but persists through more than one cell generation [20, 21]. As we saw, mutual interactions between NCPs can lead to highly compacted configurations of chromatin [3], which can also be seen in experiments [18]. Furthermore chromatin in the compacted state is inactive. This compactification is used in cells to inactivate large regions of chromatin [16]. Consequently there seems to be a direct connection between the interaction between NCPs and the regulation of large gene

sequences. It is therefore crucial to reach a theoretical understanding of the interaction between NCPs, which is the subject of this thesis.

We will investigate the pair interaction, especially the attraction, of two isolated nucleosome core particles. In order to do so, the structure of the core histones has to be taken properly into account. Each histone protein consists of three regions: The histone-fold regions, diverse extensions therefrom and, most importantly, the histone tails. These tails, conserved throughout evolution [16], are highly flexible and relatively highly charged chains containing many lysines. As we will show, these tails are the main ingredient of the interaction between NCPs.

1 Experimental facts on NCPs

1.1 The nucleosome core particle

As already mentioned in the introduction, the principal packaging unit of DNA is the nucleosome core particle. The nucleosome core particle consists of the histone core, forming a cylinder of approximately 57 Å height and 105 Å diameter, and a strand of DNA wrapped around [22, 23]. Two of each of the histone proteins H2A, H2B, H3 and H4 form the core. These central proteins form crescent-shaped heterodimers in the pairings H3-H4 and H2A-H2B. These four dimers are arranged in the way H2A-H2B, H3-H4, H3-H4, H2A-H2B defining the path of the DNA: A left-handed helical ramp of 147 bp length and 1.7 turns. Each of the eight histone proteins also carries one highly flexible N-terminal amino tail [24–26]. These tails are lysine rich polypeptide chains with neutral and positively charged side groups.

In order to reveal the structure of this complex, X-ray crystallography has been employed. In 1997 a X-ray crystallography study by Luger et al. at a resolution of 2.8 Å succeeded to determine the structure of the nucleosome core particle in atomic detail [23]. The NCPs used here were obtained by assembling human DNA and histone proteins made in bacteria from transcription DNA of the African clawed frog (Xenopus laevis).

Fig. 1.1 shows the structure of the NCP presented in that study. The eight core histone proteins can be clearly distinguished. The coloring gives information about the protein identity: Yellow corresponds to H2A, red to H2B, blue to H3 and green to H4. The two strands of DNA wrapped around the protein core are also clearly visible and colored brown and turquoise respectively.

A protein is a chain of amino acids. The sequences of the histone core proteins and their tail regions are presented in fig. 1.2. The upper half of the figure shows the sequences of the core regions, according to the labels on the left side of the illustration. The lower half of the figure presents the histone fold extensions and the histone tails. The histone tails, which are not part of the core region, but reach out of the structure, are printed in italic. Each letter corresponds to an amino acid, the formulas and names of the amino acids can be found in biology textbooks, such as reference [16]. Some of the side chains of the amino acids carry charges. Lysine, arginine and histidine, which are represented here by the letters "K","R" and "H" respectively, carry one positive elementary charge. Aspartic acid and glutamic acid, represented by "D" and "E", carry one negative elementary charge. However in the case of the histone proteins, these charges are not necessarily dissociated in solution. The behavior of NCPs in solution with respect to the dissociation was studied by Khrapunov [27] and will be shortly discussed later.
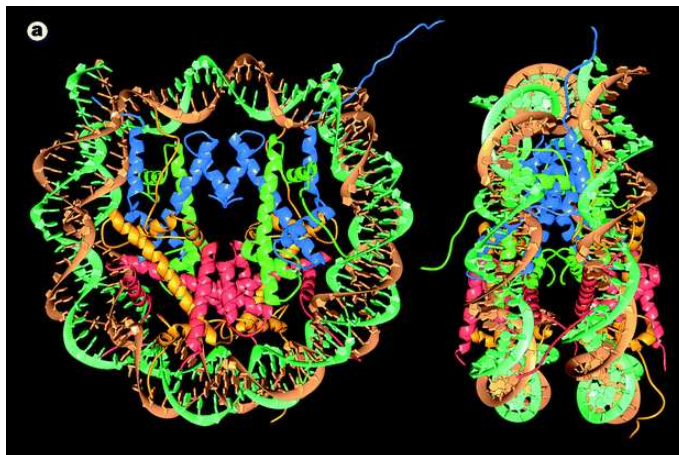
Figure 1.1: X-ray crystal structure of the nucleosome core particle
The eight histone proteins (yellow: H2A, red: H2B, blue: H3, green: H4)
and the wrapped DNA strands (brown/turquoise). Due to the low electron
density for the tails, most tail structures are not included in the picture.
(Taken from [23])

Sites featuring acetylation in living cells are indicated with the letter "a". The core histone name is representing the corresponding core histone region. Regions which are shaded gray were not included in the atomic model represented in fig. 1.1. Here the X-ray crystallography could not be interpreted, since the electron density was too low resulting in weak contrast.

However, in the next section we will describe, how the conformation of the tails can be investigated in dilute solutions. As we already mentioned above, the proteins and the DNA form a flat cylinder, with the diameter being twice the height.

The histone octamer contains 220 cationic arginine and lysine residues. About 117 residues are included in the globular histone domains, while the remaining 103 residues are located on the unfolded histone tails [27]. Using NMR-spectroscopy [28] and chemical modifications [29], it has been shown, that 86 cationic residues belonging to the globular domain are involved in intra- and interprotein ionic interactions and are therefore not exposed to the solvent. The remaining 31 cationic residues dissociate and constitute the net charge of the globular region. In order to get the overall charge of the nucleosome core, the wrapped DNA has to be taken into account. Each bp carries a negative charge of 2 due to the phosphates. Typically around 150 bps are wrapped around the histone octamer, resulting in a negative charge of about 300. Subtracting the protein charges, one gets a negative net charge of the core of about 270.

This charge inversion can also be observed for simple NCP models that describe the complex by a uniformly charged sphere with a semiflexible chain carrying an opposite charge wrapped around. Section 2.1.1 explains the charged sphere-polyelectrolyte chain model and deals with the effect of charge inversion. This simple model of a charged sphere and a oppositely charged chain can explain partly the condensation of the DNA

Figure 1.2: Core histone sequences and NCP
The upper half shows the sequences of the folded histone core regions as labelled on the left side. The lower half shows the histone fold extensions and the histone tails. Each letter corresponds to an amino acid, structure and names can be found in reference [16]. More details can be found in the text. (Taken from [23])

on the histone core. However there are still specific binding sites between the DNA and the core histones [23]. The shape of the core histones and their relative position to each other also defines the path of the wrapping DNA [23].

1.2 Configurational changes of the tails

This section is devoted to the configurational changes of NCPs induced by changes of the salt concentration. In a crystal the tails are fixed and embedded in the crystal structure. In order to observe effects, in which the tails are involved, one has to investigate a dilute solution of NCPs.

The interesting length scale is here no longer the atomistic scale, as in the case of the revelation of the histone core structure described in the previous section, but the overall size of the entire nucleosome core particle. In scattering, longer distances investigated correspond to smaller angles measured. Therefore for the measurements in the dilute solution small angle X-ray scattering (SAXS) was used [1].

Changing the salt concentration of the solution environment can change the configuration of the complex dramatically [1]. This is illustrated schematically in fig. 1.3: The left side shows a visualization of a NCP in low salt environment. The positive charged histone tails do have strong electrostatic interaction with the negative DNA strands.

Therefore they are condensed onto the core of the particle. However, with increasing salt concentration, the electrostatic interaction becomes screened. Now it is possible for the tails to separate from the core and form the extended configuration which is shown on the right hand side of the figure.
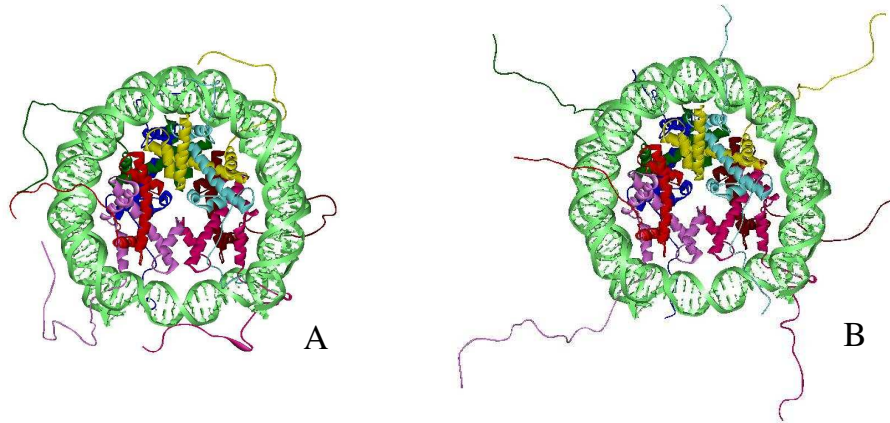
Figure 1.3: Regulation of the NCP configuration by the ionic strength 'Compact' configuration of the nucleosome core particle with condensed tails for low salt concentration (A) and 'extended' configuration for high salt concentration with the tails dangling in the solution (B) (Taken from [1])

The unfolding of the structure with increasing salt concentration can be detected by scattering experiments. Fig. 1.4 presents the maximal extension D_{max} of the distance distribution function obtained from X-ray scattering [1]. The lowest value for D_{max} of about 135 Å represents the extension of the structure in the compact state. The amplification of the size of the structure due to the separation of the tails at a certain salt concentration can be obtained by computing the difference between D_{max} corresponding to the actual salt concentration and the diameter of the compact state.

The filled symbols show the behavior for a complex with 145 bp of DNA wrapped around. Here an increase in the extension from about 135 Å at a salt concentration from 10 mM to a maximal extension of approximately 165 Å for salt concentrations larger than 50 mM can be observed. Increasing the salt content of the solution further towards the physiological ionic strength, which is at about 100 mM, does not have any significant impact on the measured diameter. Even for the further increase of the concentration until 200 mM, no change in the extension can be observed. A possible explanation for this behavior is the condensation of the tails on the core formed by the histone proteins and the wrapping DNA. With increasing salt concentration the tails are separating from the core as illustrated in fig. 1.3, resulting in a larger diameter of the structure. The empty symbols represent the case of a longer strand of DNA with 165 bps wrapped around the complex. According to the longer strands the overcharging is enhanced with respect to the former case. The observed diameter at a salt concentration of 50 mM

is about 139 Å and is much smaller than in the case of the weaker charged particle. This result suggests, that the unfolding of the tails is prevented by the higher negative core charge in this case. By increasing the salt concentration to 160 mM, also in the high charge case an enhanced diameter can be found. Apparently the screening is now strong enough to account for the separation of the tails from the core. The maximally measured extension of the complex, however, does not exceed the one obtained for the lower charged case.
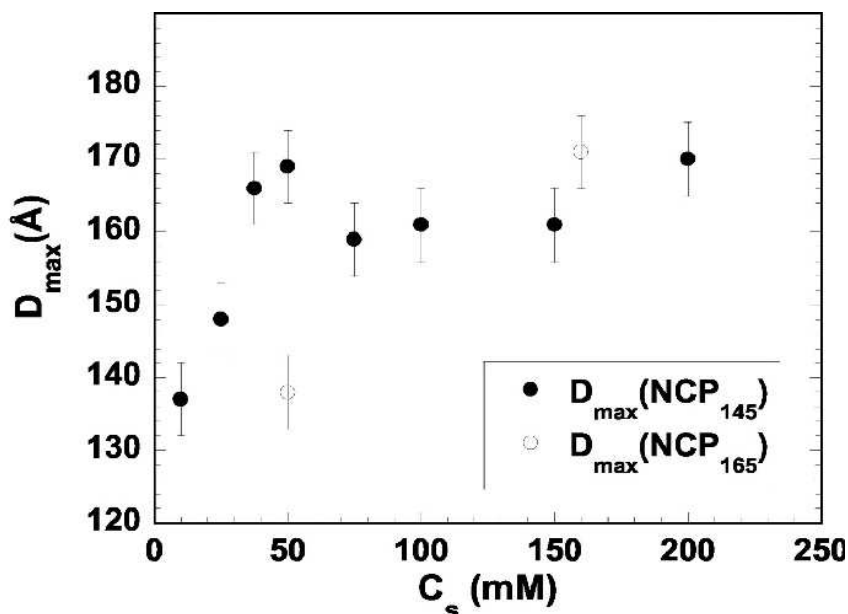
Figure 1.4: The diameter D_{max} of NCPs measured by X-ray scattering The filled symbol correspond to a NCP with 145 bp of DNA wrapped around. The value of D_{max} rises with increasing salt concentration to a maximum. In the case of a higher central charge, which is realized by using a core particle with 165 bp of DNA wrapped around (empty symbols), the increase in D_{max} starts at higher salt concentrations. The saturation value is not changed with respect to the former case. (Taken from [2])

1.3 Interaction of NCPs

As mentioned in the last section, the configuration of a nucleosome core particle varies with the salt concentration of the surrounding medium. This raises the question, whether this has also an impact on the interaction of two isolated NCPs.

This interaction can be inferred experimentally from the osmotic pressure Π. In a dilute solution of NCPs it can be written as a virial expansion:

$$\frac{\Pi}{RT} = \frac{C_{\mathrm{NCP}}}{M} + A_2 C_{\mathrm{NCP}}^2 + A_3 C_{\mathrm{NCP}}^3 + \ldots \tag{1.1}$$

Here R is the gas constant, M the molar mass of one NCP, C_{NCP} is the concentration of NCP and T the temperature. The factors A_i appearing in equation 1.1 are called the virial coefficients. The virial coefficient of order i is related to the interaction involving i particles at the same time. For dilute solutions the second virial coefficient represents the mutual effective interaction between two particles. Due to the dilution, the conjunction of more than two particles at the same time is very rare and can be neglected. In this case the virial expansion can be truncated after the second term. In the following, we will show experimental data for A_2 from reference [2]. An explanation of the methods used to obtain the second virial coefficient in this experiment can be found in Appendix A. Data from the experiment, which prove, that the interaction is indeed described correctly by the truncated expansion, can also be found in that appendix.

The experimental values of the second virial coefficient are shown in fig. 1.5 as a function of the salt concentration. The empty symbols correspond to a solution of NCPs. For low salt concentrations A_2 decreases monotonically with increasing salt content due to the increasing screening of the electrostatic interaction. When reaching the salt concentration $c_s = 80$ mM, A_2 decreases strongly to a minimum at $c_s \approx 180$ mM. For higher values of c_s A_2 rises again until it reaches a plateau at $c_s \approx 300$ mM.

The filled symbols represent the second virial coefficient for bare fragments of DNA with a length of 146 bps. In this case each interacting particle carries a higher charge, since it contains the same amount of negative charges from the DNA but no positively charged histone proteins. The higher charge leads to higher electrostatic repulsion resulting in a higher value of A_2 than in the NCP case. With increasing salt concentration A_2 monotonically decreases due to the screening. However, a drop in the second virial coefficient, as observed for nucleosome core particles, cannot be seen.

So not only the configurational state, but also the mutual interaction of nucleosome core particles depends strongly on the salt concentration. Due to the vicinity of the effect of unfolding from section 1.2 and the drop in A_2 with regard to the salt concentration, the question arises, whether there is a connection between these effects. In the next chapter we will propose possible models that might be capable to explain the observed attraction and give an outline how to explore this issue by the means of computer simulations.

Summary

This section presented experimental facts about the nucleosome core particle. The NCP consists of a core formed from one pair of each histone protein H2A, H2B, H3 and H4. Around the histone core a strand of DNA is wrapped about 2 times. The complex of histone core and DNA forms a cylinder of 57 Å height and 106 Å diameter decorated by eight highly flexible histone tails. Due to the high lysine content, these tails are charged positively. The histone proteins carry a positive charge, however, due to overcharging by the wrapped DNA, the NCP carries a negative net charge [23].

While the structure of the histone core with the wrapped DNA was studied by X-ray crystallography, the tail configurations were studied in dilute solutions of NCPs.
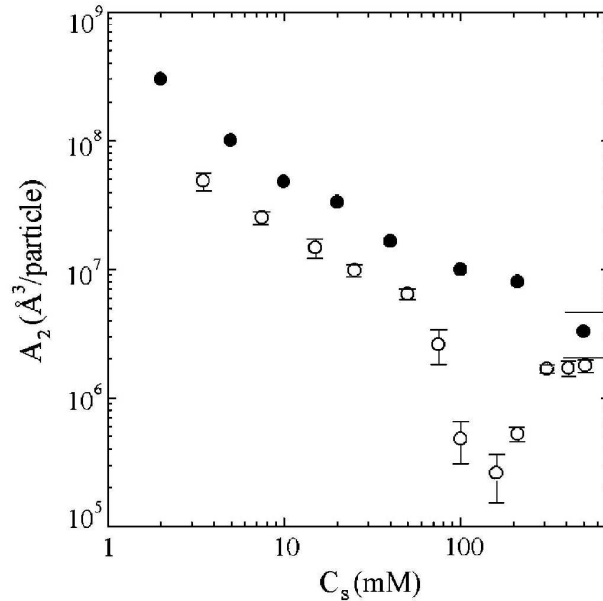
Figure 1.5: Comparison of the second virial coefficient of nucleosome core particles and of naked DNA fragments

This plot shows the second virial coefficient of NCPs and naked DNA fragments of a length of 146 bps as a function of the salt concentration. The data corresponding to the NCPs is represented by empty symbols, the data from the DNA fragments is shown with the full symbols. For naked DNA A_2 decreases monotonically with increasing salt concentration. In the case of NCPs A_2 shows a similar decrease up to a salt concentration of about 50 mM, where it is followed by a steep drop to a minimum at $c_s = 180$ mM. For higher salt concentrations the curve rises again to a plateau. (Taken from [2])

Dependent on the salt concentration, configurational changes can be observed for the tails of the NCP. At low salt concentrations the electrostatic interactions are only weakly screened. Therefore the positively charged tails condense onto the negatively charged surface of the core. By increasing the salt concentration, a separation of the tails from the core can be observed. Since the electrostatics are weaker in this case, thermal fluctuations can move the tails easier out of the interaction range of the cores. This results in an increase of the overall size of the NCPs [1].

For salt concentrations comparable to those, where this unfolding process can be observed, reduced repulsion between the NCPs can be detected. This effect turns also out to be dependent on the screening: At salt concentrations in the vicinity to the unfolding region, a steep drop in the second virial coefficient can be observed. For very high salt concentrations, the second virial coefficient rises again [2].

The vicinity of the observed drop in the second virial coefficient and the unfolding of the tail structure of the NCP raises the idea of a connection between both effects. A

possible explanation could be tail bridging between both complexes leading to mutual attraction. In the following, we will point out other mechanisms capable to explain the attraction observed and try to shed light on this question.

2 Theoretical and simulation models for NCPs

2.1 Models for a single NCP

For the interaction of DNA and the histone proteins, short range electrostatics plays an important role [30]. In this chapter we want to discuss analytical and simulation models that have been presented in the literature to describe the electrostatics in this system. A new model suitable for the investigation of the histone tails will be introduced.

2.1.1 Charged sphere chain models

A popular way of modelling NCPs is to represent them by some sort of chain-sphere complex. Here the histone core of the nucleosome is typically modelled by a sphere with a positive central charge that represents the charged histone proteins. The DNA is modelled as a (usually semiflexible) negatively charged polyelectrolyte. In order to lower its free energy, a section of the chain wraps around the sphere. Surprisingly the amount of wrapped chain is so large, that the negative polyelectrolyte charges typically outnumber the positive ball leading to a complex with a negative net charge [31–33].

This effect is similar to overcharging observed for a charged sphere in a solution containing multivalent counterions [34–37]. Here the reduction in the electrostatic energy of the counterions due to the condensation on the surface of the sphere outweighs the decrease in entropy. This behavior is due to correlation effects between the discrete charges [35]. The effects leading to charge inversion in the case of the charged sphere chain model are different ones and will be discussed in the following.

In the case of a highly charged chain, it was shown by theoretical studies and also by experiments that this effect can be understood by a counterion release mechanism [31,38–44]. Before complexation the highly charged chain carries condensed counterions [45]. When the chain condenses on the surface of the sphere, a fraction of these counterions is released into the solvent. The corresponding entropy increase can then lead to an overcharging of the complex beyond its isoelectric point [46, 47]. Charge inversion can also be observed, when the chain is only weakly charged [32, 33, 48, 49]. In order to explain the effect in this case, the condensation of the chain can be interpreted as a two step process [49, 50]. In the first step, chain fragments with a length of the order of the sphere radius condense randomly on the sphere surface. In the second step, these segments are reoriented and shifted in order to minimize their mutual electrostatic repulsion. The result is an equidistant coil with distance A between the turns. This leads to an additional contribution of the chain piece with a stripe on the sphere of the length of the chain section and of width A. By minimizing the energy

of this system with respect to the wrapping length, one finds a length, which is longer than the isoelectric length, where the chain charge equals the sphere charge. These correlation effects can outweigh the unfavorable deformation of the semiflexible chain.

The sphere polyelectrolyte model for the nucleosome core particle can also be extended to systems containing several spheres. In the highly charged case [47] as well as in the weakly charged case [50, 51] multi sphere complexes were found. Here several spheres were assumed to be linked by a single wrapping polyelectrolyte, similar to the case which is observed for the nucleosome core particles and the DNA. Fig. 2.1 depicts the pearl necklace structure formed by charged spheres and polyelectrolytes, which can serve as a model of artificial chromatin [50]. In experimental realizations
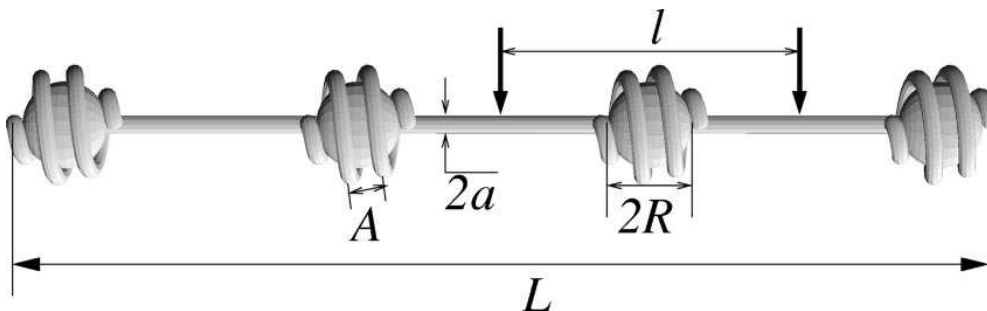
Figure 2.1: A model for artificial chromatin
In this model the histone octamers are represented by positive charges spheres while the DNA is modelled by a negative charged polyelectrolyte chain. (Taken from [50])

of artificial chromatin, spheres can be colloidal particles [52–54], micelles [55–57] or dendrimers [58, 59].

Apparently this chain-sphere model is suitable to describe some features of the interaction of the DNA and the histone core. The charged sphere-polyelectrolyte model is well established by now and also widely used as a basis for computer simulation [60–72].

2.1.2 NCPs and DiSCO

In order to provide a better description of the charge distributions of macromolecules suitable for simulations on the Debye-Hückel level, Beard and Schlick developed the DiSCO (Discrete Surface Charge Optimization) algorithm [73]. By solving the Poisson-Boltzmann equation (PBE) numerically, the authors obtain the electric field around a given macromolecule. In a second step they construct a virtual surface S around the macromolecule. The structural information about the NCP was obtained from the study from Luger [23]. The left side of fig. 2.2 shows the NCP and the surface laid around. It is composed of a large disc and a small cylinder: The disc encloses the main part of the particle, the cylinder encloses the part of one of the H3 histone tails, which could be resolved by the X-ray crystallography [23]. The other histone terminal

tails were also partly resolved. They were included in the main particle rather than modelled explicitly in this model.
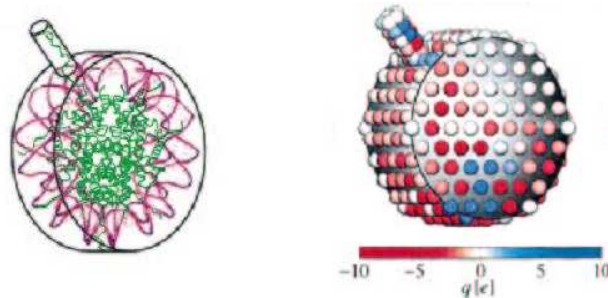
Figure 2.2: DiSCO surface and charge distribution
The DiSCO algorithm describes the NCP by using charges on a surface enclosing the particle. Here the surface is composed of a disc, containing the core formed from the histone proteins and the DNA, and a cylinder, modelling a part of the H3 histone tail explicitly, as shown on the left side. The right side shows the charge distribution resulting from the DiSCO algorithm. Here all charges of the NCP core are mapped on 277 charge patches located on the surface. Red charges correspond to negative charges, blue to positive charges. See the text for details on the DiSCO algorithm. (Taken from [73])

In the next step they define discrete charges on the surface S. The values of the charges are optimized in order to reproduce the electric field obtained by solving the PBE outside S. From the reference field obtained via the PBE, the renormalized charges are determined via the Debye-Hückel equation. The result of this process is a structure, which shall reproduce the electrical properties of the macromolecule, without the need of using a setup of the entire atomistic charge distribution.

The right side of fig. 2.2 shows the resulting charge distribution of the DiSCO algorithm for the NCP for a salt concentration of 50 mM [73]. Each patch on the surface corresponds to a charge as indicated on the legend below. The circular surface of the disc shows positive and negative charges while the disc margin is dominated by the DNA and is consequently charged negatively. The cylinder representing the stump of the H3 histone tail yields mainly positive charges due to the relatively high content of lysine and arginine groups.

This model was also used to construct a computer model of the 30 nm fiber [74]. Even though these authors achieve a high sophistication to describe the charged surface of the NCP, they fail to include in their model what is likely the most important ingredient: The flexible histone tails. Although they include the parts of the tails whose structure were resolved by Luger (which make up hardly half of the tails, as indicated in fig. 1.2), these parts are either included in the charge distribution of the main particle (in the case of both of the H2A,H2B and H4 and one of the H3 tail parts) or assumed to act like a stiff rod (in case of the remaining H3 tail part).

The left side of fig. 2.3 shows the electrostatic potential around a NCP at a salt concentration of 100 mM computed by using the DiSCO model. Red indicates a nega-
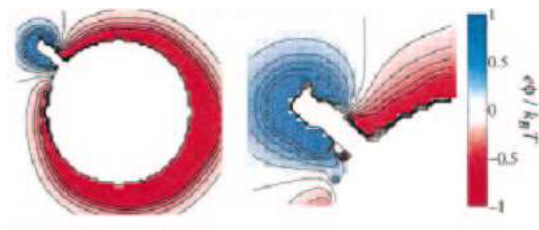
Figure 2.3: Electrostatic potential of the NCP obtained by DiSCO
The left side shows the potential around the structure shown on the right side of fig. 2.2. Around the main particle, the potential is mainly negative. The stump of the H3 histone tail apparently dominates the local potential. This suggests a considerable influence of the tails on the shape of the electrostatic potential, since the other tails also carry a relative high amount of positive charge [23]. The right side shows the H3 tail region in detail. (Taken from [73])

tive, blue a positive potential. The potential is found to be negative around the NCP, except in the region around the stump of the H3 histone tail. Here the positive charge of the tail dominates, leading to a positive potential. The right side shows the H3 tail region in detail. Apparently the stump of the H3 histone tail has considerable influence on the local potential. This result suggests, that an adequate description of the histone tails is necessary, when dealing with the electrostatics of the NCP.

Since the tails are the center of interest in this study, we have to establish a new model, which is more suitable for our needs. The new model will consist of a central spherical core containing the histone core and the wrapped DNA. Due to the effect of overcharging discussed here, this core will be charged negatively. Since we aim on the description of isolated NCPs in dilute solution, there will be no modelled linker DNA. The lysine rich histone tails will be mimicked by flexible polyelectrolytes grafted on the surface of the core particle. Evidently our model uses a very simple representation of the histone-DNA spool. We will show in this thesis that this representation is sufficient to reproduce essential features of the NCP-NCP interaction if the tails are included in the model.

2.1.3 Simulation model for NCP

Lennard-Jones units

In order to perform Molecular Dynamics (MD) simulations, it is necessary to define and fix several units for the further description of the setup and the results. As unit length $\sigma = 3.5$ Å is chosen, corresponding to the length of the lysine backbone which represents the repeat unit of the tails. The energy unit ϵ is set to the thermal energy $k_B T$. Dealing with electrostatics requires the definition of a unit charge, which was

chosen to be the negative elementary charge $e_0 = -1.6 \cdot 10^{-19}$ C. The Bjerrum length $l_B = e_0^2/4\pi\epsilon k_B T$ is the distance at which two unit charges have the interaction energy equal to kT. It has the value of approximately 7 Å in the case of water at room temperature. Since we have already defined the length scale σ, fixing the Bjerrum length to $l_B = 2\ \sigma$ also fixes the temperature. Time can be measured in units of $\tau = \sigma\sqrt{m/\epsilon}$. The definition of mass is not necessary since it would be only needed to compare τ to another system of units. The time step was set to 0.01 τ for all simulations presented in this work. To compare our results to experimental data, the Lennard-Jones units can be converted to the International System of Units. Assuming a temperature of 300 K, the energy unit kT translates to approximately $4 \cdot 10^{-21}J$. Consequently the unit of the force, kT/σ, is approximately 12 pN.

Setup of a NCP

The core particle is modelled as a sphere with radius a. This radius is chosen to be 15 σ. The volume of the sphere representing the core is then comparable to that of the NCP complex. In order to be able to identify the conditions where unfolding can happen, the spheres central charge Z was varied from 0 to 300. According to the results to be presented in chapter 3, $Z = 150$ was chosen for the further course of the study. The eight histone tails were modelled as flexible chains grafted on the surface of the sphere. Each chain consists of 30 monomers with every third carrying a positive charge of one, the rest being neutral. Here the model was fitted to the experimental data with respect to chain length and charge fraction. In order to fix the chains to the sphere, a shifted harmonic potential was applied between the grafted monomers and the center of the sphere. To stabilize the relative position of the grafted monomers to each other, each one was connected to its next neighbor via a shifted harmonic potential, such that they sit on the corner of a cube. The structures with the bonds stabilizing the relative positions of the chains is illustrated in fig. 2.4.

Creating the canonical ensemble

Molecular Dynamics (MD) can be used to obtain a statistical ensemble average by creating a sufficiently long trajectory through the phase space of the system. In order to be able to simulate a canonic ensemble, the purely deterministic Newtonian equations of motion have to be extended. In this work we choose to employ a Langevin thermostat [75]. This means, we have to solve the Langevin equation

$$m\ddot{r} = -\nabla V(r) - \Gamma\dot{r} + \xi(t). \tag{2.1}$$

Here r and m denote the position and the mass of a particle. $V(r)$ describes the potential, $-\Gamma\dot{r}$ represents the friction and $\xi(t)$ the random collisions of the surrounding medium. $\xi(t)$ is a δ- correlated Gaussian noise term with

$$\langle\xi\rangle = 0 \qquad \text{and} \qquad \langle\xi_i(t)\xi_j(t')\rangle = 6kT\Gamma\delta_{ij}\delta(t-t'). \tag{2.2}$$

ξ is adjusted via the fluctuation-dissipation theorem, for the simulations presented here Γ was set to $1\ \frac{\epsilon\cdot\tau}{\sigma^2}$. The Langevin dynamics can be formulated as a general Fokker-Planck process. The stationary state of this process will be the Boltzmann distribution [76].

Figure 2.4: Model for NCP

Eight polyelectrolyte chains are grafted on the surface of a charged sphere. The end monomers are connected to the core by harmonic bonds (lhs). To ensure the stability of the relative positions of the chains, the end monomers are also connected to the next neighbors by harmonic bonds (rhs).

Verlet integrator scheme

In order to carry out a MD simulation, we have to integrate the equations of motion. To obtain an algorithm suitable for this task, we start with a Taylor expansion of the coordinate r of a particle around the time t:

$$r(t + \Delta t) = r(t) + \dot{r}(t)\Delta t + \ddot{r}(t)\frac{\Delta t^2}{2} + \dddot{r}(t)\frac{\Delta t^3}{3!} + \mathcal{O}(\Delta t^4). \tag{2.3}$$

Equivalently we can write

$$r(t - \Delta t) = r(t) - \dot{r}(t)\Delta t + \ddot{r}(t)\frac{\Delta t^2}{2} - \dddot{r}(t)\frac{\Delta t^3}{3!} + \mathcal{O}(\Delta t^4). \tag{2.4}$$

By adding up the equations 2.4 and 2.4 and using the force $F(t) = \ddot{r}(t)m$, with m denoting the mass of the particle, we obtain

$$r(t + \Delta t) + r(t - \Delta t) = 2r(t) + \frac{F(t)}{2m}\Delta t^2 + \mathcal{O}(\Delta t^4) \tag{2.5}$$

or

$$r(t + \Delta t) \approx 2r(t) - r(t - \Delta t) + \frac{F(t)}{m}\Delta t^2. \tag{2.6}$$

This instruction constitutes the Verlet algorithm, which was used as integrator in the simulations. The calculation of the new position is accurate up to an order of Δt^4, where Δt is the time step applied in the simulation.

The velocity $v(t) = \dot{r}(t)$ of the particle can easily be computed by subtracting equation 2.4 from 2.3:

$$r(t + \Delta t) - r(t - \Delta t) = 2v(t) + \mathcal{O}(\Delta t^3) \tag{2.7}$$

$$v(t) = \frac{r(t + \Delta t) - r(t - \Delta t)}{2\Delta t} + \mathcal{O}(\Delta t^2) \tag{2.8}$$

The estimate of the velocity has an error of the order of Δt^2. The velocity will be used as an input in the Langevin thermostat described in the previous section. The force $F(t)$ from eq. 2.6 can then be written as

$$F(t) = -\nabla V(r) - \Gamma(v(t - \Delta t) + a(t - \Delta t)\Delta t) + \xi(t). \tag{2.9}$$

Interaction potentials

Lennard-Jones potential For the simulation of the hard core particles (i.e. the tail monomers and the spheres) a purely repulsive Lennard-Jones potential [77] was chosen, which is shown here for the case of the interaction between two tail monomers:

$$V_{\mathrm{LJ}}^{\mathrm{MM}}(r) = \begin{cases} 4\epsilon[(\frac{\sigma}{r})^{12} - (\frac{\sigma}{r})^6 + \frac{1}{4}] & \text{for } 0 < r \le r_{\mathrm{cut}}^{\mathrm{MM}} \text{ with } r_{\mathrm{cut}}^{\mathrm{MM}} = 2^{1/6}\,\sigma \\ 0 & \text{else} \end{cases} \tag{2.10}$$

The parameters ϵ and σ, characterizing the strength and extension of the potential, were chosen to be the basic units of energy and length in the previous paragraph. With respect to the plain Lennard-Jones potential, the potential used here is shifted and truncated. This is illustrated in fig. 2.5.
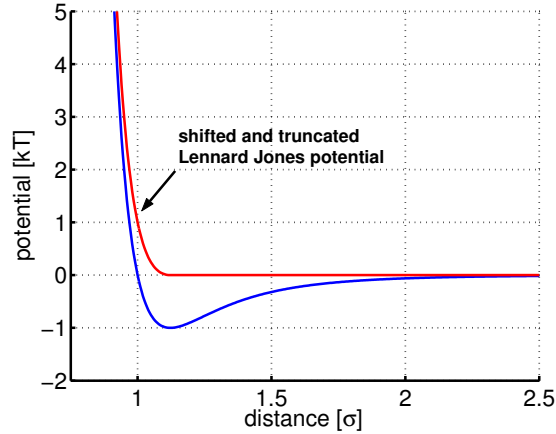
Figure 2.5: Lennard-Jones potential
The potential used in the simulation is represented by the red curve. With respect to the bare LJ potential, which is shown by the blue curve, it is shifted and truncated in order to ensure a smooth transition from the repulsive to the zero potential region.

The shift of the potential is necessary in order to obtain a purely repulsive potential. The potential is truncated at the minimum at $r_{min} = 2^{1/6}\ \sigma$ and has the value of zero beyond that point. Since the Verlet integrator uses the force as an input, which is obtained by differentiating the potential, the potential should be differentiable and should therefore not contain any kinks or jumps. By including the $-\left(\frac{\sigma}{r}\right)^6$ term and the truncation, a smooth transition from the repulsive to the zero region is achieved, which is in contrast to the use of a bare r^{-12} potential.

The interaction between a tail monomer and a core with the radius a can be described by a slight modification of equation 2.10. The potential has to be shifted to larger particle distances, in order to take the volume due to the extension of the core into account:

$$V_{\text{LJ}}^{\text{cm}}(r) = \begin{cases} 4\epsilon[(\frac{\sigma}{r-a})^{12} - (\frac{\sigma}{r-a})^6 + \frac{1}{4}] & \text{for } a < r \leq r_{\text{cut}}^{\text{cm}} \text{ with } r_{\text{cut}}^{\text{cm}} = 2^{1/6}\ \sigma + a \\ 0 & \text{else} \end{cases} \tag{2.11}$$

Since the positions of the cores are fixed in our simulations at distances larger or equal twice the core radius, excluded volume interaction between the cores has not to be taken into account.

Potentials of the grafting monomers In the multi chain model, the chains are located at fixed positions on the sphere surface. In order to keep these positions fixed, each chain has one end monomer grafted on the surface of the sphere. This grafting is realized by applying a shifted harmonic potential on the center of the core and each grafted monomer:

$$V_{\text{GRAFT}} = \frac{1}{2} * k_{\text{GRAFT}}(r - r_{\text{GRAFT}})^2 \tag{2.12}$$

r represents the distance between the grafting monomer and the core, k_{GRAFT} the spring constant. r_{GRAFT} is the core radius a. The bonds established by the grafting potentials between the chain ends and the core center are illustrated with black bars on the left hand side of fig. 2.4. k_{GRAFT} was choosen to be $2\ \epsilon/\sigma^2$.

An equivalent potential is also used in order to preserve the relative positions of the monomers amongst each other. It is applied between the next neighbors of the grafted monomers, resulting in a cube formed by the eight particles. This arrangement of the bonding potentials is presented on the right hand side of fig. 2.4. The functional form of the potential can be obtained by replacing the core radius r_{GRAFT} by the reference length r_{MATCH} of the edge of the cube and r by the distance between the involved next neighbors:

$$V_{\text{MATCH}} = \frac{1}{2} * k_{\text{MATCH}}(r - r_{\text{MATCH}})^2 \tag{2.13}$$

The value of k_{MATCH} is choosen to be $2\epsilon/\sigma^2$, r_{MATCH} is $\frac{2\sqrt{3}}{3}a \approx 17.3\ \sigma$.

FENE potential and effective potential for the monomers The bonding interactions of the neighboring monomers of the chains were modelled using the Finite Extendible Nonlinear Elastic (FENE) potential

$$V_{\text{FENE}} = -\frac{1}{2}\ k_{\text{FENE}}\ r_{\text{FENE}}^2\ \ln(1 - (\frac{r}{r_{\text{FENE}}})^2) \tag{2.14}$$

with k_{FENE} being the spring constant and r_{FENE} the maximal distance between two bonded monomers. The potential shows a singularity at this point. The values for the FENE parameters are $k_{\text{FENE}} = 7\,\epsilon/\sigma^2$ and $r_{\text{FENE}} = 2\,\sigma$.

In theoretical models, bonding potentials are mainly considered to be harmonic. However in the case of computer simulations, the FENE potential turned out to be preferable, since it contains the finite extension of the bonding length [78]. The Taylor expansion of the FENE potential yields a harmonic potential for small r, the deviation from a harmonic potential is of the order of r^4.
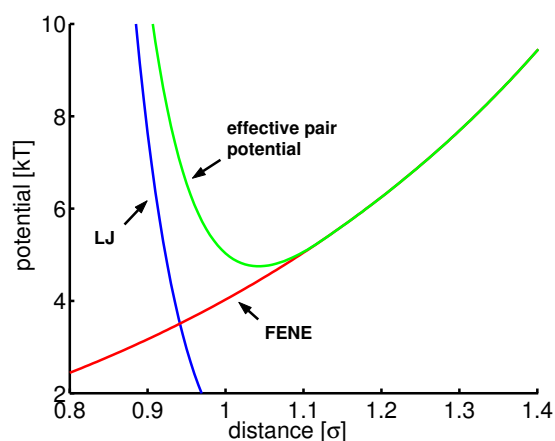
Figure 2.6: Effective potential between neighboring monomers
The effective potential is shown by the green curve. It is the sum from the pure repulsive Lennard-Jones potential, represented by the blue curve, and the attractive FENE potential plotted red. The effective potential has its minimum at approximately 1.01 σ, which defines the bond length.

The effective potential, which acts upon two bounded monomers, is shown in fig. 2.6 by the green line. It consists out of the pure repulsive Lennard-Jones potential, plotted in blue, and the FENE potential, which is represented by the red curve. The minimum is at $r \approx 1.01\,\sigma$, which determines the bond length.

Debye-Hückel potential The results expected from the studies of the sphere tail models are going to be compared to data obtained from biological systems. These are usually available at physiological conditions, what corresponds to a relatively high salt concentration of the surrounding solution. Due to the salt content of the solution, the electrostatic interaction between the charges becomes exponentially screened with the distance. The characteristic screening length in this case is due to the thermodynamic properties of the system [79].

In the case of dilute salt concentrations and sufficiently weak charge densities, the linear response or Debye-Hückel theory can be used [80]. In this case the salt is treated as an ideal gas and the screening length κ^{-1} is given by

$$\kappa^2 = 4\pi l_B I \tag{2.15}$$

with I representing the ionic strength $\sum_i Z_i c_i$ of the solution with Z_i being the valence and c_i the concentration of the species i [81]. Inside a cell nucleus the salt concentration is about 100 mM of sodium chloride, what corresponds to a value of κ of approximately $0.4\,\sigma^{-1}$. A short derivation of the formulas, used below, is presented in the Appendix B. Here we just give the results necessary for the simulation. The effective pair potential for two monomers, which can be treated as point like charges, is then given by

$$V_{\mathrm{DH}}^{\mathrm{mm}}(r) = l_B \frac{\exp(-\kappa r_{\mathrm{DH}}^{\mathrm{mm}})}{r_{\mathrm{DH}}^{\mathrm{mm}}}. \tag{2.16}$$

In the case of the interaction of a monomer and a core the interaction becomes

$$V_{\mathrm{DH}}^{\mathrm{cm}}(r) = Z l_B \left(\frac{\exp[\kappa a]}{1+\kappa a}\right) \frac{\exp(-\kappa r_{\mathrm{DH}}^{\mathrm{cm}})}{r_{\mathrm{DH}}^{\mathrm{cm}}}. \tag{2.17}$$

Finally the core-core interaction can be written as

$$V_{\mathrm{DH}}^{\mathrm{cc}}(r) = Z^2 l_B \left(\frac{\exp[\kappa a]}{1+\kappa a}\right)^2 \frac{\exp(-\kappa r_{\mathrm{DH}}^{\mathrm{cc}})}{r_{\mathrm{DH}}^{\mathrm{cc}}}. \tag{2.18}$$

In the simulations presented in this work, l_B was chosen to be $2\,\sigma$. κ ranged from $0.2\,\sigma^{-1}$ to $1.0\,\sigma^{-1}$.

The electrostatic interaction in a solution of salt is subject to screening and therefore can be modelled using the Debye-Hückel potential. However, by interactions ranging through one of the cores, e.g. of two charged monomers on the surface of one core, the interaction becomes complicated. The solution and the volume occupied by the NCP show different values of the refraction index and of κ. By choosing an effective charge for the core, we get rid of this problem for interaction, in which the core is involved (i.e. the interaction between two cores or between a core and a charged monomer). However, by interactions amongst monomers, these details are omitted.

At low salt concentrations the Debye-Hückel approximation allows an accurate description of the electrostatic interaction. In this work we investigate salt concentrations up to 1 Mol, which corresponds to a screening length of about 3 AA, which is about the size of the involved salt ions. In this region the Debye-Hückel approximation describes merely a short ranged sticky potential. A more accurate description of the electrostatic interaction would require the explicit simulation of the salt ions.

For the convenience of the reader we give a summary of the simulation parameters in Table 1. These values were used for all simulations, unless stated differently in the text.

Parameter	Symbol	Value
Bjerrum length	l_B	$2\ \sigma$
time step	Δt	$0.01\ \tau$
thermal energy	kT	ϵ
core central charge	Z	150
monomer charge		-1
core radius	a	$15\ \sigma$
friction constant	Γ	$\epsilon \cdot \tau/\sigma^2$
parameters for the		
GRAFT potential	k_{GRAFT}	$2\ \epsilon/\sigma^2$
	r_{GRAFT}	a
MATCH potential	k_{MATCH}	$2\ \epsilon/\sigma^2$
	r_{MATCH}	$17.3\ a$
FENE potential	k_{FENE}	$7\ \epsilon/\sigma^2$
	r_{FENE}	$2\ \sigma$
screening length	κ^{-1}	$2.5\ \sigma$
monomers per chain	N	28
charged monomers per chain		10

Table 1: Simulation parameters

2.2 Multi NCP models

In section 1.3 we saw, that the interaction of nucleosome core particles depends on the salt concentration, as documented in fig. 1.5. For a certain range the mutual repulsion of the particles is suppressed in a way that suggests a mechanism of attraction. The conditions of the appearance of this attraction are comparable to those, where the unfolding of the tail structure described in section 1.2 occurs. This coincidence might be a indication that the mechanism of attraction is tail induced. However there is also another possible mechanism that leads to such a non-monotonic form of the second virial coefficient. In this case the mutual attraction is due to the interaction between discrete charges on both complexes. In this section we want to give examples for both interactions showing similar behavior with respect to the particle interaction. The mechanisms giving rise to these results, however, are completely different.

2.2.1 Interactions due to the charge distribution

Counterion mediated interaction of charge patterns

One possible explanation for the effects observed in section 1.3 is the interaction of charge patterns. In reference [82] Allahyarov, Löwen, Louis and Hansen introduced a MD study investigating the second virial coefficient of colloidal "proteins". The method of extracting the second virial coefficient from a simulation will be explained in appendix A.2. The authors investigate the mutual interaction of spheres with Z

monovalent embedded discrete charge patches. As reference system serves the case of colloidal molecules with a central charge Z. In both cases the macroions carried charges with the same sign and were in a solution with discrete counterions and salt. The particles interact via excluded volume and Coulomb interaction. In order to obtain results comparable to experimental values, a short ranged attractive potential, modelling the hydrophobic and van der Waals interaction, was applied between the proteins. Fig. 2.7 illustrates the setup: Each spherical macroion carries charge patches shown as grey structures on the surface. The colloids are surrounded by grey counterions and black coions. The salt concentration here is approximately 200 mM. Due to the pure repulsive Coulomb interaction between the macroions, any attractive component, besides the implemented van der Waals/hydrophobic potential, has to be counterion mediated.
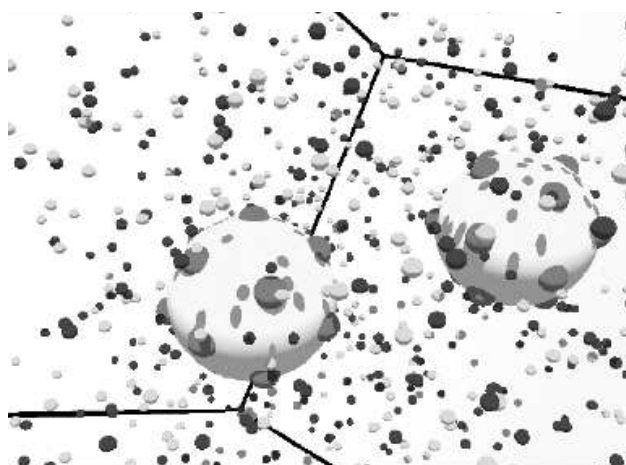
Figure 2.7: Snapshot of a typical MD configuration
Each macroion carries charge patches symbolized by the embedded dark spheres. The small grey spheres are counterions, the black ones coions. (Taken from [82])

Fig. 2.8 shows the results. In the large frame the second virial coefficient of the proteins is plotted as a function of the salt concentration. As unit for the second virial coefficient the authors of reference [82] chose the value obtained for a system of hard spheres carrying the same electrical charge. The case of colloids with smeared out charges is represented by the lines with symbols. Here a monotonic decay with increasing salt concentration can be observed. From top to bottom the central charges are 15, 10 and 6. In the discrete charge case, which is represented by the lines without symbols, A_2 becomes non-monotonic: At low screening A_2 decreases with increasing salt concentration until a minimum is reached. By increasing the salt concentration beyond this point, a rise of A_2 with increasing salt concentration can be observed. However at even higher salt concentrations A_2 reaches a maximum and decays finally.

For the case of the highest protein charge $Z = 15$, plotted with dot-dashed lines, the non-monotonic behavior of the curve is most distinctive. By decreasing the macroion

charge to 10, represented by the solid line, the depth of the curve decreases, as does the position of the maximum. Finally, for the lowest charge 6, the effect is least significant.

Obviously the interaction of the two macromolecules consists of three contributions: The attractive short range potential, which is independent from the salt concentration, the counterion mediated attraction, creating the minimum of the second virial coefficient at medium salt concentrations and the repulsive monopole repulsion due to the embedded charges. The rise of A_2 beyond the minimum is due to the monopole interaction. The reason for the final decrease of A_2 is the attractive short range potential. It leads to a negative limit of A_2 for high salt concentration in spite of the positive value that pure screening would suggest according to appendix A.

The inset shows the Coulomb interaction potential of the proteins as a function of the separation distance of the two proteins for the case $Z = 10$ in units of the protein diameter σ_p. The different curves represent different salt molarities as indicated in the legend. Here the evolution of the effective potential with increasing salt concentration can be observed.
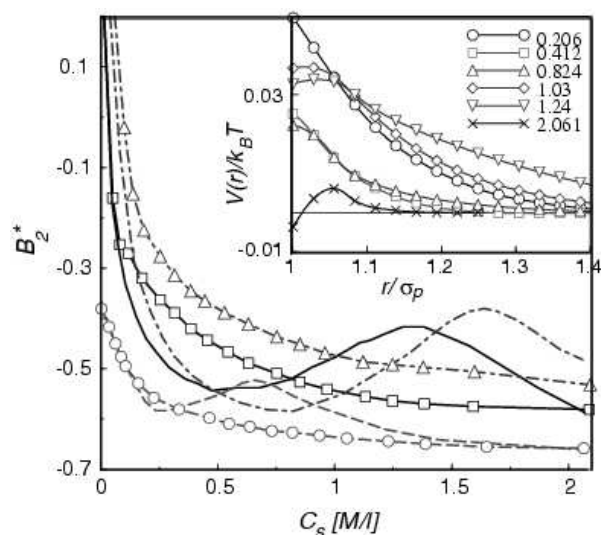
Figure 2.8: Second virial coefficient normalized by hard-sphere value The protein charges are Z=15 (dot-dashed lines), 10 (solid lines) and 6 (dashed lines). Lines without symbols correspond to the charge patches model, lines with symbols to the cases with smeared out charges. The inlet shows the Coloumb macroion-macroion interaction potential for Z=10 as function of the distance. The different curves represent different salt molarities as indicated in the legend. (Taken from [82])

A similar system was studied analytically as well as numerically by Rouzina and Bloomfield. They investigated the attraction of two surfaces due to screening counterion correlations [83]. On each of the two charged planes, they observe correlations amongst the condensed counterions. Due to the repulsion between the counterions, the counterion density around each counterion is low. The size of each of these correlation

holes corresponds to the average distance between neutralizing ion neighbors along the surface. Each surface is neutral on the average, but is decorated by an alternating pattern of positive and negative charges. Due to the mutual interaction of both charge patterns, the positions of the counterions are adjusted to each other to minimize their total energy, which results in mutual electrostatic interaction. The decay length of this interaction is of the order of the intrasurface ionic separation. This can be theoretically explained by applying Wigner Crystal arguments [36, 37, 84].

Dipole interaction in the sphere chain model

The model used in reference [82] was set up to describe the interactions of proteins in general. However, also for the nucleosome core particle a similar interaction was proposed. In reference [85] Boroudjerdi and Netz calculate the interaction of two sphere-chain complexes in the ground state approximation. By using parameters according to the histone core and the wrapping DNA they find the second virial coefficient to be negative for intermediate salt concentrations.

The interactions observed are rationalized to be due to the interaction of a monopole-dipole complex. In the explanation the emerging dipole is due to the charge distribution according to the position of the chain on the surface of the core.

However, in this picture the polyelectrolyte chain describing the DNA is allowed to freely reposition itself on the sphere in order to take the optimal configuration. As explained in section 1.1, the position of the DNA on the histone DNA octamer is already prescribed by the shape and arrangement of the histone proteins, so that such a repositioning seems unlikely.

2.2.2 Chain interacting model

As we have seen, the mere existence of a discrete charge distribution can lead to non-monotonic effects similar to those observed in the experiments with NCPs. However Podgornik suggested also another explanation for the observed attraction of the nucleosome core particles. In this approach the interaction is induced by bridges formed by the charged tails. Reference [4] is a variational study using a model of two macroions with one oppositely charged flexible chain each. Both chains consist of N monomers, giving rise to a contour length l. The electrostatic interactions are treated on the Debye-Hückel level. The macroions are modelled as pointlike particles. The surrounding polyelectrolyte chains are treated as Gaussian blobs. The width of these blobs is calculated by a harmonic variational ansatz including both the external fields acting on the chains and the self-interaction of the chains. Therefore a general harmonic Hamiltonian (in units of the thermal energy kT) of the form

$$H_0[\vec{r}_i(n)] = \frac{3}{2l^2} \sum_{i=1}^{2} \int_0^N \dot{\vec{r}}_i{}^2(n) dn + \frac{3}{2} \sum_{i=1}^{2} \zeta_i^2(\vec{r}_{0i}) \int_0^N [\vec{r}_i(n) - \vec{r}_{0i}]^2 dn + NL(\vec{r}_{01}, \vec{r}_{02})$$

(2.19)

was obtained. $\vec{r}_{0i}$ for $i = 1, 2$ stands for the center of mass of each chain. Apart from $\vec{r}_{0i}$ the solution depends on $\zeta_i^2(\vec{r}_{0i})$ and $L(\vec{r}_{01}, \vec{r}_{02})$, which have to be obtained

variationally. The term containing $\zeta_i^2(\vec{r}_{0i})$ represents an external harmonic potential. It is centered on $\vec{r}_{0i}$ and acting on the chain, confining or expanding it, according to its sign. $NL(\vec{r}_{01}, \vec{r}_{02})/kT$ is the value of this harmonic potential at the center-of-mass of the two chains.

Podgornik differentiates the variational solution of the problem into two branches according to the relative magnitude of the macroion-chain interaction and the sum of self interaction of the chain and the mutual chain interaction. In the strong-coupling limit, which corresponds to $\zeta_i^2(\vec{r}_{0i}) > 0$ in equation 2.19, the system is dominated by the macroion-chain interaction. In the weak-coupling limit, the chain interactions are the principal contributions. In this definition the term coupling refers to the chain-macroion interaction. The branch of strong coupling bifurcates again into two sub-branches: In the case of a weakly paired system, each chain is associated with its own grafting macroion, while in the case of strong pairing both chains share both macroions on the average. In general, in both cases of coupling, bridging interactions can be found. However, in the case of strong pairing they are several orders of magnitude stronger than in weakly paired case.

Fig 2.9 illustrates these cases. On the left side the system is strongly coupled, the interaction between the chains and the macroion dominates, resulting in a confined conformation of the chain with respect to the core. The NCP pair on top corresponds to the weakly paired state, each chain interacts only with its grafting macroion, while the configuration on the bottom illustrates the strong paired case with strong interaction between both structures.

The right side shows the case of weak coupling. Due to the lower chain-center attraction and the dominating self-interaction of the chains their conformations are much more extended. Both configurations here are weakly paired, the mutual interaction of the complexes is repulsive for all separations of the complexes. For low separation distances the reason for this behavior is the repulsive interaction of both chains. At higher separation distances, as in the case of strong coupling, the monopole repulsion becomes dominant. However, one has to note, that the cores in the variational calculation are treated as point particles unlike in the drawing.

The attraction observed in this model has its maximum for the case of strong coupling. Fig. 2.10 shows the pair interaction as a function of the distance between the macroions. The different symbols correspond to different chain length, which is from the bottom to the top 100, 30 and 10 monomers. The bold line represents the pure Debye-Hückel interaction which is always repulsive. The curves resulting from the variational calculation show a different behavior. For small distances repulsion due to the electrostatic interaction can be observed. By increasing the distance, a minimum can be found for intermediate distances. The depth of the minimum decreases with increasing chain length. At larger distances the potential snaps to the pure Debye-Hückel curve. The position of the snap, marking the transition from the strong to the weakly paired regime, increases with increasing chain length.
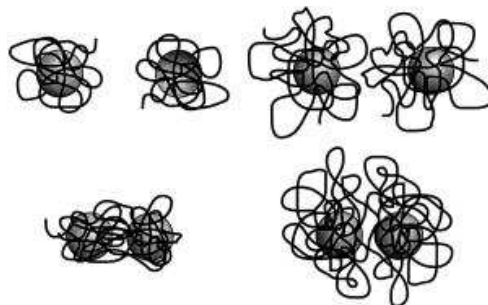
Figure 2.9: Schematic representation of the model proposed in reference [4] and its variational solutions

The left side represents the strong coupling solution branch. Due to the strong chain-center interaction, the chain configurations are confined to the macroion. The upper drawing shows the case of weak pairing. Due to the large distance every chain is confined to its grafting macroion. For short distances, as shown in the lower drawing, both chains share both macroions. The right side shows the case of weak coupling. In both cases the pairing is weak. Since the self-interaction of the chains is now the dominating factor, the configurations are more extended than in the case of strong coupling. The interaction of the complexes is always repulsive in this case, due to the mutual interactions of the chains. Note that the core particles are assumed to be point like particles and not finite size spheres as the drawing might suggest.(Taken from [4])

A presentation of the second virial coefficient calculated from this interaction potential was abandoned in reference [4]. The author stakes:

"At this stage it does not seem reasonable to compare the second virial coefficient derived from our calculation of the effective pair interactions with the experiments on NCPs. There would be just too many adjustments that one would have to put in by hand, but that would have a crucial effect on the ensuing numerical results [. . .] Nevertheless, if one chooses to ignore all these additional complications, the virial coefficient in the strong-coupling limit comes out always monotonically (decreasing) dependent on the screening length: i.e., ionic strength. No nonmonotonic effects, of the type that feature so prominently in experimental results, are ever seen for any reasonable values of parameters (i.e. the charges on the macroions, the length of the chain, the charges of the chain). Basing our conclusions on the analysis presented above, we are inclined to believe that the polyelectrolyte bridging itself never leads to a nonmonotonic second virial coefficient. One nevertheless has to keep in mind, that our model calculation is based on many constraints that are not entirely realistic."
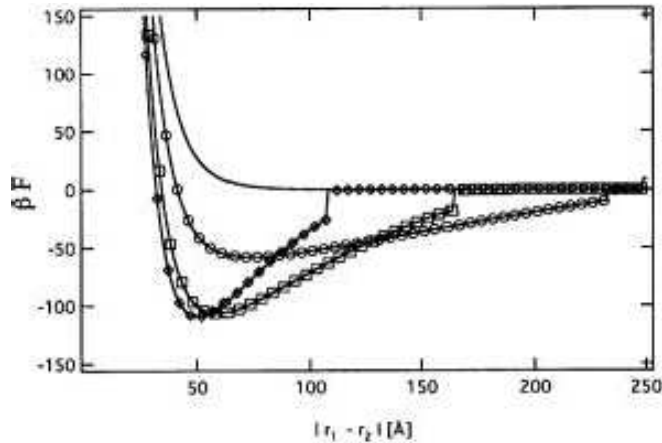
Figure 2.10: Interaction potentials obtained from the harmonic variational ansatz for the colloid-polyelectrolyte system

This plot shows the interaction potential obtained from the variational approach for the case of strong coupling on the separation of the macroions. The curves differ with respect to the chain length, from top to bottom $N = 10$, 30 and 100 at a salt concentration of 60 mM. The observed snapping, depending on the chain length, marks the transition from the strong to the weak paired regime. The bold line represents the pure Debye-Hückel interaction of the macroions. (Taken from [4])

This statement raises the question, if the approximations made were suppressing the effects of tail bridging or whether tail bridging at all can lead to the observed non-monotonic salt-dependence of A_2 as shown in fig. 1.5.

In reference [86] Pincus studies also a related system, namely a spherical colloid with grafted polyelectrolytes. However, in this case the grafting density is very high leading to a polymer brush. Furthermore the core does not carry any charge. The aim of that paper is to investigate the stabilization of colloids. Due to the electrostatic repulsion and the excluded volume interaction of the grafted chains, only repulsive interaction can be found in this case.

A Monte Carlo simulation of charged spheres with oppositely charged grafted polyelectrolytes is presented in reference [87]. The grafting monomers were assumed to be mobile on the surface of the sphere, otherwise the setup is qualitatively similar to the one presented here. However, it features an attractive short range potential between the macroions and differs considerably in properties like charge density of the surface of the sphere, charge fraction and length of the chains. In that study the authors observe attraction between the macroions, however a non monotonic behavior depending on the salt concentration was not stated and also not in the scope of the paper.

The interaction mediated by grafted ions and polyions of electric bilayers was also studied in the past [88]. In that case the authors find again attractive interaction for a range of the separation of both layers.

2.2.3 Simulation models

1 **plain spheres**

2 **discrete charge patches**

3 **single chain**

4 **several chains**
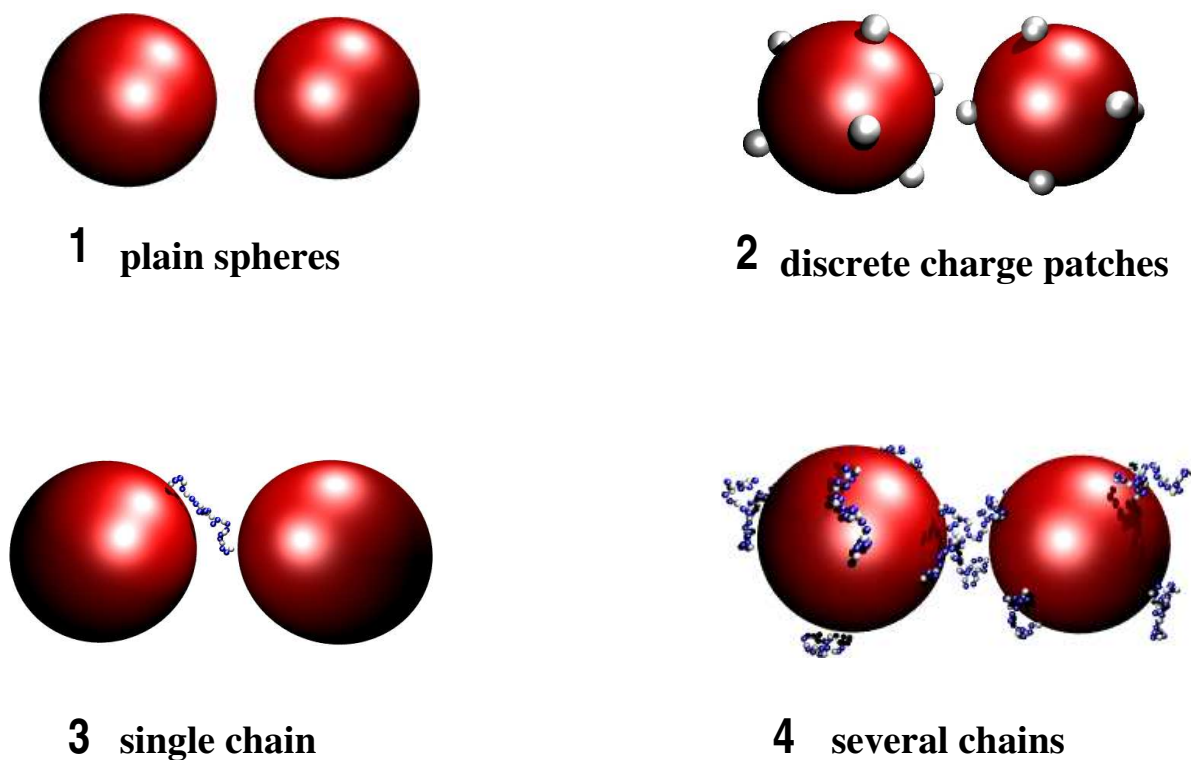
Figure 2.11: Different model for the investigation of the attraction between NCPs

The net charge and core radius of all introduced structures equal the values of the model described in 2.1.3. Model 1 is a plain sphere, yielding the monopole term of the system. In model 2 the monomers of each chain are condensed to a single patch carrying the charge of a entire chain. No chain effects are present in this case. Model 3 consists of two spheres interacting via a polyelectrolyte chain grafted on the surface of one core. This model complements the previous by eliminating interactions of charge patches. The focus here is on the tail mediated interaction. Finally model 4 consists of two spheres with eight charged tails as already described. Here both effects might occur.

As shown in the preceding sections, different reasons, namely interaction of charge patches and tail induced interaction, can be held accountable for attraction between NCPs. Our simulation model introduced in section 2.1.3 shows both features: On the one hand tail bridging is clearly possible due to the grafted tails on each complex, on the other hand each chain can be considered as a discrete charge patch. In order to isolate and distinguish the contributions from each of these interactions, we modify our model to be able to concentrate on one of the effects at a time. Overall, we have now four different models at hand. They are depicted in fig. 2.11:

1. The simplest case of plain charged spheres shows just the monomer repulsion due to the electrostatics.

2. In the second case, each chain is collapsed into a positive charge patch. Here the charge of an entire tail is concentrated on the patch. The patches are positioned on the surface of the negatively charged core particle. The intention of using this patch model is to get rid of bridging effects.

3. To isolate the tail induced interaction from the patchiness effect, the single tail model, presented here as model 3, was set up. Here two homogenously charged spheres interact via one polyelectrolyte chain, which is grafted on the surface of one of the spheres. In this case the sphere charges were reduced about the charges carried by the removed chains.

4. Finally in the last setup the full chain model combines both patchiness and tail effects: it is the full setup containing eight chains on a charged sphere which was already introduced in section 2.1.3.

In all four cases the complexes carry the same net charge. In the case of model 1, all tail charges are smeared out on the sphere. Consequently, each sphere carries the net charge of the full chain model. In the patch model, number 2 in fig 2.11, each tail is collapsed to a single patch carrying the entire charge of one chain. The central charge of this complex, as well as its net charge, is unchanged with respect to model 4. In order to get a model which concentrates on the bridging effects, all tail charges, except one tail for one complex, were smeared out on the cores.

The conformation of the positively charged histone proteins and the negatively charged DNA that forms the nucleosome core also shows a dipole [85]. The interaction via the dipole is low at physiological salt concentrations [85]. As we will see later, tail bridging occurs in the case of a smeared out core charge. Therefore the charge distribution on the sphere can be seen as an effect of lower order and will be neglected in this study.

2.3 Summary

The model mainly used in the literature to describe the nucleosome in theories and simulations is the sphere polyelectrolyte model. Here the sphere represents the histone core, while the polyelectrolyte models the DNA wrapped around. Such models can explain charge inversion, however tails have been neglected so far. Another model used in simulations can be obtained by using the DiSCO (Discrete Surface Charge Optimization) algorithm. Here the discrete charge distribution is mapped on a virtual surface around the core particle structure. The idea of this approach is to get a more detailed reproduction of the electrical field generated by the charges from the NCP. However, as in the case of the sphere polyelectrolyte model, the charged histone tails were neglected. For this reason the existing models are not applicable to our simulations.

In order to obtain a model suitable for our needs, we introduced the multi-chain complex. In this model the histone tails and the wrapped DNA are represented by

a sphere with a negative net charge. The eight histone tails are modelled as flexible polyelectrolyte chains having one end grafted to the surface of the sphere. The eight grafted end monomers sit on the corners of a cube. Their relative positions are fixed by harmonic potentials between the next neighbors. The distance between the core center and the grafted monomers is controlled analogously by a harmonic potential. Furthermore a Lennard-Jones potential is applied for the excluded volume interactions, a FENE potential models the bonding interactions of the chains and the electrostatic interactions are computed via the Debye-Hückel potential. The thermodynamic equilibrium is realized by using a Langevin thermostat.

The interaction between nucleosome core particles, which was discussed in the previous chapter, could in principle come from two effects: The interaction via the discrete charge distribution and the tail induced attraction. For both effects examples were discussed. The setup of the multi tail system shows features which are capable of both kinds of interaction: The charged chains can be seen as charge patches, however they can also form bridges between both cores.

In order to be able to distinguish the effects, we modify the model accordingly. In the patch model each chain is condensed to a single monomer, so the bridging effects are eliminated. In the case of the single chain model, the discrete charge distribution was eliminated by including the chains in the core. One chain per pair of NCPs was kept, in order to allow tail interaction.

Despite the fact, that those representations of the NCP carry the same monopole moments, the mutual interaction differs dramatically for each case, as we will see later.

3 Properties of a single complex

Our model differs from the NCP with respect to some features: The shape of the NCP is more like a flat cylinder than that of a sphere. Also is the charge of the NCP discretely scattered over the complex rather than a evenly distrubuted. Finally the tails are not evenly located over the NCP, neither are they of the same length or equally charged. All these effects have an impact on the swelling behavior, we want to investigate. Since we cannot include all these effects, we have to renormalize the central charge of our sphere, in order to be able to observe an unfolding of the tails similar to that observed for the real NCP. The aim of this chapter to chose an effective central charge Z that shows a swelling behavior compatible with the experimental data for the relevant range of salt concentrations discussed in section 1.2.

3.1 Configurational changes

In order to get a comprehensive overview of the configuration space, Z was varied from 0 to 300 and κ from 0 to 1 while the radius a of the core was kept constant at 15 σ. This corresponds to a variation in the salt concentration from 0 to 5 Mol. Each simulation was set up for 10^6 time steps. Every 200 time steps the configurations were evaluated. The first $2.5 \cdot 10^5$ time steps were discarded in order to equilibrate the system. Each simulation took about five hours on a AMD XP 2000+ processor at 1.67 GHz. The overall consumption of CPU time for this study was about 360 hours. In order to perform these simulations, a MD program was written in the programming language C. Some of the routines concerning the force calculation could be adapted from existing software. For the data analysis matlab scripts were used, which were written for this purpose.

In the limits of high/low salt concentration and high/low central charge four cases can be distinguished for our full chain model. Fig. 3.1 shows typical conformations of those cases obtained by simulation:

1. **low central charge and low salt concentration:** The chains are stretched radially extending from the core. This behavior can be rationalized as follows: There is only a small central attractive force on the charged monomers due to the low central charge. This attraction is overruled by the monomer-monomer repulsion that results, since almost no screening is present, in the radial extension of the tails. Since the screening is so low, also interaction between the chains is present. By optimizing their electrostatic energy, they stretch away from the core, extending the structure.
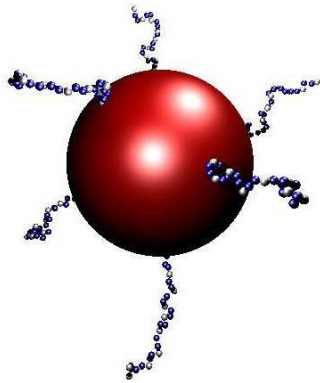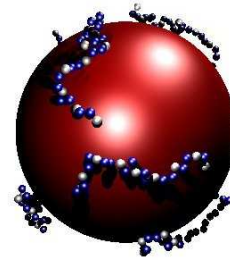
1 **low salt, low central charge** **2** **low salt, high central charge**
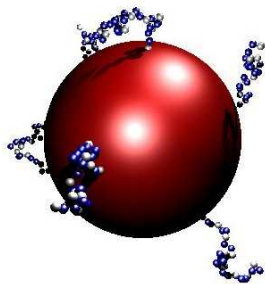
3 **high salt, low central charge** **4** **high salt, high central charge**
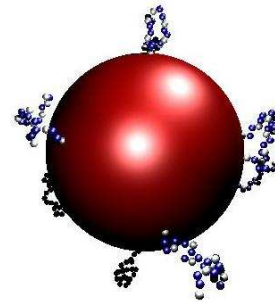
Figure 3.1: Conformations for different central charges/salt concentrations

The conformational state depends strongly on the salt concentration and the charge of the core Z. At low salt concentrations the tails are condensed onto the sphere for large values of Z and highly extended for small Z-values. At high salt concentrations the conformations for low and high Z-values are nearly indistinguishable due to the screened electrostatics.

2. **high central charge and low salt concentration:** The tails are condensed on the surface of the sphere, leading to a reduced size of the structure. The dominating factor in this case is the attraction of the core due to the high central charge. This effect wins against the monomer-monomer and the chain-chain repulsion that dominated the previous case.

3. **low central charge and high salt concentration:** The chains form self-avoiding-walk-like configurations. Since the system is heavily screened, monomer-monomer repulsion is only short-ranged and the chain-chain interaction is completely screened. Therefore the chain conformations are less stretched than in the low salt case, resulting in reduced extension.

4. **high central and charge high salt concentration:** This configuration is very similar to the preceding one. Again the chains form polymer coils. Obviously the high salt concentration screens not only the repulsive interactions between the monomers and the chains, but also the core-monomer attraction. The overall extension of the structure is now enhanced compared to the low salt case. Evidently in the limit of "perfect" screening case 3 and 4 are asymptotically identical.

3.2 Average diameter of NCPs

A quantity that allows the comparison of the simulation results to the experiment described in reference [1] is the diameter of the structure. It is given by the average maximal distance D_{max} between the two most distant monomers of the eight tail complex:

$$D_{\mathrm{max}} = \langle \sqrt{(\vec{r_i} - \vec{r_j})^2} \rangle \tag{3.1}$$

Here i and j denote the two monomers of the complex with maximal distance from each other.

Fig 3.2 shows the influence of the central charge and the salt concentration on the extension of multi tail complexes. The height of the surface in fig. 3.2 represents the average diameter of a given complex. The left axis describes the central charge Z ranging from 0 to 300 elementary charges. The salt concentration varies between 0 and about 5 Mol. This corresponds to a change of κ from 0 to about 1 σ^{-1}. The diameter of the complex has its maximum in the limit of low salt concentration and low central charge. Case 1 of fig. 3.1 is a typical conformation found in this regime. By increasing the central charge at constant salt concentration a steep decrease of the diameter to its minimum in the limit of high central charge and low salt concentration can be observed. A corresponding configuration is depicted in fig. 3.1, case 2. By increasing the salt concentration, the size difference of complexes with low and high central charge decreases. The extensions of the multi-tail complex converge to a common value due to the increasing screening. The corresponding conformations in fig. 3.1, 3 for the low central charge and 4 in the case of a high charged system, show no qualitative difference.

The convergence of the diameter with increasing salt concentration can also be seen in Fig. 3.3. It shows the diameter as a function of κ for different central charges Z. The curve is a spline function between the data points to guide the eye. The curve on top corresponds to a central charge of $Z = 0$. For each curve closer to the bottom Z increases in steps of 50 until it reaches 300 for the lowest curve. The curves are cuts of the surface presented in fig. 3.2 with planes of constant Z. While for low salt
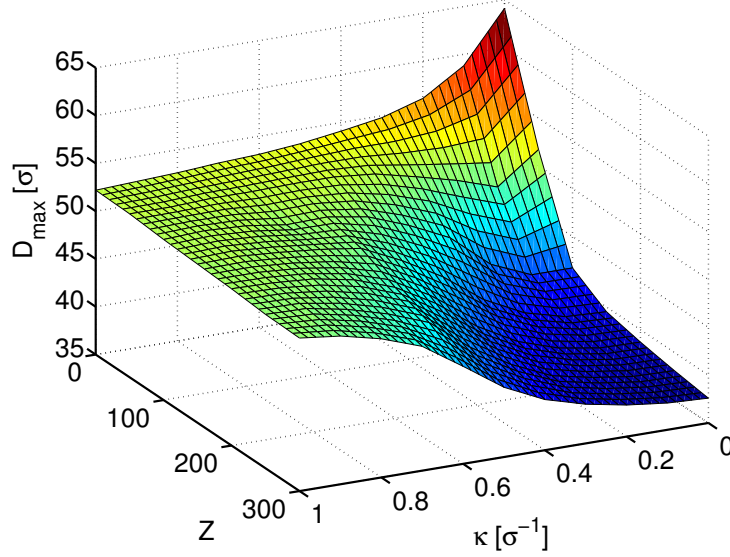
Figure 3.2: Average diameter of multi-tail complexes
The surface represents the diameter D_{max} of multi-tail complexes as a function of κ and of the central charge Z. The central charge is represented by the left axis ranging from 0 to 300 negative elementary charges. κ is shown on the right axis, ranging from 0 to 1 σ^{-1}. For the case of low Z and low salt concentration (i.e. small κ) the average diameter shows a maximum continuously decreasing for higher central charges to the minimum in the high central charge limit. When increasing the salt concentration, the differences between the high central charge and the low central charge are less pronounced. In the limit of high salt concentration the high charged and low charged structures are identical. (See also fig.3.3)

concentrations the extreme values appear clearly for $Z = 0$ and $Z = 300$, the curves converge for high salt concentration to a common value.

For $Z = 50$ the diameter of the complex shows a non monotonic behavior when increasing κ for low values of κ. For very low values of κ, D_{max} decreases with increasing κ until it reaches its minimum at $\kappa \approx 0.1$ σ^{-1}. By increasing κ beyond this value, an increase of D_{max} to the asymptotic value can be observed. The position of the minimum at 0.1 σ^{-1} corresponds to a screening length of 10 σ, which is of the order of the distance between two of the grafted chains. This gives rise to the idea, that the observed minimum might be caused by the interactions between the chains. To be able to discriminate the impact of the inter chain interaction on the extension of the complex from the other present interactions, like repulsion between the monomers of a single chain and attraction between the monomers and the core, we set up a further model consisting of a sphere representing the core and a single monomer chain grafted on the surface. We want to compare the outcome to the results of the multi chain
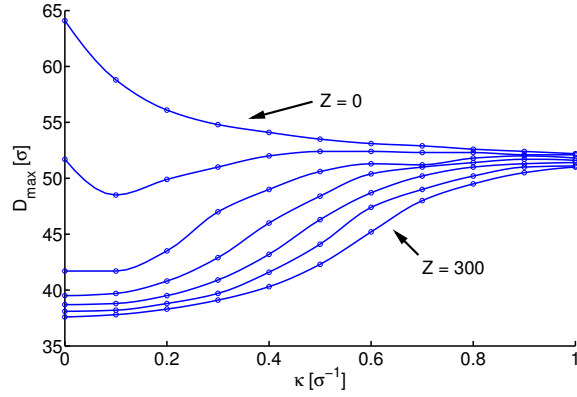
Figure 3.3: Cuts through fig. 3.2 along the salt concentration axis
This plot shows $D_{\max}$ for constant values of Z. The values for Z are from
top to bottom 0, 50, 100, 150, 200, 250 and 300. The low salt case features
the extreme values for the extension, while the curves converge for high
salt concentrations to a common value.

model at $Z = 50$. However, since the overall charge of the complex of the single chain
model has changed due to the absence of the other seven tails, the central charge will be
somewhat renormalized. For the multi chain model we measured the average diameter,
which consists of twice the core radius and twice the average extension of one tail. In
the case of the single chain model, we only have one tail. In order to obtain comparable
results, we measure here $R_{\max}$, the average distance between the center of the sphere
and the monomer most distant from the core. Twice this value corresponds roughly to
$D_{\max}$ measured for the multi chain model.

Fig. 3.4 presents $R_{\max}$ as a function of κ for the single chain model for different
values of Z. For $Z = 0$ we see a monotonic decrease of the extension with increasing
κ. By increasing Z to 10 the behavior changes dramatically: For very low values we
observe an increase of $R_{\max}$ with increasing κ, until $R_{\max}$ reaches a maximum at about
$\kappa = 0.3\ \sigma^{-1}$. For higher values of κ a monotonic decrease of $R_{\max}$ with increasing κ can
be observed. The screening length, which corresponds to the position of the observed
maximum at about $0.3\ \sigma^{-1}$ is about $3\ \sigma$. This is roughly the distance between two
neighboring charges on the grafted polyelectrolyte chain. Apparently the repulsion
between the chain monomers is responsible for the rising of $R_{\max}$. For $Z > 20$ non-
monotonic behavior cannot be observed anymore. Here $R_{\max}$ increases with increasing
κ over the entire range. Apparently the interaction between the central charge of the
sphere and the charged chain monomers is now so strong, that the interaction between
the monomers is negligible.

At $Z = 0$ we can directly compare the multi and the single chain model, since we do
not have to renormalize the central charges. By comparing the maximum value of $R_{\max}$
of the single chain model with $\frac{1}{2}D_{\max}$ of the multi chain model, we find that for very
small values of κ, the extension in the case of the multi chain model is considerably
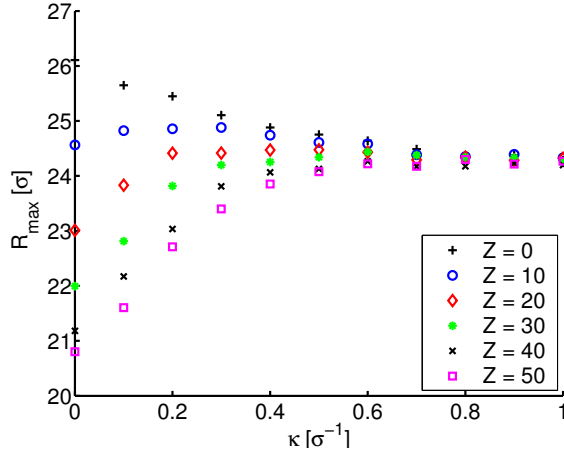
Figure 3.4: Extension of a single chain complex
The average distance between the center of the sphere and the most distant monomer is presented as a function of κ for different values of Z. For $Z = 0$ $R_{\max}$ decreases monotonic with increasing κ. For $Z = 10$ and $Z = 20$ $R_{\max}$ increases for very small values of κ to a maximum located at $\kappa \approx 0.3\ \sigma^{-1}$. The corresponding screening length is about $3\ \sigma$, which is approximately the distance between two neighbor charges on the chain. Apparently the here observed maxima correspond to the screening of the interaction between the chain monomers. For values of κ beyond the maxima, $R_{\max}$ decreases with increasing κ. For $Z > 20$ for all values of κ $R_{\max}$ increases monotonically with increasing κ.

larger than for the single chain model. Apparently the extension of the multi chain complex is affected by three electrostatic effects: The repulsion between the charged chains, the repulsion of the charged monomers within a single chain and the attraction between the charged monomers and the oppositely charged core. Since the charged chains interact over a range of about $10\ \sigma$, this interaction is mostly screened at $\kappa \approx 0.1\ \sigma^{-1}$. The charged chain monomers have a distance of about $3\ \sigma$ to their next charged neighbor, so their interaction is mostly screened at $\kappa \approx 0.3\ \sigma^{-1}$. The charged monomers can come very close to the core, the minimum distance between them and the surface of the sphere is only limited by the excluded volume interaction. The closest realistic encounter of a monomer to the surface of the sphere would be about σ. To obtain screening on this length scale we have to choose a value of κ of about $1\ \sigma^{-1}$. Our results support this picture: The non monotonic behavior presented for the single chain complex in fig. 3.4 is due to the repulsion of the monomers of a single chain. The differences observed for the single and the multi chain model, like the enhanced extension of the multi chain complex with respect to the single chain complex at $Z = 0$ for very low salt concentrations, and especially the non monotonic behavior of the extension of the multi chain model at $Z = 50$, which cannot be observed for the single chain model, are due to the mutual repulsion of the chains. Finally, the dramatic

differences of the extensions in both models between the cases of high and small values of Z are due to the interaction of the center with the charged monomers.

Now we want to determine the value for the central charge, which allows us to reproduce the experimental findings of the extension of the NCP. Comparison of the results presented in fig. 3.3 with the corresponding experimental findings presented in fig. 1.4, allows us to choose a reasonable value of Z, namely $Z = 150$. It corresponds to the fourth curve from the top of fig. 3.3 which comes closest to the experimentally observed curve, fig. 1.4. For this case the unfolding of the tails can be observed in the range from $\kappa = 0$ to $\kappa = 0.7 \ \sigma^{-1}$.

3.3 Monomer distribution

The diameter studied in the preceding section can be compared to the experimental measurements. However, it only gives information about the monomers far away from the core. Our simulation allows to study all monomers. We present in the following the monomer distribution around the core.

3.3.1 High central charge

Fig. 3.5 shows the monomer density for $Z = 150$ for different values of κ. Since a Lennard-Jones potential is used to model the excluded volume interaction of the core, the monomer density is very low for distances smaller than σ. In the case of low κ the attraction between the monomers and the central core is dominating. For this reason the monomers stay in this case close to the core forming a narrow peak as shown by the blue curve. With increasing salt concentration the central potential is subject to screening. The tails separate now from the core due to entropic reasons. The monomer distribution becomes wider reflecting the unfolding of the complex. During this process the maximum of the distribution becomes flattened out.

The largest distance with non-zero monomer density corresponds to the diameter observed in the simulation for the represented value of κ in the figures 3.3 and 3.2 respectively. Consistent with the previous results, it moves to farer distances for higher salt concentrations.

3.3.2 No central charge

The case $Z = 0$ is represented in fig. 3.6. For $\kappa = 0$ the distribution of monomers is slightly decreasing with increasing distance from the core. Since there is no attraction from the core, the main component of the interaction is here the repulsion of the charged monomers. In the case of no salt, they can employ their electrostatic repulsion fully, resulting in almost stretched chains, as shown in fig. 3.1, case 1. By increasing κ this interaction becomes screened. The distribution becomes now less extended. In the high salt case they form polymer coils, similar to those observed in the high salt case of the preceding section. Largest distance with non-zero monomer distance, which represents the diameter, shifts, in agreement to the data shown in fig. 3.3, to lower values with increasing salt concentrations.
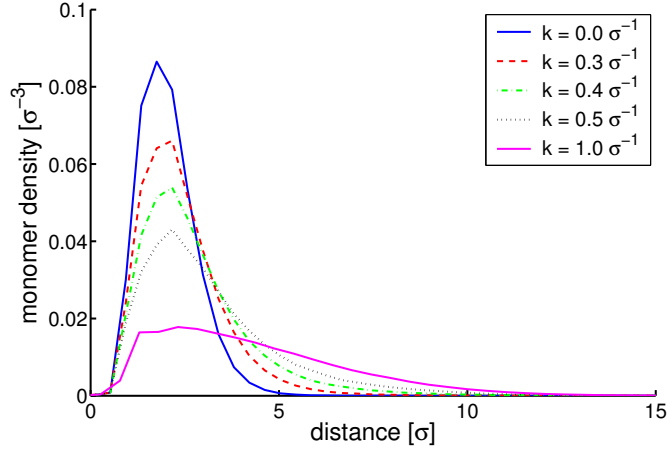
Figure 3.5: Monomer density around the core
The densities are measured for $Z = 150$ and different values of κ as indicated in the legend. In the case $\kappa = 0$ the monomers stay close to the core. Since the simulation uses a Lennard-Jones potential, the monomer density is very small for distances smaller than σ. With increasing salt concentration the monomer distribution smears out and shifts its maximum slightly to higher values of r.

3.4 Statistical properties of the chains

Other interesting observables measured in this study are static properties of the chains, like the end-to-end distance R_{EE} or the radius of gyration R_G of the chains. The end-to-end distance is defined as the length of the end-to -end vector $\vec{r}_{EE}$ and can be written as [89]

$$R_{EE}^2 = \langle \vec{r}_{EE}^2 \rangle = \langle (\vec{r}_N - \vec{r}_1)^2 \rangle. \tag{3.2}$$

Here $\vec{r}_1$ and $\vec{r}_N$ denote the positions of the first and the last monomer in the chain, respectively. Fig. 3.7 presents the end-to-end distance of a single tail of our chain sphere complex as a function of κ. The different symbols represent different values of the central charge Z. For all values of Z R_{EE} has its maximum at $\kappa = 0$ and decreases with increasing salt concentrations to a common value of about $10.5\,\sigma$. In the case of no central charge the maximum value of R_{EE} is about $15.8\,\sigma$ and decreases continuously until it reaches the common value at $\kappa \approx 1.0\,\sigma^{-1}$. For $Z = 150$ the maximum value of R_{EE} adds up to $12.1\,\sigma$ and decays continuously until it reaches it minimum at about $\kappa = 0.5\,\sigma^{-1}$. For larger values of κ it remains at the value common for all three values of Z. A similar behavior can be detected for $Z = 250$: Here the maximum of R_{EE} at low values of κ is also at about $12.2\,\sigma$ and remains constant to a value of κ of about $0.1\,\sigma^{-1}$. Then the end-to-end distance decreases with increasing salt concentration until it reaches the common value for high salt concentrations at $\kappa \approx 0.5\,\sigma^{-1}$.
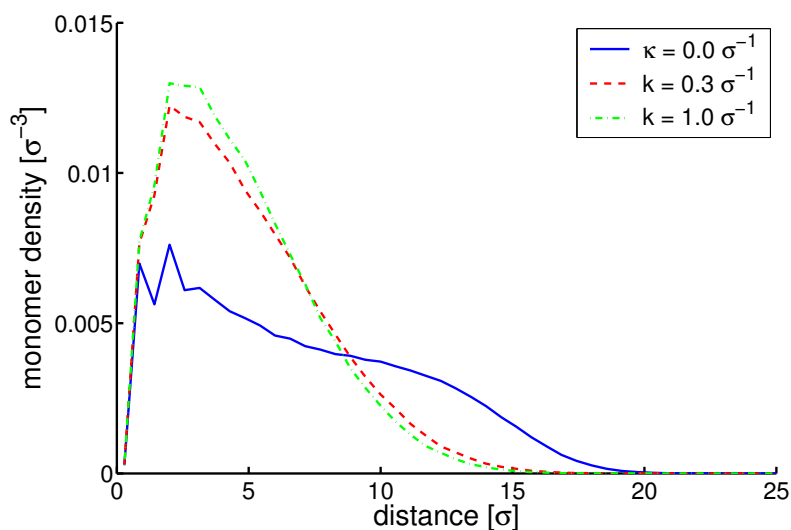
Figure 3.6: Monomer density around the core

Densities are measured for $Z = 0$. The distribution is flat for the no salt case, reflecting the stretched tail configurations observed in this regime. With increasing salt concentration the chains start to form coils. The extension of the complex shrinks, the monomer distribution converges to the one observed in fig. 3.5, at high salt content.
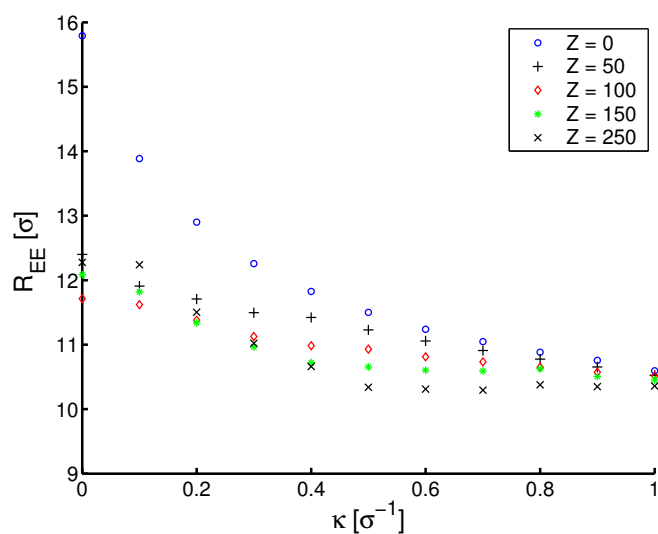
Figure 3.7: End-to-end distance

The end-to-end distance is presented as a function of κ for different values of Z as indicated on the legend. In all three cases the maximum value is located at $\kappa = 0$ and decays to a common value for high salt concentrations.

3 Properties of a single complex

The radius of gyration R_G is defined as [89]

$$R_G^2 = \frac{1}{N^2} \sum_{ij} \langle (\vec{r}_i - \vec{r}_j)^2 \rangle \tag{3.3}$$

with $\sum_{ij}$ representing the summation over all possible pairs ij of monomers of a chain. The radius of gyration is presented in fig. 3.8 as a function of κ for different values of Z. In all three cases R_G has its maximum value at $\kappa = 0$ and decays continuously to a
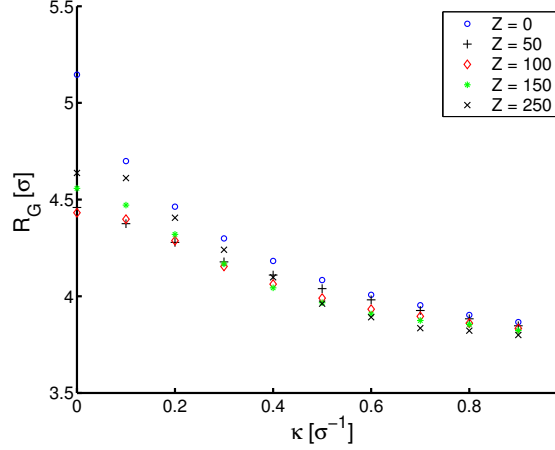
Figure 3.8: Radius of gyration

The radius of gyration is shown as a function of κ for different values of Z as indicated in the legend. For all values of Z the value of R_G has its maximum value at $\kappa = 0$ and decays continuously to a value independent of Z. The maximum value of R_G decays with increasing Z.

common value of about 3.8 σ for high salt concentrations. The maximum value of R_G is decreasing with increasing from about 5.2 σ for $Z = 0$ to about 4.5 σ for $z = 250$.

Fig. 3.9 presents the ratio between the squared end-to-end distance and the squared radius of gyration.[1] For $Z = 0$ R_{EE}^2/R_G^2 is continuously decreasing with increasing κ, corresponding to the transition from the stretched tails depicted in fig. 3.1 case 1 to the coils for case 3. For higher values of Z the behavior is different: For low salt concentrations R_{EE}^2/R_G^2 decreases with increasing κ to a minimum at about $\kappa = 0.3$ σ^{-1}. By increasing κ beyond this value, R_{EE}^2/R_G^2 rises again until it reaches the asymptotic value for high salt concentrations, which is independent from Z. As noted before, the interaction between the chains becomes mostly screened at relatively low salt concentrations. Consequently the reason for the non monotonic behavior of R_{EE}^2/R_G^2 as a function of κ might be the interaction between the chains at very low values of κ. In order to optimize their electrostatic energy, the chains might adopt configurations,

---

[1]The characteristic ration R_{EE}^2/R_G^2 describes the shape of a polymer coil. For a random-walk configuration it has the value 6. A self-avoiding walk configuration corresponds to a value of 6.3. For a rod-like polymer R_{EE}^2/R_G^2 is 12 [89].
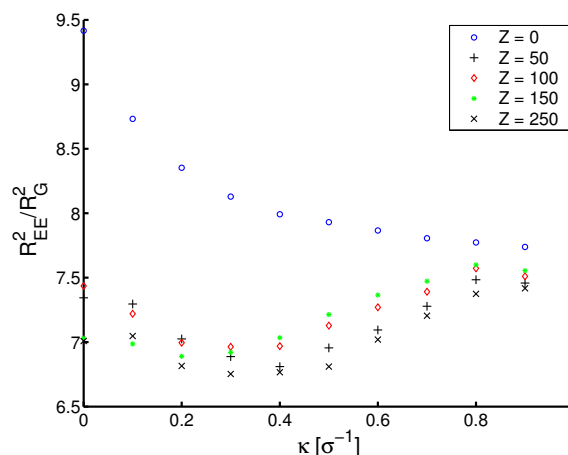
Figure 3.9: R_{EE}^2/R_G^2

The ratio R_{EE}^2/R_G^2 describes the shape of the coil formed by the polymer chain. A higher value corresponds to a more stretched configuration. For $Z = 0$ R_{EE}^2/R_G^2 decreases continuously with increasing κ. For $Z > 0$ R_{EE}^2/R_G^2 decreases with increasing κ until it reaches a minimum at $\kappa = 0.3$ σ^{-1}. Further increasing of κ leads to a increase of R_{EE}^2/R_G^2 until it reaches a common value, which is independent of Z.

which are more stretched. With increasing κ that interaction gets screened, resulting in a slight drop of R_{EE}^2/R_G^2. Finally, with increasing κ, the inter chain interaction gets completely screened at the observed minimum. When κ is increased beyond that level, the interaction between the charged monomers and the charge of the sphere gets screened. This results in a higher value of R_{EE}^2/R_G^2. The left side of fig. 3.10 depicts the configuration of a chain complex at $\kappa = 0$ and $Z = 100$. Under these conditions the maximum of R_{EE}^2/R_G^2 at low values of κ and high central charges can be observed. The right side presents a configuration of a complex with $Z = 250$ at $\kappa = 0.4$ σ^{-1}, which corresponds to the minimum of R_{EE}^2/R_G^2. Apparently here the interaction between the charged monomers and the charged core is still present, but not as strong as in the case of $\kappa = 0$. The chains here are still close to the core, but they are not condensed to its surface, as in the low salt case presented on the left side of the figure. The case of high salt and high central charge is presented as case 2 in fig. 3.1. Here the chains are separated from the core, similar to the case of no central charge and high κ.

Summary

In this chapter the properties of an isolated multi chain complex were investigated. First a parameter scan with regard to the central charge of the sphere Z and the screening constant κ was carried out in order to find the relevant region, where the unfolding of the tails can be observed. We find the following general behavior of the complex: For low Z and low κ the extension of the particles is maximal. Due to
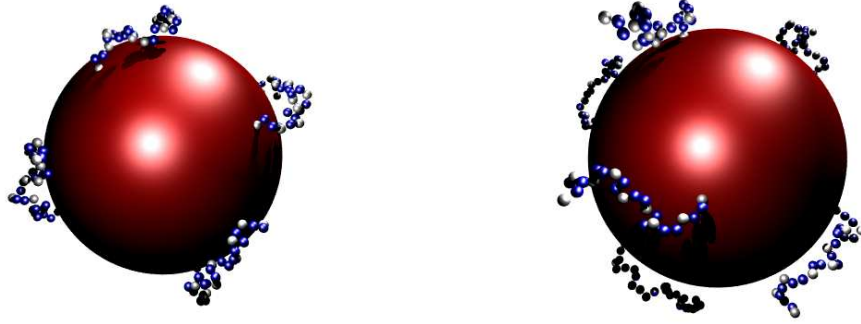
Figure 3.10: A typical conformation for $k = 0$, $Z = 100$ (left side) and $k = 0.4\ \sigma^{-1}$, $Z = 250$ (right side)

the lacking central attraction of the core and the mutual repulsion of the charged monomers, the chains are almost stretched. For high Z and low κ we observed the opposite behavior, the tails condensed on the surface of the core resulting in the minimal size of the structure. Due to the high central charge and the low screening, the central attraction is here the dominating factor. In the cases of the high salt concentrations, the resulting configurations are essentially identical: In both cases the chains form coils of comparable size. The monomer distribution was also evaluated. For the case of high Z a peak near the surface of the central sphere could be observed for the case of low κ. With increasing κ the maximum of the distribution shifted to higher distances and the peak smeared out. For low Z the distribution showed the opposite behavior. The distribution was widely stretched for low κ. With increasing κ it became smaller, approaching the same value as for the high salt case with high central charge.

The shape of the coils formed by the tails was investigated using the ration R_{EE}^2/R_G^2 of the squared end-to-end distance and the squared radius of gyration. For $Z = 0$ R_{EE}^2/R_G^2 decreases continuously with increasing κ indicating the transition from a stretched chain to a coil. For $Z > 0$, R_{EE}^2/R_G^2 decreases with increasing κ to a minimum and rises to a value which is similar to the value for high salt concentrations for $Z = 0$.

A comparison of the salt dependence of the diameter of the complex in our simulation to that of the experiment, allowed us to choose a reasonable value of the central charge. In the next chapter we will use this value in order to investigate the interaction between two multi chain complexes.

4 Interactions of complexes

In the last chapter we found for our full chain model a tail unfolding process comparable to that observed in the experiment. This allowed us also to identify the relevant parameter values for Z and κ. The task now will be to check whether in this parameter region mutual attractions between particles occur, and to identify the processes underlying those interactions.

4.1 Interaction of the tail systems

4.1.1 Interaction force

The effective potential between sphere tail complexes in the Debye-Hückel picture derives from two sources: On one hand the electrostatic interaction of the charged spheres and monomers, and on the other hand the entropic contributions due to the tail configurations. Since the simulations are performed at a constant core-core distance, which is in any case larger than two times the core radius, excluded volume interactions between the cores do not occur.

Due to the entropic contributions of the tails it is not possible to compute the interaction potential directly. Instead we determine the interaction via a molecular dynamics simulation. For the calculation of the interaction potential of the complexes at low concentration, a simulation was set up with two complexes fixed at a distance d. The force acting on the cores consists of four contributions:

1. Between both cores exists electrostatic repulsion.

2. The cores also interact with the charged monomers via electrostatics.

3. Monomers close to the core surface are also subject to pure repulsive Lennard-Jones interaction with the core.

4. The last interaction affecting the cores is due to the grafted chains: The monomers forming a chain are connected to their next neighbors by bonds. The last monomer is grafted on the surface of the core, i.e. it is connected to the core via a bonding potential. So forces acting on the chain will also act on the core via the grafting monomer.

At higher salt concentrations the electrostatic interactions are screened. Consequently the core-core repulsion is only important for small core-core separations in this case. Also the interaction between the core and the oppositely charged monomers is subject to screening. Here the interaction is unique to monomers close to the core.

This might include monomers belonging to the complex observed as well as monomers from the other complex forming a bridge between both cores.

All these contributions add up to the effective force acting upon the core of the multi tail complex. Knowing the effective force of both cores, the mutual interaction force can be defined as the interaction force along the connecting line of the two centers:

$$F_{\text{int}} = \frac{1}{2}\langle(\vec{F}_2 - \vec{F}_1) \cdot \vec{e}_{12}\rangle \tag{4.1}$$

$\vec{F}_i$ is the effective force on the core of complex i and $\vec{e}_{12}$ denotes the unit vector from the center of complex 1 to the center of complex 2. The brackets $\langle \ldots \rangle$ denote thermal averaging. In the case of attraction the resulting force F_{int} will be negative and positive in the case of repulsive interaction.

By using equation 4.1 the mutual interaction of the two complexes can be computed for a given set of configurations. By repeating this procedure for different values of d, the force distance relation can be obtained by fitting the resulting set of data with a least squares fit. As a fitting function the product of a rational function and an exponential function was used. The explicit fit functions and the parameters obtained for the data sets are put into the Appendix C.

The upper half of Fig. 4.1 shows exemplarily the force distance relation for a complex with a center charge of $Z = 150$, a radius of $r = 15\ \sigma$ and a salt concentration of about 120 mM corresponding to $\kappa = 0.4\ \sigma^{-1}$. The measured mean force is represented by the symbols, the line plotted through the data shows the least squares fit. Each data point shown in fig. 4.1 is the result of a MD simulation of 10^6 time steps consuming approximately four hours of CPU time on an Intel Xeon processor at 2.4 GHz. $2.5 \cdot 10^5$ time steps were given to equilibrate the system and not included into the evaluation. From the rest of the data, the interaction force was evaluated every 250 time steps. At low distances the force is repulsive due to the strong monomer interaction: By increasing the distance the force shows a steep decrease until it reaches its minimum at a distances of about 6 σ. Here the force is weakly negative, what corresponds to attraction between the complexes. At higher distances the force increases again and approaches zero.

In order to obtain the pair potential with the statistical error between two complexes, a sample of ten sets of data for the force as a function of the core-core separation like the one presented in the upper half of fig 4.1 were evaluated. By integration a potential function was obtained for each fit. The lower part of fig. 4.1 shows the average potential function of the sample with the statistical error for the parameters given above. The consumption of CPU time necessary to obtain one potential curve as presented here adds up to approximately 1000 hours.

To carry out the simulations, the MD program used for the simulations of the single comples was extended. The analysis was done using Mathematica and Matlab scripts, which were written for this purpose.
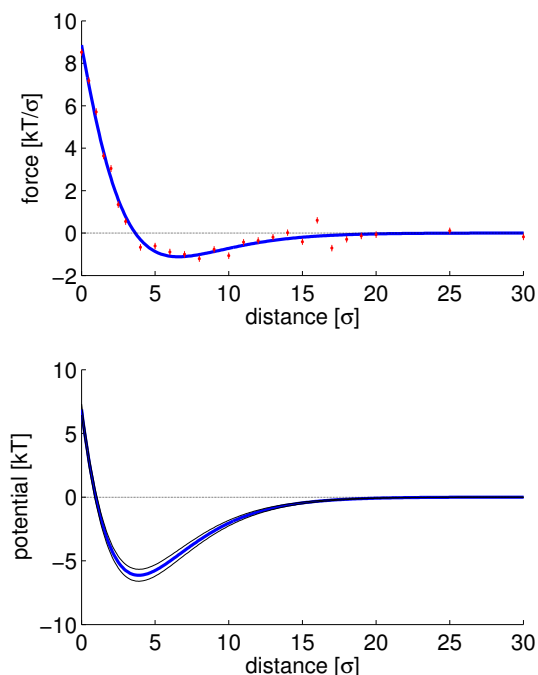
Figure 4.1: Effective force and pair potential between two complexes
In the upper half of the figure the force is plotted as a function of the
surface-surface separation of the cores at $\kappa = 0.4\ \sigma^{-1}$. Each core had a
central charge of $Z = 150$. The symbols represent the measured mean
force, the line shows a mean square fit. The lower part shows the pair
potential between two complexes obtained via integration and averaging
over a sample of fitted force functions. The thinner lines accompanying the
potential function denote the statistical error of the mean of the potential.

4.1.2 Interaction potential

The pair potential of the two tail sphere complexes can be determined by integrating
the function that was obtained by the least squares fit to the force data as explained
in the previous section.

By integrating the force functions obtained from fitting the measured data, one has
to consider, that the fit might only yield physical results in the region, where data
is available. Since the interaction is screened for long distances, the fitting function
was set to zero for distances which exceed the sampled space. The measured data
justifies this truncation: In the set of data shown in fig. 4.1 no effective interaction
can be determined for distances larger than approximately 20 σ, while the fit uses data
measured up to a distance of 30 σ.

The interaction potentials, which were determined in that way, are shown in fig. 4.2
for different salt concentrations as a function of the surface separation. The repulsion
due to sphere-sphere and excluded volume interaction dominates in the short distance
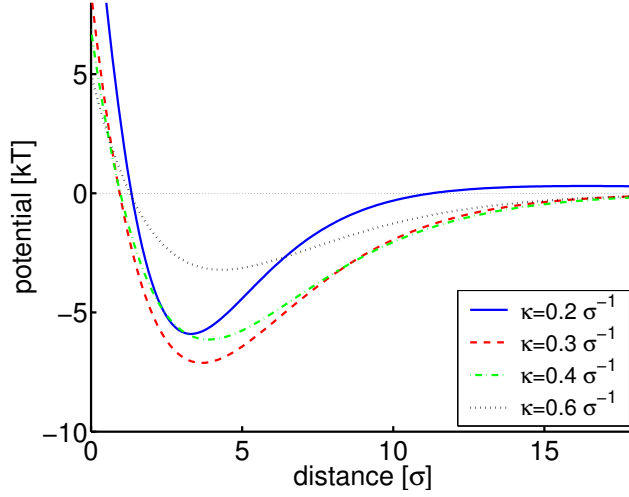
Figure 4.2: Interaction potential for the full chain model with $Z = 150$
The potential is plotted along separation of two complexes for different κ.
Each curve corresponds to a different κ as indicated on the legend. A steep
decrease of the potential is followed by the minimum. Due to screening
effects the potential rises again for larger distances and approaches zero.

region. With increasing distances all potentials decrease and show a negative minimum.
Remarkably the position of this minimum is hardly affected by the salt concentration.
The depth decreases with increasing κ until it reaches the maximal value at $V_{\min} \approx$
$-7 \ kT$ for $\kappa = 0.3 \ \sigma^{-1}$ at $d \approx 4 \ \sigma$. By increasing κ above this value, the minimum
flattens out again. At even higher distances, the potentials approach zero. Only in the
case of $\kappa = 0.2 \ \sigma^{-1}$ the potential raises once again and becomes positive. This effect
is due to the monopole-monopole repulsion of the two complexes. Since the screening
in this case is quite low, the monopole interaction is longer ranged in this case, which
corresponds to model 1 in fig. 2.11. To verify this we compare in fig. 4.3 the interaction
potential of the full tail complex with that of the bare monopoles, which corresponds
to the interaction of model 1 from fig 2.11. We find that for $\kappa = 0.2 \ \sigma^{-1}$ the two curves
come close for longer distances and show there a similar behavior. The corresponding
potential of the full chain model is also represented. Both curves approach each other
for long distances.

Fig. 4.4 presents the value of the minimum potential as a function of the core-core
separation. The minimal potential $V_{\min}$ can be found at $\kappa = 0.3 \ \sigma$. The dependence
of the position $d_{\min}$ of $V_{\min}$ on κ is presented in fig. 4.5. With increasing values
of κ the position of the minimum potential shifts continuously to higher core-core
separations. For $\kappa = 0.2 \ \sigma^{-1}$ $d_{\min}$ is approximately 3.3 σ and increases to $d_{\min} \approx 4.3 \ \sigma$
for $\kappa = 0.6 \ \sigma^{-1}$.
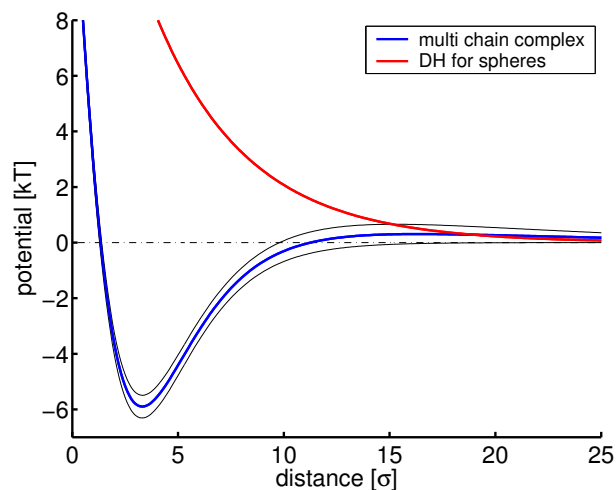
Figure 4.3: Interaction potential of the full chain model and bare monopole repulsion

The blue curves shows the interaction potential of the full chain model for $\kappa = 0.2 \ \sigma^{-1}$, also shown in figure 4.2. The black curves represent the statistical error of the potential. The red curve represents the Debye-Hückel potential between two spheres, carrying the same net charge.
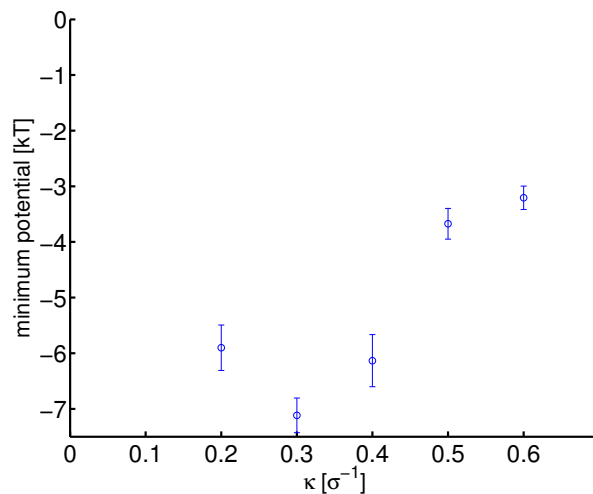
Figure 4.4: Positions of the minimum potential as a function of κ

The minimum potential V_{min} is presented as a function of κ. For low values of κ V_{min} increases with increasing κ until it reaches its minimum at $\kappa = 0.3 \ \sigma^{-1}$. For higher values of κ V_{min} increases with increasing κ.
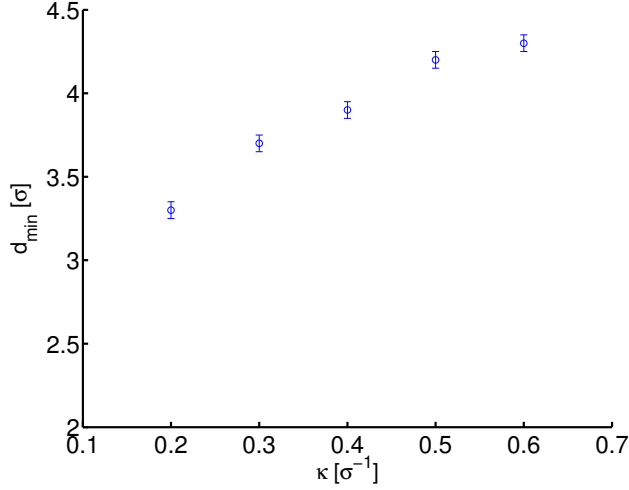
Figure 4.5: Minimum potential as a function of κ
The core-core separation $d_{\min}$ featuring the minimal interaction potential
is presented. For all values of κ $d_{\min}$ increases with increasing κ.

4.1.3 Statistical properties of the chains

In this study we also measure the statistical properties of the chains of a pair of complexes for the range of the core separation d from 0 to 15 σ and values of κ from 0.1 σ^{-1} to 0.6 σ^{-1}. Since we already studied these properties for the single complex in section 3.4, we are now interested in the impact of the interaction of the complexes on the chain configurations. We confine our measurements on the four chains of each complex, which are located on the side of the sphere, which is turned towards the neighbor complex. The measurements of the radius of gyration R_{G} and the end-to-end distance R_{EE} are performed analogous to the measurements for the study for a single complex presented in section 3.4.

The result for R_{G} is presented in fig. 4.6. For low values of κ a slight increase of R_{G} with increasing d can be detected. For higher core separations R_{G} reaches a plateau, which is independent from d. For high core separations both complexes do not interact anymore, therefore the values of the plateaus here represent the values of R_{G} obtained for the single complex for corresponding values of Z and κ. For $\kappa > 0.3$ κ^{-1} R_{G} is constant for all core separations. Also here the plateau value corresponds to the value of R_{G} of isolated complexes.

Fig. 4.7 presents the end-to-end distance of tails facing the neighbor complex. The behavior, which can be observed here, is similar to that in case of the radius of gyration described above. Also here a slight increase of R_{EE} with increasing core separation can be detected for low values of κ at low d. For higher values of the core separation, R_{EE} reaches a plateau, whose value corresponds to the end-to-end distance of tails of an isolated complex. For $\kappa \geq 0.4$ σ^{-1} R_{EE} is independent of the core separation, indicating no influence of the pair interaction of the complexes on the tail configuration. Also
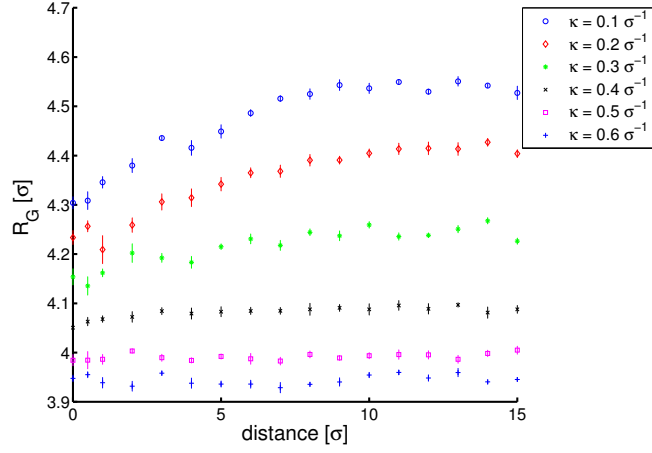
Figure 4.6: Radius of gyration

In this figure the radius of gyration of the tails, which are facing the neighbor complex is presented. For $\kappa \leq 0.3 \ \sigma^{-1}$ a slight increase of R_G with increasing d can be detected for low values of d. For higher values of d a plateau, corresponding to R_G of the tails of isolated complexes, can be found. For higher values of κ no change of R_G can be detected in the investigated range of d.
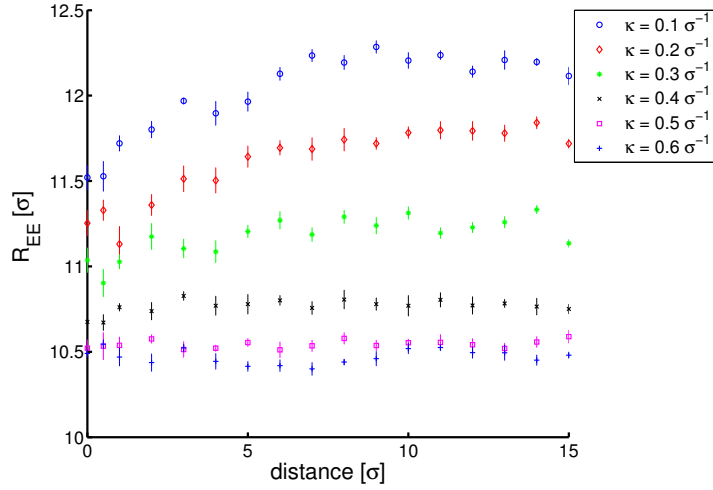
Figure 4.7: End-to-end distance

The end-to-end distance of tails facing the neighbor complex is shown. Similar to the behavior of R_G, which is described above, the pair interaction has only an impact in the region of $\kappa \leq 0.3 \ \sigma^{-1}$ and $d \leq 3 \ \sigma$. For parameters, which are outside of this region, the values for tails of an isolated complex are found.

here the value obtained for R_{EE} is in good agreement to that obtained for the case of an isolated complex.
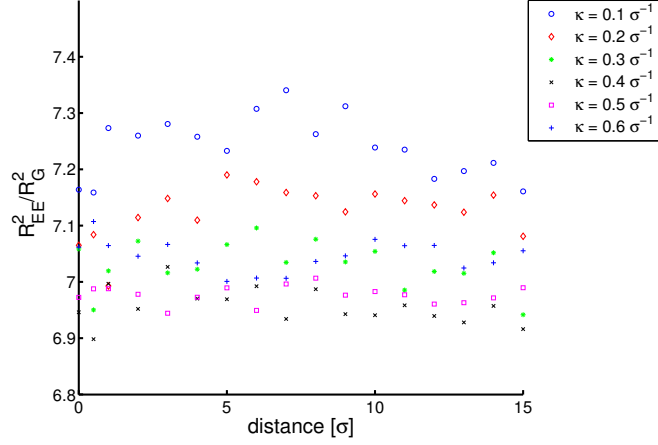
Figure 4.8: $R_{\mathrm{EE}}^2/R_{\mathrm{G}}^2$

The ratio $R_{\mathrm{EE}}^2/R_{\mathrm{G}}^2$ for tails facing the neighbor core is presented. A dependence of the ratio on the core separation cannot be detected. With increasing κ $R_{\mathrm{EE}}^2/R_{\mathrm{G}}^2$ decreases in accordance to the findings presented in section 3.4. No influence of the interaction of the complexes on the shape of the tail configurations can be detected.

The ratio $R_{\mathrm{EE}}^2/R_{\mathrm{G}}^2$ of the tails facing the neighbor core is shown in fig. 4.8. The ratio is constant for all values of d, indicating that the influence of the interaction of the complexes on the shape of the tails is negligible. The obtained values differ slightly for different values of κ, reflecting the results for a isolated complex presented in section 3.4.

As we can see from the data presented here, the shape of the configurations of the tails of interacting complexes differs only slightly from configurations, which can be observed in the case of isolated complexes. However we will see, that the overall conformation, formed by all monomers of a complex, differs for interacting complexes significantly from those observed in the case of an isolated complex. As an observable we choose the mean deviation D_{CM} of the center of mass (CM) of all monomers of a complex from the center of the sphere towards the neighbor complex:

$$D_{CM} = \frac{1}{8N}\langle \sum_{i=1}^{2} \sum_{j=1}^{8N} (\vec{r}_j^{\,i} - \vec{r}_{CS}^{\,i}) \cdot \vec{e}_{ss}^{\,i}\rangle \tag{4.2}$$

Here $\vec{r}_j^{\,i}$ denotes the position of the jth monomer of the complex i, $\vec{r}_{CS}^{\,i}$ is the center of the core of complex i, $\vec{e}_{ss}^{\,i}$ is the unit vector from the center of core i to the center of the neighbor core. N is the number of monomers of a single chain.

The result is presented in fig. 4.9: For the case of $\kappa = 0.1\ \sigma^{-1}$ the deviation has its maximal value of about $2.2\ \sigma$ at very low core separations. With increasing core
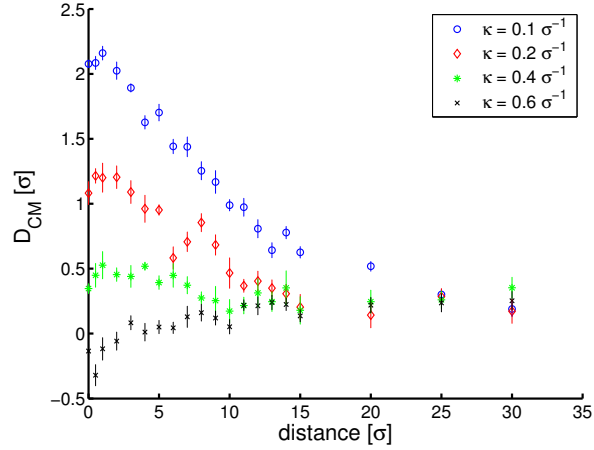
Figure 4.9: CM position of the monomer cloud of an entire complex
The mean deviation of the center of mass of the monomer cloud from the
center of the sphere of an entire complex is presented as a function of the
core separation. For $\kappa < 0.4\ \sigma^{-1}$ a significant deviation can be found at low
core separations. The effect is maximal at $\kappa = 0.1\ \sigma^{-1}$ and decreases with
increasing κ. Furthermore the effect appears to decrease with increasing
core separation.

separations the mean deviation of the CM decreases linearly with the distance. At
$d \approx 25\ \sigma$ finally no deviation can be detected anymore. In the case of $\kappa = 0.2\ \sigma^{-1}$ the
maximum at low core separation is about $1.2\ \sigma^{-1}$. The deviation decreases linearly
with increasing d, until it is decayed at $d \approx 15\ \sigma$. For $\kappa = 0.4\ \sigma^{-1}$ the maximum at
low core separations is about $0.5\ \sigma^{-1}$ and decays at a core separation of about $15\ \sigma^{-1}$.
Finally for $\kappa = 0.5\ \sigma^{-1}$, a deviation of the CM of the monomer cannot be detected
anymore for any value of the core separation.

So despite the fact, that almost no significant impact of the complex interaction on
the configurations of the single tails can be detected, we can observe a slight shift of
the center of mass of the monomers towards the interaction zone between the com-
plexes. Due to the screening this effect decreases with increasing κ and increasing core
separation.

4.1.4 Second virial coefficient

Another measurement for the interaction of particles in dilute solution is the second
virial coefficient A_2. The procedure to obtain A_2 experimentally is described in the
appendix A.1. In order to obtain A_2 from our computer simulation we use equation
4.3 (see also appendix A.2):

$$A_2 = 4v_0 + 2\pi \int\limits_{2a}^{\infty} (1 - \exp(-V(r)/kT))r^2 dr \tag{4.3}$$

Here $V(r)$ is the interaction potential described in the preceding section. The cores of the complexes are considered as hard spheres with radius a and volume v_0. Since in the simulation a Lennard Jones potential between both cores is not included, $V(r)$ represents the electrostatic interactions involving the cores, the Lennard Jones interaction between the monomers and the cores and the chain interaction mediated by the grafting monomers.

Fig. 4.10 shows the second virial coefficient of the sphere tail complexes as a function of κ. This result was obtained by using the potential energy functions of section 4.1.2 and plugging it into equation 4.3. The outcome of A_2 is quite sensitive to the minimum
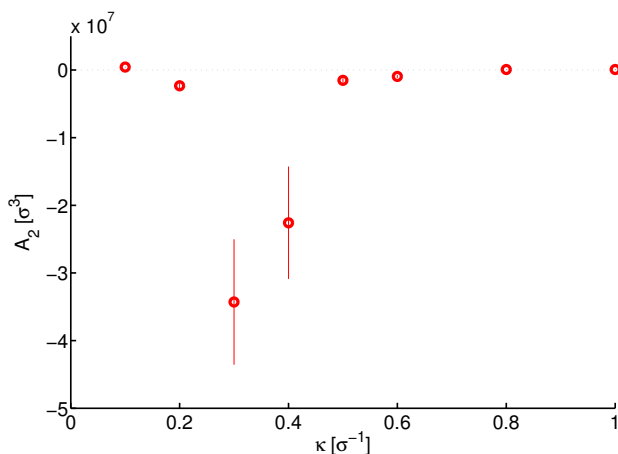
Figure 4.10: Second virial coefficient for the sphere tail complexes. With increasing salt concentration the second virial coefficient decreases due to the interaction observed in sections 4.1.1 and 4.1.2. The minimum at $\kappa = 0.3\ \sigma^{-1}$ corresponds to the lowest minimum value of the interaction potentials.

of $V(r)$. This was the main reason, that a fit has to be used to interpolate between the measured data points describing the force instead of using a spline function. The obtained potentials are discussed in the previous section. For small κ A_2 is positive, however with κ increasing above $0.15\ \sigma^{-1}$, A_2 drops dramatically until it reaches its minimum at $\kappa = 0.3\ \sigma^{-1}$. Now the screening between the particles becomes the dominant part forcing A_2 to rise again. For high salt concentrations the electrostatic interactions are screened. This results in a positive second virial coefficient, due to the excluded volume interactions of the monomers and the spheres.

4.1.5 Possible explanations: Patchiness and tail effects

The non monotonic behavior of the interaction potential observed in section 4.1.2 could have its origin in two different effects, as already discussed in section 2.2. As we saw there, multipole interaction can give rise to attractive interaction. However, also polyelectrolyte chains are capable of mediating attraction between two oppositely

charged walls. Our chain sphere complex, a charged sphere with polyelectrolyte chains grafted on the surface, has a multipole moment, which could possibly be accountable for attractive interaction between two of these complexes. However also the grafted chains could be responsible for the observed attraction.

In order to discriminate between these effects, simulations and measurements were also performed using the models already introduced in section 2.2.3. The results will be shown in the next two sections.

Attraction due to the charge distribution

To investigate the interaction due to the charge distribution of the complex, model 2 from section 2.2.3 was used. As shown in fig. 2.11, here each chain is collapsed to one single monomer carrying the complete charge of the chain. The relative positions of the charge patches are fixed via the match potentials. The central charge of the sphere is unchanged with respect to the full chain model. Fig. 4.11 shows the interaction potential of two of these patched complexes for different salt concentrations. Also in this model all curves have a region which shows attraction. The overall minimum can be found at $\kappa = 0.4 \ \sigma^{-1}$ to be $V_{\min} \approx -10 \ kT$ at $d \approx 0.5 \ \sigma$. It is slightly deeper than in the case of the full system. For all salt concentrations the position of the minimum is at a sphere-sphere separation of less than σ, which is clearly closer than in the case of the full system. Analog to the full system, also for the patch system the second
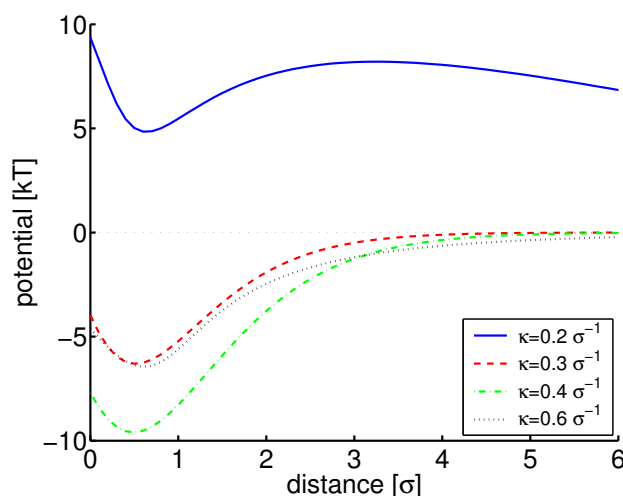
Figure 4.11: Interaction potential of two spheres decorated with patches

For small separation distances a minimum can clearly be seen. However the range of attraction is much more narrow than in the case of the sphere tail complex. The overall minimum value for the interaction potential can be found at $\kappa = 0.4 \ \sigma^{-1}$ at about $-10 \ kT$.

virial coefficient can be determined. Fig. 4.12 shows A_2 as a function of κ. With increasing salt concentration A_2 decreases until κ becomes approximately 0.25 σ^{-1}.

Now the second virial coefficient drops dramatically until it reaches it minimum at about $\kappa = 0.35 \, \sigma^{-1}$. For higher values of κ a sharp rising of A_2 can be observed until the curve approaches its asymptotic value for high salt concentrations. In light of this data,
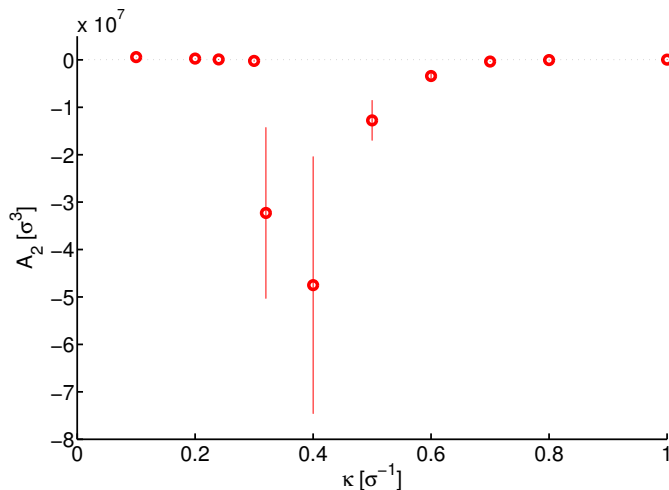
Figure 4.12: Second virial coefficient of patch complexes along A_2 is plotted as a function of κ. For small κ A_2 decreases slowly until $\kappa \approx 0.30 \, \sigma^{-1}$. Now follows a steep decrease of A_2 to the minimum value at $\kappa \approx 0.35 \, \sigma^{-1}$. For higher κ A_2 increases strongly until $\kappa \approx 0.5 \, \sigma^{-1}$. By further increasing κ A_2 approaches its asymptotic value for high salt concentration.

one might speculate that it is in fact the patchiness of the charge distribution of the NCPs, that can explain the experimentally observed nucleosome properties described in the sections 4.1.1-4.1.4. We will, however, show in the next section, that tail induced attraction is also present and yield features very similar to those observed here.

Another interesting feature of two patch complexes is the relative orientation of the structures. In order to be able to express the arrangement quantitatively, three angles were chosen, which describe the position of one patch complex. These angles refer to the cube, which is formed by the eight charge patches on the surface of the core. They are related the position of the corner, edge and plane closest to the neighbor complex.

The corner angle is simply the angle between the connecting line of both complexes and the vector from the core center to the charge patch closest to the neighboring core. The edge corner is defined as the angle between the connecting line and the sum of the two charge patches closest to the neighbor. Analog the plane angle can be found. It corresponds to the angle between the connecting line of both cores and the normal through the plane of the cube facing the neighbor patch complex. The normal vector can be obtained by adding the four vectors from the core center to the corresponding charge patches.

With these angles the position of the patch complex can be classified into three cases, depending on which angle of the three is smallest. If the corner angle is smallest,
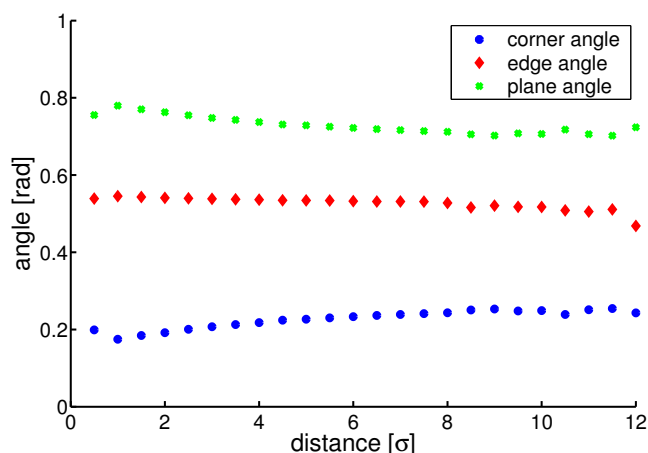
Figure 4.13: Relative position of the patch complexes at zero temperature

The three angles, which are plotted as a function of the surface-surface separation of the two cores, define the relative position of both patch complexes. Since the complexes behave in a symmetric way, only data for one structure is shown. See the accompanying text for the definition of the corner, edge and plane angle.

a corner of the cube points in the direction of the neighbor core. In this case the patch on that corner can come very close to the neighboring core. Here the enhanced interaction with this 'special' patch is favored over weaker interaction with the others. Another possibility is the case, that the edge angle is smallest. Now two patches are considerably closer to the neighbor core and are therefore favored with respect to the others. In the case of a small plane angle, a side of the cube faces the neighbor core. Now four patches are in close distance to the neighboring sphere.

Fig. 4.13 shows the measured angles for the case of zero temperature. The angles are plotted versus the surface-surface separation of the cores. Each color corresponds to an angle as shown in the legend. Since the values for both complexes turned out to be symmetric, the results for only one complex are shown. For all measured distances the corner angle is smallest, indicating that the cubes of both complexes face the corresponding neighbor with a charge patch. The mutual interaction of these patches leads to the non zero value for the corner angle. The rise for the corner angle, accompanied with a drop for the edge and plane angles, for very small separations is due to the excluded volume interaction of the charge patches with the neighboring core.

Tail induced attraction

In the previous section we found mutual attraction between patch complexes. This leads to a negative second virial coefficient in that case. However, also the single chain model shows a similar behavior, as we will see in this section.

   The model used is already described in section 2.2.3. It is represented by pair number 3 in fig. 2.11. In this case all tails except one are removed from the pair. The remaining chain is grafted on the surface of one sphere on the connecting line of the centers of the two complexes. In order to prevent the chain from moving out of the interaction zones of both centers, the chain bearing complex was also not allowed to rotate. Finally the central charges of the cores were reduced to 70 elementary charges in the case of the bare sphere and to 80 charges for the tail bearing complex in order to equal the net charge to those of the complexes carrying eight tails. Fig. 4.14 shows the interaction
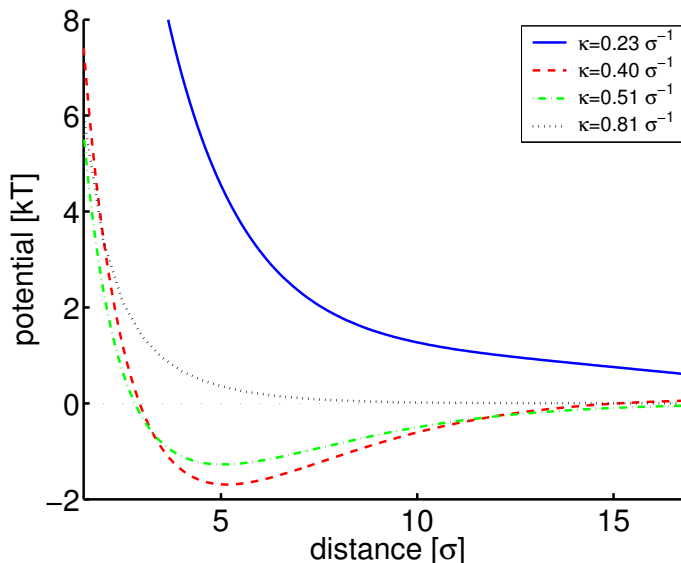
Figure 4.14: Interaction potential of a single tail complex
For low salt concentrations no attraction can be observed. In the case of higher κ a minimum appears at a separation distance $d \approx 5\,\sigma$. Compared to the eight chain model it is shifted to higher separation distances. With a value of $V_{\min} \approx -2\,kT$ the minimum is also shallower than is the case of the full chain model.

potential of the one tail system. For low salt concentrations no attraction can be observed. In this case the repulsion decays monotonic. By increasing κ, however, a minimum appears at a core separation of approximately $5\,\sigma$. The minimum is found for $\kappa = 0.45\,\sigma^{-1}$ with the value $V_{\min} \approx -2\,kT$. Compared to the full chain model it is shifted to larger separation distances and is shallower. By increasing κ further the observed attraction vanishes again, similar to the case of the full chain model.

   Fig. 4.15 shows the second virial coefficient as a function of κ for the single tail model. Due to the monomer interaction and entropic repulsion of the grafted chain it is positive for small separation distances. By increasing κ A_2 increases to the minimum at $\kappa = 0.4\,\sigma^{-1}$. For even higher κ A_2 increases and approaches its limit for high salt concentration.

   Apparently a single tail is capable of inducing an attraction that shows again similar features as the patch model and the full chain model. This raises the question, whether
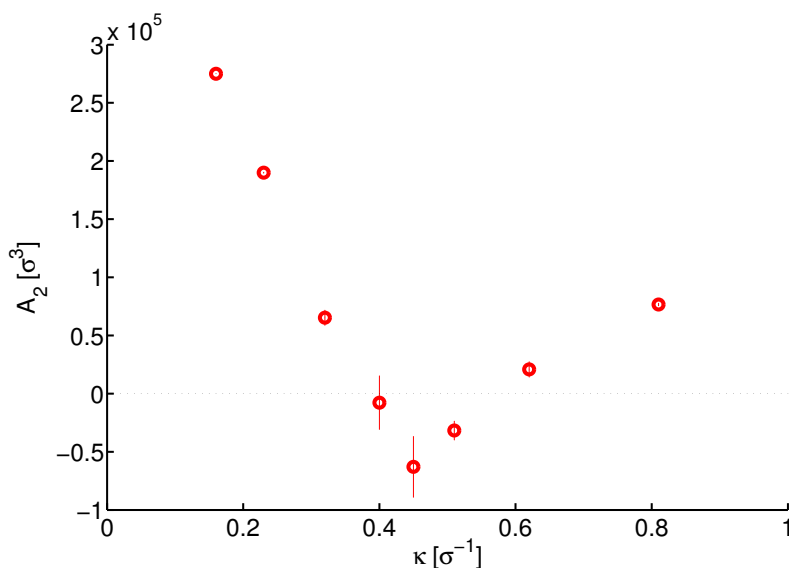
Figure 4.15: A_2 for one tail model along κ

For low κ A_2 decreases with increasing salt concentration. At $\kappa = 0.4 \; \sigma^{-1}$ a minimum is reached. For higher salt concentrations A_2 increases again.

the attraction of the full system should be interpreted as being based on a tail effect or on the interaction between patches. We will show in the next section that both effects are qualitatively different with respect to the range of the interaction. This will allow us to distinguish between these effects and ultimately will let us resolve the question, whether the attraction between multi tail complexes is mainly based on tails or patches.

4.1.6 Comparison of the range of the potentials

In the last section we found, that all of the proposed models feature a non monotonic dependence of the interaction potential on the salt concentration. However the potentials of the various models are obviously different with respect to the range of the interaction. This issue will be addressed in this section.

Fig. 4.16 shows the negative part of the interaction potential of the full chain model as a function of the separation of two complexes on a semilogarithmic scale with the statistical error. The red line indicates the screening function $-C \exp(-\kappa r)$. Here r is the separation distance and C is a factor that we choose such that the line passes the minimum of the potential.

In the case of small κ the interaction decays faster than the screening. However, already at $\kappa = 0.3 \; \sigma^{-1}$ the potential clearly decays slower than screening effects alone would suggest. This behavior becomes even more distinct when going to higher values of κ which are also shown in the plot.

The case of the patch model, shows exactly the contrary characteristics. As shown in fig. 4.17, the interaction potential decays now much faster than bare screening effects
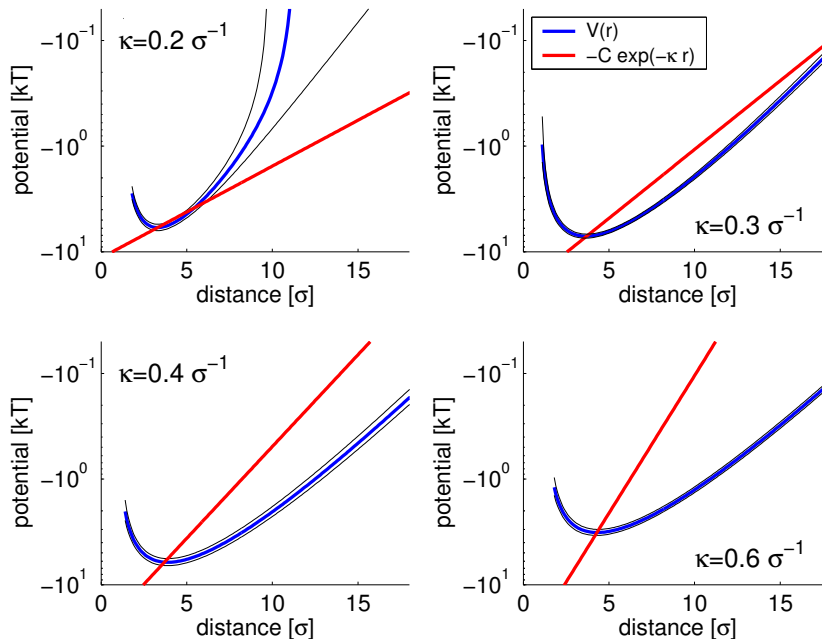
Figure 4.16: Interaction potential vs. Debye Hückel screening for the full complex

The plots show the negative part of the interaction potential from fig. 4.2 as a function of the separation of the cores for the full chain model on a semilogarithmic scale. Each plot corresponds to a different value of κ as indicated. The red line corresponds to the screening an exponential decay as expected from pure Debye Hückel screening. For $\kappa = 0.2 \; \sigma^{-1}$ the potential decays faster than the Debye Hückel screening, however for higher values of κ the decay of the potential is clearly slower than electrostatic screening. The longer range of the interaction as compared to the screening clearly indicates a tail induced effect.

would indicate. The fast decay might be a indication of the nature of the dominating interaction in this case. The observed attraction could be due to a electrostatic correlation of the charges. This effect is known to decay exponentially with distance [83].

The comparison for the single tail model is shown in fig. 4.18. For all presented values of κ the interaction potential decays slower than the Debye Hückel screening for small distances. For large distances, the slope of each curve exceeds the screening at a certain point. With increasing salt concentration the position of this point shifts to higher distances. For $\kappa = 0.40 \; \sigma^{-1}$ it is located at $r \approx 10 \; \sigma$ while it is at $r \approx 15 \; \sigma$ for $\kappa = 0.62 \; \sigma^{-1}$.

Apparently the models differ considerably with regard to the range of their attractive interactions. Furthermore the interaction decays only in the case of the single chain model and in the full chain model slower than the screening, indicating the importance
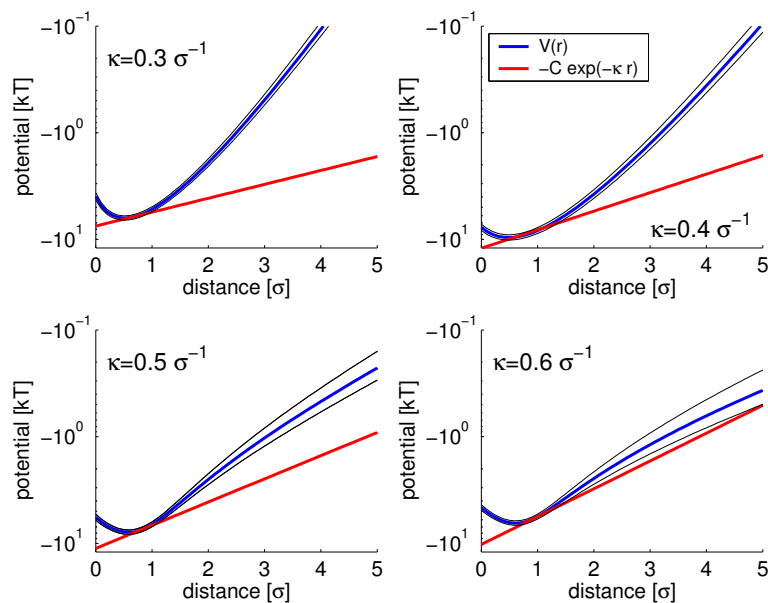
Figure 4.17: Interaction potential and screening for the patch model
Each plot shows the interaction potential corresponding to the indicated
value of κ on a semilogarithmic scale. The red line provides a comparison
to electrostatic screening $\exp(-\kappa r)$. In all cases the attracting potential
decays faster than bare screening would indicate.

of the tails for the interaction of the full chain model. Apparently the pair interactions
of the chain models and the patch model differ qualitatively, giving raise to the idea,
that the tail interactions and not the charge correlations of the system are responsible
for the interaction observed for the full chain model.

In the next chapter the nature of the chain interaction and its influence on the overall
attraction will be analyzed in detail.

Summary

For our full chain model we do not only find an unfolding process similar to that observed in the experiment, we also find attractive interaction which is dependent on
the salt concentration. The investigation of these attractions are the subject of this
chapter. In order to obtain the pair potential between two complexes, MD simulations
were performed and the effective force between the complexes were measured for different core-core separations of the complexes. The obtained data was fitted in order to
obtain a function of the effective force. By integration of the force function the effective
pair interaction can be obtained, which is presented in fig. 4.2. With increasing core
separation the pair potential decreases for all presented values of κ, until it reaches a
minimum at a surface separation of about 3-4 σ. The minimum value of the potential
is dependent on κ: For $\kappa < 0.3\ \sigma^{-1}$ the minimum value decreases with increasing κ
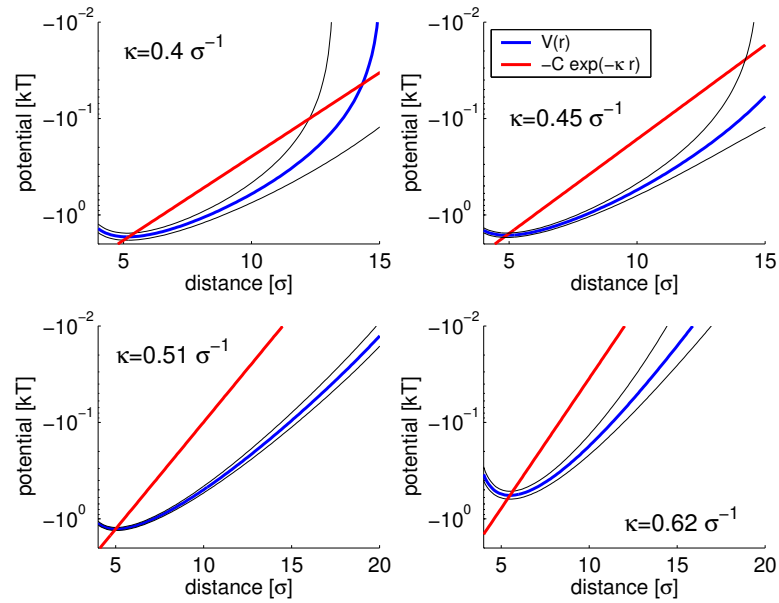
Figure 4.18: Interaction potential and screening for the one tail complex

The potential is compared to the screening function on a semilogarithmic scale. Each subplot features data according to the indicated κ. In all cases the attraction decays slower with increasing separation than the screening would suggest over a wide range of r.

until the minimal value at $\kappa = 0.3 \ \sigma^{-1}$ is reached. For values of κ larger than $0.3 \ \sigma^{-1}$ the minimum in the potential increases with increasing κ. For small values of κ, it even becomes positive again, due to the monopole interaction of the cores.

Using the effective pair potential of the chain sphere complexes, the second virial coefficient A_2 can be computed. A_2 for the chain sphere complex depends on κ. For low values of κ A_2 is dominated by the monopole repulsion of the cores and therefore positive. With increasing κ a steep drop in A_2 to negative values can be observed at $\kappa = 0.3 \ \sigma^{-1}$. For $\kappa > 0.4 \ \sigma^{-1}$ A_2 rises again with increasing κ. For $\kappa > 0.6 \ \sigma^{-1}$ the excluded volume interaction becomes the dominant part of the interaction resulting in positive values of A_2.

According to our explanations in section 2.2 the observed attraction can either be due to interaction induced by the discrete charge distribution of the complexes or to tail interaction. In order to be able to distinguish between the contributions of these effects, we performed MD simulations using the patch and the single sphere model as explained in section 2.2.3. In both cases an attractive pair potential can be found. At the same time the strength of the attraction is dependent on the salt concentration. Also A_2 is dependent on the salt concentration in both cases. For the patch model as well as the single chain model the second virial coefficient shows qualitatively the same non-monotonic behavior as we observed or the multi chain complex.

In order to be able to compare the range of the potentials of the different models, we presented the potential functions together with the screening. For the full chain model we find two different scenarios: For $\kappa < 0.3\ \sigma^{-1}$ the attraction decays faster than the screening. According to chapter 3 the tails are not yet fully separated from the cores under these conditions. However for values of κ larger or equal $0.3\ \sigma^{-1}$, which is a conditions corresponding to the separation of the tails, the attraction decays slower than the screening would suggest. In the case of the patch model, the attraction decays for all values of κ faster than the screening would suggest. However for the single chain model a decay slower than the observed screening can be detected for $\kappa \geq 0.4\ \sigma^{-1}$.

The tail systems differ qalitatively from that of the patch system regarding the range of the interaction. While the interaction induced by the patches declines faster than the screening, the tail induced interactions decay slower. Apparently the contribution to the interaction is here more important than those of the charge correlations. In the next chapter we will analyse the tail mediated interaction and confirm this idea.

5 Tail bridging

In the previous chapter the interaction potentials of the full chain model, the single chain model and the patch model were described and compared both regarding to the intensity as well as to the range. In all three cases mutual attraction of the complexes were found. Also the second virial coefficient A_2 showed a non-monotonic behavior as a function of the salt concentrations in all three cases. However the interactions differed with regard to their range. The attraction of the patch model decayed much faster than the screening due to the salt concentration would require, while the chain models yielded attraction over a wider range than the screening would suggest. This observation confirms the idea, that the dominant interaction in the case of the full chain model does not originate from correlations of charge patches, but from tail induced effects. In order to prove this, the tail configurations and their contributions to the attraction will be investigated in more detail in this chapter.

5.1 Monomer distribution

The interaction of multi tail complexes decays slower than the screening of the salt suggests. This is a hint, that the tails play an important role in the interaction of these complexes. Any effect due to the charge distribution is subject to screening and therefore decays at least as fast as the screening increases. This effect was shown for the patch model.

To get a deeper understanding of these effects, the monomer distribution of the multi tail complexes was investigated. The effect to be addressed in this chapter is tail bridging: A tail separates from the core, to which it is attached, due to thermal fluctuations. Now its free end can come into the zone of influence of the neighboring core. The charged monomers at the free end of the chain can get attracted to the other core and condense onto its surface. At the same time, due to the screening, they do not interact electrostatically with their home core anymore. A connection of the two complexes is now established. Since both cores have the tendency to get more monomers condensed on their surfaces, this bridge will give rise to an attractive force.

In order to identify such bridges, the bridging monomers have to be found. In the first step, we focus on the monomer closest to the neighboring complex in a given configuration. If this monomer is too far away from the other core to establish a bridge, also no other monomer in this configuration can do so and the complexes are not connected. However, if this monomer is condensed on the other core, a bridge is identified. For the analysis on bridging presented in this chapter, we used the configurational data from the simulations presented in chapter 4, i.e. we averaged over 10 simulations of 10^6 time steps with independent initial conditions. Fig. 5.1 shows the probability density

to find the monomer closest to the alien core around the alien core. The different curves represent different distances of separation between the cores. The data were obtained from $4 \cdot 10^4$ configurations for each curve. The x-axis in this plot gives the distance from the alien surface, where the closest monomer was found.
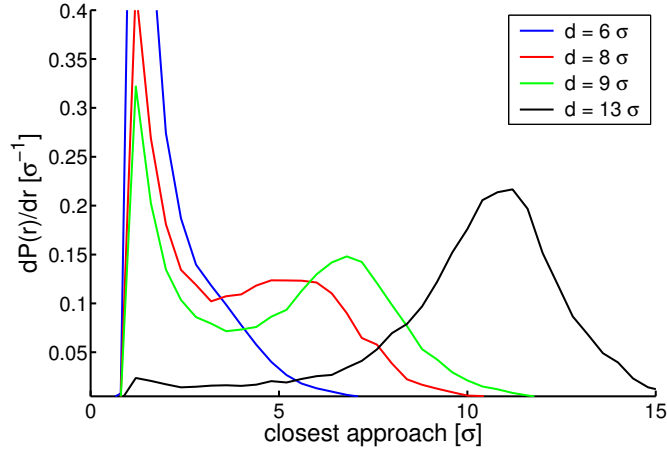
Figure 5.1: Closest approach of monomers to the alien core
The different curves correspond to different surface-surface separations d of the two complex cores. For $d = 13 \, \sigma$ only few configurations show tail bridging. By reducing the separation to $d = 9 \, \sigma$ a second condensation peak can be found on the surface of the neighboring core. By further reducing the distance to $d = 8 \, \sigma$ this effects is even enhanced. Finally in the case of $d = 6 \, \sigma$, the condensation peak on the home core has vanished. Bridging can now be found for almost all configurations.

In the case of large separation only few chains find their way to the neighboring core. This is shown by the curve representing $d = 13 \, \sigma$. Most monomers stay close to their 'own' complex core, what results in the condensation peak at about $11 \, \sigma$. By reducing the separation to $d = 9 \, \sigma$, a second peak can be observed at the surface of the neighbor core. The minimum between the two peaks shows, that it is less favorable for monomers to stay in between the balls than to condense on either their own or on the neighboring core. By reducing the separation further to $8 \, \sigma$ the effect of condensation on the neighbor core becomes even stronger. A second peak of condensation on the home complex is still visible. Finally, in the case of $d = 6 \, \sigma$, most configurations show a bridge between the two complexes. The second peak of condensation has disappeared.

After having demonstrated the occurrence of tail bridging by measuring the distance of closest approach, we study the conformations of bridge-forming tails. Fig. 5.1 allows us to establish a criteria to identify tails that form bridges. A minimum of monomers can be observed at the distance $r \approx 3.6 \, \sigma$ and does not change for different separations d. This suggests to define a bridging chain as a chain with a closest approach of one of its monomers to the neighboring core smaller than this threshold. This definition of a bridge will be used throughout this work.
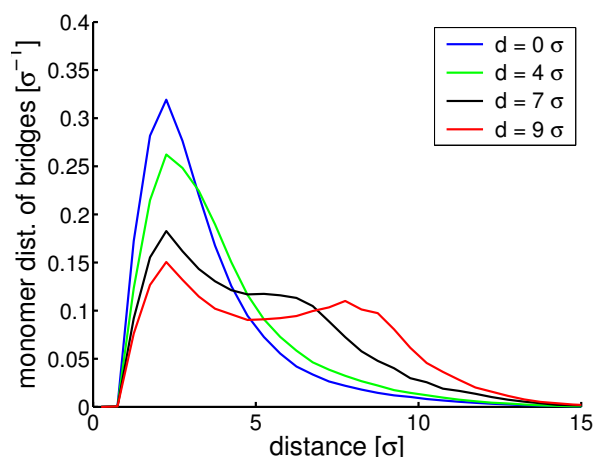
Figure 5.2: Monomer distribution of bridges

The distance of monomers from bridging chains from the surface of the grafting core is shown for different surface-surface separations. In the case of small separations like $d = 0$ and $d = 4\,\sigma$ only one peak can be observed because both surfaces are too close to allow a distinction. However for $d = 7\,\sigma$ a shoulder at $r \approx 7\,\sigma$ can be observed suggesting a second maximum due to monomer condensation on the neighboring core surface. For the largest separation $d = 9\,\sigma$ two maxima can be clearly distinguished. Obviously it is more favorable for the monomers to condense on one of the surfaces than to stay in between the complexes.

Fig. 5.2 shows the distribution of monomers of bridging chains for different separations of the surfaces of the cores. For small d the distribution is peaked at small distances. In this case the monomers can stay in the interaction zones of both cores at the same time. By increasing the separation to $d = 4\,\sigma$ the distribution smears out, but does not change significantly. The case of $d = 7\,\sigma$ the monomer distribution features a shoulder around the distance $r = 5\,\sigma$, suggesting the existence of a second attractor for monomers. Finally the curve corresponding to $d = 9\,\sigma$ has two separate maxima. The second peak observed is due to monomer condensation on the surface of the neighboring core. So once a bridge is established between two complexes, it is possible for the chain to move more monomers onto the neighboring surface. The monomer density between the condensation zones is smaller, indicating that the monomers prefer condensation on any of both surfaces to staying between two complexes.

5.2 Frequency of bridges

In the previous section a criteria to identify bridges was established, namely that a chain approaches the alien core closer than $3.6\,\sigma$. Using this criteria, the frequency of bridges can be investigated quantitatively. Fig. 5.3 shows the number of bridges found during one unit of the LJ-time τ as a function of the surface distance for different values of κ
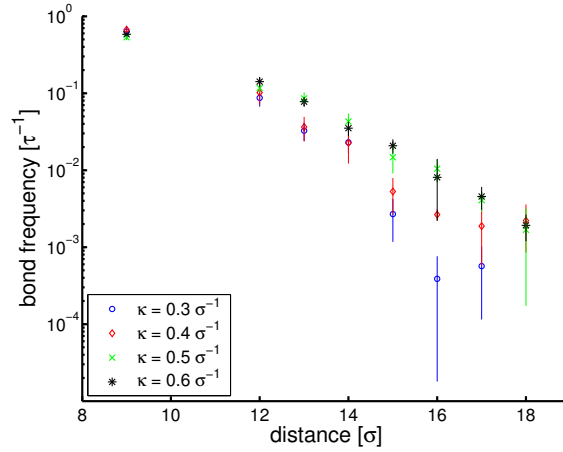
Figure 5.3: Frequency of bridges

The frequency of bridges is shown as a function of the surface separation for different values of κ as indicated in the legend. Increasing the core separation from $d = 9\ \sigma$ to $d = 18\ \sigma$ results in a dramatic decrease of the frequency of bridges of about three order of magnitude. Increasing of κ leads to an increase of the frequency of bridges.

on a logarithmic scale. For surface distances larger than $9\ \sigma$ the frequency decreases exponentially with the distance of the cores. In the region of $9\ \sigma\ <\ d_{\mathrm{ss}}\ <\ 18\ \sigma$ this effects adds up to a variation of the frequency of about three orders of magnitudes. With increasing salt concentration also a weak increase of the frequency of the bridges can be detected. What is the reason for this dramatic dependence of the bridging probability on the distance? As we will show in the next section, it can be understood in terms of the dynamics of bridges.

5.3 Dynamics of bridges

In principle, the decrease of the bridging frequency with increasing distance between the cores, which was presented in fig. 5.3, could be either a result of a corresponding decrease in the life time of the bridges or a result of their possibly decreased formation frequency. Also a combination of both of these effects could be possible. To check these possibilities we study in this section the dynamics of the bridges. Let us start with the life time.

In order to obtain the life time of the bridges, we checked at each time step, wether bridges were formed or decayed. This was done to prevent consecutive bridges formed by the same tail to be counted as the same bridge. The mean life time $\langle \tau_{\mathrm{Life}} \rangle$ of bridges is shown in fig. 5.4 as a function of the surface separation of the cores for different values of κ. In general the lifetime decreases with increasing core separation and increases with increasing κ. In the range of d_{ss} from $9\ \sigma$ to $18\ \sigma$ $\langle \tau_{\mathrm{Life}} \rangle$ varies about half an order of magnitude. The variation observed for the lifetimes of bridges is thus much smaller

than the variation observed in the occurrence of bridges. Consequently the frequency of the formation of new bridges must be important in order to explain the effect of tailbridging.
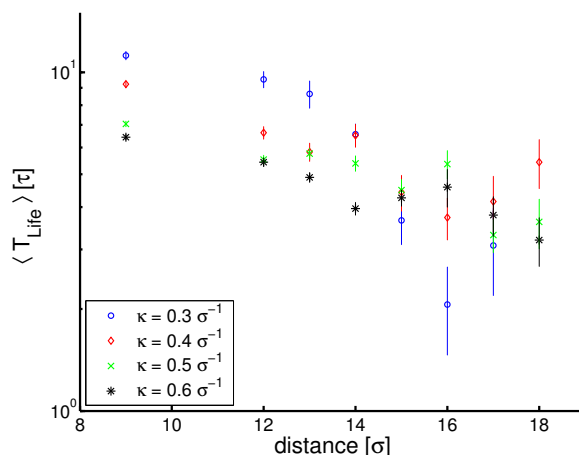
Figure 5.4: The life time of bridges

The mean life time of bridges is shown as a function of the core separation for different values of κ. A decrease in the life time of half an order of magnitude can be observed by increasing the core separation from $d = 9\ \sigma$ to $d = 18\ \sigma$. Increasing of κ also leads to an increase of the life time.

In the next section, we will investigate the formation of new bridges. We will also see, that the formation of new bridges is dependent on the adsorption energy of the charged monomers on the core surfaces. Furthermore we will introduce a simple model capable to explain most of the bridging dynamics.

The rate of formation of new bridges is shown in fig. 5.5 as a function of the distance of the core surfaces. For distances larger than $d = 10\ \sigma$ a decay of the formation rate exponentially to the surface-surface distance can be seen. As for the probability of bridges in fig. 5.3, the formation rate decreases via three orders of magnitude over the depicted range of the core-core separation. This shows, that it is the formation rate and not the life time of bridges, which is responsible for the strong variation in bond frequency with distance [1]

This dependence of the formation rate on the distance can be rationalized using a simple model. We assume the interaction of both complexes to be equal to the interaction of two charged planes with grafted polyelectrolytes. Furthermore we will consider the electrostatic interaction between a core and a charged monomer as a short ranged attractive potential with the minimum value of

$$E_{\text{Ads}}(\kappa) = \frac{Z l_B}{a(1 + \kappa a)} \tag{5.1}$$

---

[1]It should be mentioned, that the product $\langle \tau_{\text{Life}} \rangle \cdot$ (bond appearance rate) is the mean number of bridges. This number is asymptotically identical to the probability to have at least one bond, which is again the bond frequency presented in fig. 5.3.
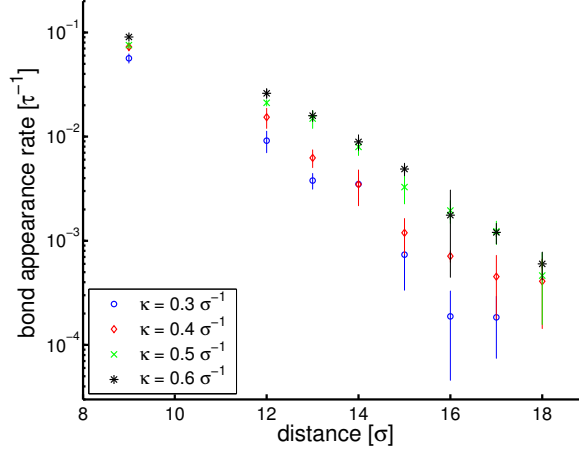
Figure 5.5: Formation rate of new bridges

The formation rate of new bridges is shown as a function of the core separation d. Increasing of the core separation leads to a decrease of the formation rate. In the range of $9\,\sigma < d < 18\,\sigma$ the formation rate shows a decrease of about 2.5 orders of magnitude. The formation rate increases with increasing values of κ. This effect is mainly due to the dependence of the adsorption energy of the charged monomers on κ. See the text for details.

close to the surface of the core. Equation 5.1 can be obtained by setting $r_{cm} = a$ in equation 2.17. Since the monomer is small compared to the core, the particle radius is neglected here. Due to the short range of the potential, the energy of one monomer can be written as

$$E_{\mathrm{monomer}} = \begin{cases} -E_{\mathrm{Ads}}(\kappa) & \text{in case of condensation} \\ 0 & \text{else.} \end{cases} \tag{5.2}$$

Finally, an occurring bridge is approximated by a straight line of monomers connecting both cores. This is illustrated in fig. 5.6. Here d_{ss} is the surface distance between two cores and d_{charge} is the contour distance between two charges on the chains. d_{charge} was set to $3\,\sigma$ for the simulations in this section. Obviously for the formation of a bridge over a gap of the length of d_{ss} it is necessary to separate at least $d_{\mathrm{ss}}/d_{\mathrm{charge}}$ monomers from the energetically favorable position near a core. One of these monomers will condense on the alien core, leaving $d_{\mathrm{ss}}/d_{\mathrm{charge}} - 1$ in the unfavorable position. Consequently the probability of the formation of a bridge should be proportional to the corresponding Boltzmann factor:

$$P_{\mathrm{Bridge}} \propto \exp(-E_{\mathrm{Ads}}(\kappa)(\frac{d_{\mathrm{ss}}}{d_{\mathrm{charge}}} - 1)/kT) = C(\kappa)\exp(-E_{\mathrm{Ads}}(\kappa)\frac{d_{\mathrm{ss}}}{d_{\mathrm{charge}}}/kT) \tag{5.3}$$

$C(\kappa)$ is only dependent on κ and does not change the exponential decay. In order to test the exponent extracted from this model, we fit the formation rate of new

$$d_{ss}$$
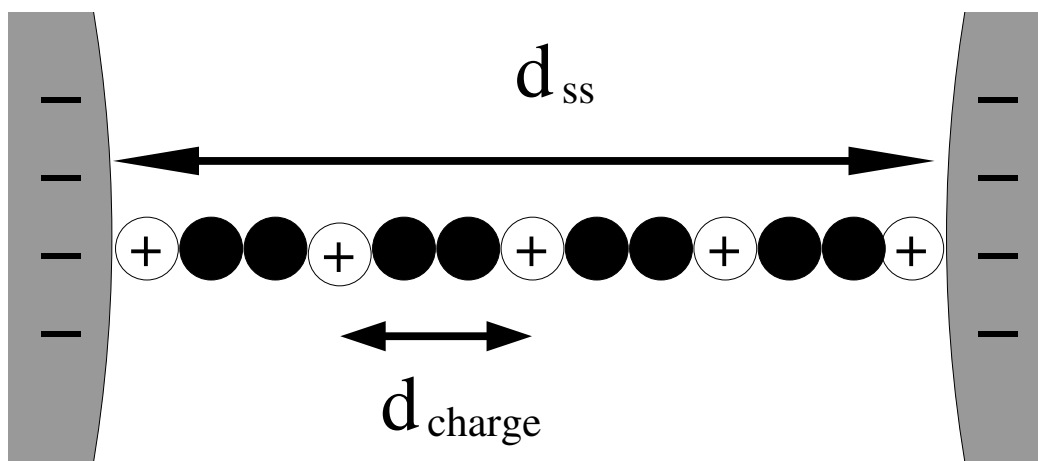
$$d_{charge}$$

Figure 5.6: Bridge formed between two sphere chain complexes
In order to form a bridge, it is necessary to separate charged monomers
from the favored positions near one of the cores. The number of charged
monomers prevented from condensing on a core is dependent on the core
separation d_{ss} and the separation between two charges on the chain d_{charge}.

bridges for core surface distances larger than 10 σ with the exponential function
$f(d_{ss}) = A \exp(-m_{meas} d_{ss})$ with the two parameters A and m. Fig. 5.7 shows the
fitted exponent m_{sim} from the simulated data divided by exponent extracted from the
described model $m_{theo} = -E_{Ads}(\kappa)\frac{d_{ss}}{d_{charge}}$ as a function of κ. For small values of κ
the exponent obtained from the simulation is in good agreement with the exponent
extracted from the model. For higher values of κ the measured exponent is smaller
than the theory would suggest. For this behavior entropic effects, which were neglected
in our model, might be responsible: Fig. 3.5 in section 3.3 shows the monomer dis-
tribution around a single complex. For higher salt concentrations more monomers can
be found away from the core. This behavior implies, that the tails separate from the
core in this regime due to entropic effects. In this case the energetic "costs" for the
formation of a bridge are lower than estimated in the model, leading to a slower decay
of the formation rate than obtained from the model.

To conclude this section, we found that the probability of bridges reflect their for-
mation rate, that in turn depends on their energetic cost. The life time of bridges is
fairly independent of the core-core separation.

What remains to be shown in the next section is that the bridges are responsible for
the attraction between multi tail complexes.

5.4 Force contribution of bridged configurations

The preceding sections dealt with tail bridging. We showed, that tail bridging occurs
and that monomers favor condensation on one of the core surfaces over staying between
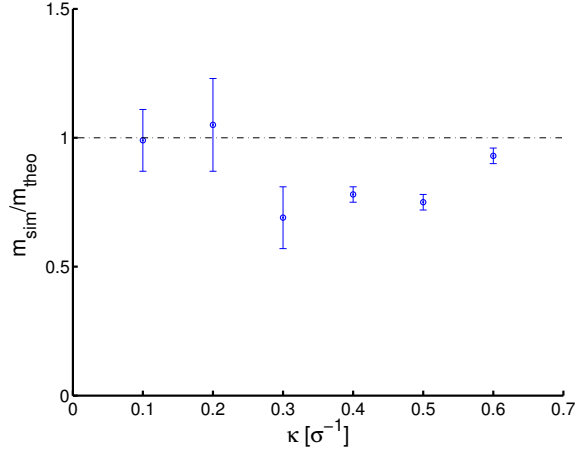
Figure 5.7: Bridge formation from simulation and from theory
Here the ratio of the exponents obtained from the simulation (m_{sim}) and from the theory (m_{theo}) are presented. For low values of κ both exponents match, indicating a good theoretical description of the system in this region. For higher salt concentrations m_{sim} exceeds m_{theo}. The reason for this behavior might be due to the separation of the tails from the core, which is observed in this region.

the complexes. In this section we will have a look at the contribution of the bridging to the interaction.

In order to achieve this, a further simulation of a pair of full chain complexes had to be performed at $\kappa = 0.4 \ \sigma^{-1}$. For the simulations presented here the MD program had to be extended, since the force data contained no bridging information up to this time. For each value of the core separation we set up 10 simulation runs over 10^6 time steps of $0.01 \ \tau$ with independent initial conditions. The mean interaction force was measured separately for configurations featuring tail bridging and for those cases without bridging by using the bridging criteria established in the previous section. Fig. 5.8 shows the results. The red line represents the case without bridging. The blue curve corresponds to the configurations with tail bridging. In the plot forces above zero correspond to repulsion, forces below zero represent attraction. The evaluation of all configurations results in the green curve. The interaction is always attractive, for large σ it approaches zero. The minimum can be found at $d = 6 \ \sigma$. Over the sampled space the blue curve, representing the non-bridging case, is well below the curve representing the overall force. We do not show data beyond $d = 13 \ \sigma$, because for larger separation tail bridging occurs too rarely to have reasonable statistics. In any case, for such large separations tail bridging is negligible which can be seen by the fact, that the blue and green curves approach close to each other. The force obtained by evaluating the configurations without tail bridging is represented by the red line. For the sampled space it is above the other curve and always in the repulsive regime. So the attraction observed for the full chain model is completely due to tail bridging
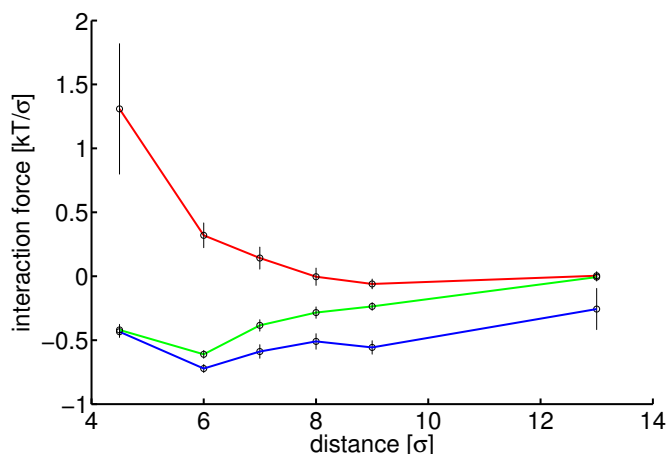
Figure 5.8: Force for bonded and non bonded configurations
This plot shows the interaction force along the separation of two complexes. The green curve represents the overall interaction force of all configurations. It has its minimum at $d = 6\ \sigma$ and is attractive over the sampled space. By accounting only for the configurations with bridging, the blue curve is obtained. For all separation distances it is well below the overall force function. The red line is obtained by only evaluating configurations were tail bridging was not observed. The curve starts at $d = 4\ \sigma$, because at smaller separations the probability of non bridged configurations is too small for any effect on the resulting force. The curve corresponding to non bridging configurations is also well above the curve obtained from all configurations. Only in the region of large d, when the effect of tail bridging becomes rare, it approaches the curve of all configurations. Since the curve from non bridged configurations is always in the repulsive regime, the attraction for the full chain model is solely due to the tail induced effects.

interaction. For large distances this curve approaches the curve of the overall force due to the lack of bridges at these parameters.

Summary

In this chapter the evaluation of the monomer distribution of two chain-sphere complexes was presented. The distribution of monomers closest to the alien core shows a minimum at a distance of $d_{\min} = 3.6\ \sigma$ from the alien core. This establishes a criteria for the formation of a bridge: Whenever a monomer comes closer to the alien core than $d_{\min}$ this configuration can be defined as a bridging configuration. Investigating the monomers of chains involved in the formation of bridges shows a bimodal distribution: These monomers prefer to condense either on the core of their own complex or on the neighbor core over residing between both complexes. The probability of finding such

a bridge was shown to decrease with increasing separation of the cores. Increasing the salt concentration leads to an increase of the frequency of bridges observed. The frequency of occurrence of bridges is linked via the mean life time to the formation rate of bridges. Here also an increase with increasing salt concentration can be observed. With increasing κ the formation rate decays exponentially. This behavior can be rationalized by taking the adsorption energy E_{Ads} of the charged monomers on the core surface into account. Comparing the simulated decay in the formation rate to the decay extracted from the theoretical model shows a small deviation for high salt concentrations. From the point of theory the decay should be faster. The reason for this behavior can possibly be explained by the chain configuration in this regime. In chapter 3 we showed that in the case of high κ the tails are already separated from the core by entropic effects. So here it is easier for the chain to find the alien core and form a bridge.

Finally the connection between the occurrence of bridging and the mutual attraction was investigated. By evaluating the interaction of the complexes separately for configurations, which show bridging, and configurations which do not, it turned out, that attraction for the full chain model is solely due to tail induced effects.

6 Influence of the tail charge on the interaction

In this chapter we study the impact of the tail charge on the interaction. As we will see in the discussion, the reduction of the charge of the tails corresponds to a chemical process, the acetylation of the histone tails, which is known to be involved in the activation of genes.

6.1 Interaction

We already studied the pair interaction of multi chain complexes via the histone tails during this work. Up to now we kept the charge fraction constant. 10 out of 28 monomers are charged, resulting in an average charge fraction of approximately 0.36. In this chapter we investigate the impact of the charge fraction f on the interaction of the complexes. We vary the fraction of charged monomers on the total number of monomers from about 0.17 to 1. This is done by changing the number of neutral monomers inserted between charged monomers as stated in Table 2. On each chain, both end monomers are always charged, the total number of monomers of a chain varies between 28 and 29. The following table shows explicitly the setups, which are investigated. In these simulations the grafted monomers are kept fixed on the surface of the sphere and κ is kept constant at 0.4 σ^{-1}.

charge fraction	charged monomers	total monomers	neutral monomers between charges
0.17	5	29	6
0.28	8	29	3
0.36	10	28	2
0.52	14	29	1
1.00	28	28	0

Table 2: Varying chain fraction

The chain fraction was varied by changing the number of charged monomers on the tails. In this table the charge fraction, the number of charged monomers, the total number of monomers and the number of neutral monomers between two consecutive charged monomers is presented for the investigated cases.

The results from the simulations with the modified chains are shown in fig. 6.1. When the charge fraction of the tails is reduced to 0.17, the minimum, which we observed in section 4.1.2 disappears completely. The interaction of the complexes is
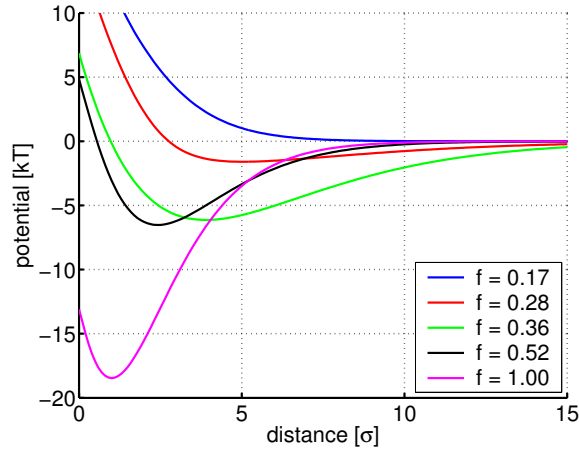
Figure 6.1: Interaction potentials for different chain charge fraction
The charge fraction of the grafted polymer chains has an impact on the mutual interaction observed. The green line represents the case of a charge fraction of 0.36 and corresponding to the values of the full chain models from the previous chapters. Here the potential has a minimum value of about -6 kT. By reducing the charge fraction of the tails to 0.28, the minimum value will increase to about -2 kT. Finally by reducing the charge fraction to 0.17, the minimum will disappear completely. Now the interaction of the complexes is repulsive for all values of the separation of the cores. By increasing the charge fraction of the tails to higher values causes a decrease of the observed minimum and a shift of the position of the minimum towards smaller core separations.

now repulsive for all values of the core separation. By fixing the charge fraction to 0.28, the minimum value of the interaction potential decreases to about $V_{\min} \approx -2$ kT. The position of the minimum can be found at a core separation of about 5 σ. The green curve corresponds to a charge fraction of 0.36 and corresponds to the potential obtained for the values used for the full chain model in the previous chapters. Here the minimum of the potential has the value $V_{\min} \approx -6$ kT. The position of the minimum is now shifted towards smaller core separations and can be found at $d \approx 4$ σ. By increasing the fraction of charged monomers to 0.52, the position of the minimum shifts to about 2 σ. The value of the minimum stays at about -6 kT. When the chains consist only out of charged monomers, what corresponds to a charge fraction of 1, the value of the minimum is dramatically reduced to about -18 kT. Also the position of the minimum shifts to a very small core separation of only 1 σ. In this case, the potential function is very similar to those found for the patch model discussed in section 4.1.5. For each curve between 13 and 24 simulations were performed at different core separations. Each simulation covered $5 \cdot 10^6$ time steps.

As we saw in section 4.1.5, in the patch model complexes optimize their electrostatic energy by putting one charge patch each into the interaction zone between the

two spheres. That results in a very strong and short ranged interaction. A typical configuration of two multi chain complexes, whose tails consists of charged monomers only (i.e. f = 1), is presented in fig. 6.2. In that case the separation of the cores is 2 σ, corresponding to the position of the observed minimum of the potential. The charge distribution here appears to be similar to that of a pair of patch complexes: An accumulation of charged monomers in the interaction zone can be observed, which is comparable to the charge patches put between the complexes in the patch model. The resulting interaction for both systems is relatively strong and short ranged. Apparently the reason for the attraction is here the interaction of the condensed charges with the charges of the central spheres, analog to the interaction observed for the patch model.
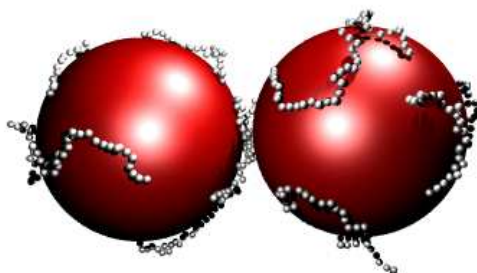
Figure 6.2: Configuration for a complex with charge fraction of the tails being 1 at a core separation of 2 σ

In this configuration the chains are almost completely condensed on the central spheres. In the interaction zone between both cores an accumulation of charged monomers can be found. Apparently the charge distribution in the interaction zone between the complexes is here similar to that observed in the patch model.

6.2 Configuration of the chains

In this section we investigate the impact of the fraction of charged monomers of a chain on its configuration. For that reason we measure the end-to-end distance and the radius of gyration. A dependence of these variable on the core separation can not be detected at the chosen value of $\kappa = 0.4 \ \sigma^{-1}$ for any of the investigated charge fractions.

Fig. 6.3 presents the end-to-end distance R_{EE} and the radius of gyration R_{G} as a function of the charge fraction of the chains. For R_{EE} we observe a monotonically increase from $R_{\mathrm{EE}} \approx 10 \ \sigma$ for a charge fraction of 0.17 to $R_{\mathrm{EE}} \approx 16 \ \sigma$ for a charge fraction of 1. For the radius of gyration the behavior is qualitatively the same: R_{G} increases monotonic with increasing values of κ. The absolute values here are lower, R_{G} ranges from about 3.5 σ for a charge fraction of 0.17 to about 6.0 σ for a charge fraction of 1. Apparently a higher charge fraction leads to swelling of the chains.

The ratio $R_{\mathrm{EE}}^2/R_{\mathrm{G}}^2$ is presented in fig. 6.4 as a function of the charge fraction. $R_{\mathrm{EE}}^2/R_{\mathrm{G}}^2$ increases slightly with increasing charge fraction from approximately 6.8 at a $f = 0.17$
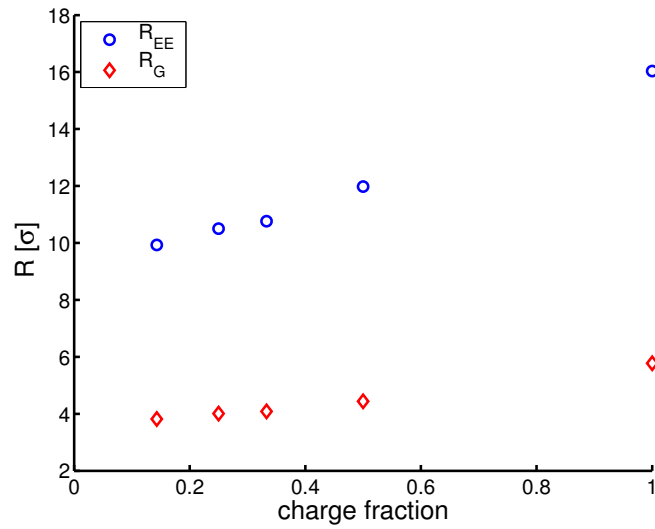
Figure 6.3: R_{EE} and R_{G} as a function of the charge fraction
The radius of gyration and the end-to-end distance are shown as a function
of the charge fraction of the grafted chains. Since the length of the chains
varies slightly, the observables are normalized by the number of monomers
per chain N. With increasing charge fraction, both the radius of gyration
and the end-to-end distance increase.
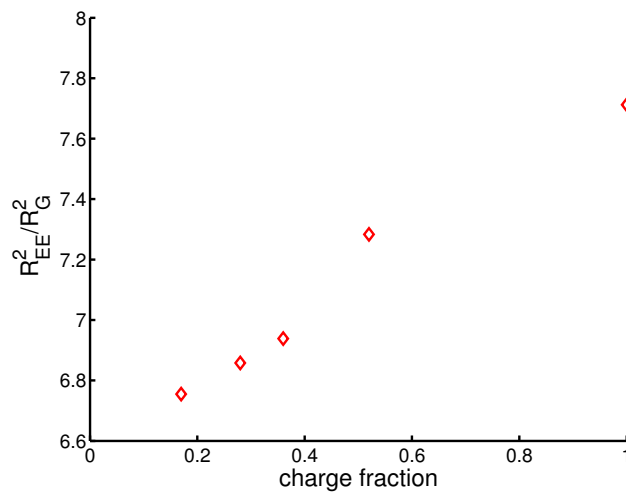
Figure 6.4: $R_{\mathrm{EE}}^2/R_{\mathrm{G}}^2$ as a function of the charge fraction
The fraction $R_{\mathrm{EE}}^2/R_{\mathrm{G}}^2$ is presented as a function of the charge fraction of
the chains. With increasing charge fraction a slight increase of $R_{\mathrm{EE}}^2/R_{\mathrm{G}}^2$
from approximately 6.7 for a charge fraction of about 0.2 to about 7.7 for
a charge fraction of 1 can be detected.

to about 7.7 at $f = 1$. Apparently the increased charge on the tails stretches the chains, what results in higher values of $R_{\mathrm{EE}}^2/R_{\mathrm{G}}^2$.

We also investigated the polarization of the monomers by computing the average deviation of the center of mass of the monomers from the center of the sphere, as we explained in section 4.1.3. However here the statistical error on the results is too large to find any significant differences for the investigated range of f, so a presentation of these results is abandoned.

Summary

This chapter is devoted to the impact of the charge fraction f on the interaction of complexes of the multi sphere model and its tail configurations. In order to change the charge of the tails, we vary the number of charged monomers per chain between 5 and 28. The number of neutral monomers between two consecutive charged monomers is varied between 0 and 6, so that the total number of monomers per chain could be kept at 28 and 29. The resulting fraction of charged monomers and total monomer varies between 0.17 and 1.

With increasing charge fraction the interaction appears to increase. For $f \geq 0.28$ we find attraction. The minimum of the attractive potential decreases with increasing chain fraction while shifting to smaller core separations. For $f = 1$ the interaction potential is very similar to that observed for the patch model. For typal configurations at that conditions, an accumulation of charged monomers in the interaction zone between the complexes can be found. Apparently the mechanism of the attraction is here similar to that found for the patch model.

The end-to-end distance as well as the radius of gyration of the single chains are both monotonic increasing with increasing fraction of charged monomers. Also the ratio $R_{\mathrm{EE}}^2/R_{\mathrm{G}}^2$ increases with increasing charge fraction. Apparently the increase of charge on the tail leads to a swelling and to the formation of more rod-like conformations of the chains.

7 Comparison to charged micelles

In the simulations presented up to now, chains were not only fixed on the surface of the sphere, but in addition the relative position of the end monomers was preserved by the 'match potentials' shown on the right side of fig. 2.4. Now we allow these monomers to float freely on the surface of the sphere. We will compare the results to the ones of the former simulations and estimate the influence of mobility of the grafting points on the interaction. We mention that such a setup could be realized experimentally by including partly charged copolymers into an oppositely charged micelle.

7.1 Interaction

We measure the interaction force of the floating chain model and compute the interaction potential in the same way as for the fixed chain model presented before. For the simulation, κ was choosen to be 0.4 σ^{-1}. The interaction force was fitted along 21 data points. The procedure to obtain the potential was analog to that described in chapter 4. We performed five runs of $2 \cdot 10^6$ time steps of 0.01 τ with different initial conditions for each data point, allowing us to average the potential over five curves. The chain length and charge fraction are the same as in the previous chapters, i.e., 28 monomers per chain and a charge fraction of 0.36. The results are presented in fig. 7.1: The middle red line indicates the pair potential of the floating chain model. The upper and lower red line indicate the errors of the mean of the curves. For small distances the potential is high due to the electrostatic interaction. With increasing distance the potential decays until it reaches its minimum of about -5 kT at a distance of about 4 σ. The blue lines show the pair potential with the error of the fixed chain model for comparison. Here the minimum is slightly deeper than in the case of the floating chain model, but also located at a distance of about 5 σ. Thus remarkably the grafting condition (floating vs. fixed) has here only a minor impact on the pair potential.

7.2 Bridging

Also for the floating chain model we find bridging between the complexes, just like in the case of the fixed chain model. This section is devoted to the investigation of the bridging between floating chain complexes. Furthermore, we compare the results obtained from both models.

Fig. 7.2 shows the frequency of bridges. The red symbols correspond to the floating chain model, while the blue symbols represent the fixed chain model. In both cases the occurrence of bridges decays exponentially with increasing distance of the cores.
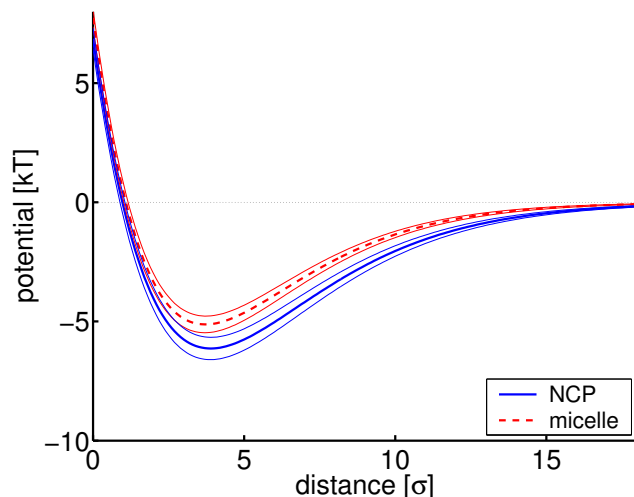
Figure 7.1: Pair interaction potential of the floating chain model
The red lines show the pair interaction potential of the floating chain model
with the corresponding errors. The minimum of about $-5\ \sigma$ is located at
approximately $4\ \sigma$. The blue lines indicate the pair interaction potential
of the fixed chain model with errors. Here the minimum is approximately
at the same position but slightly deeper.
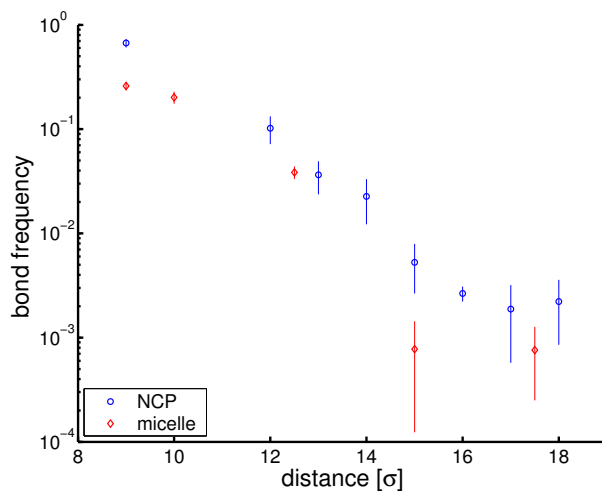
Figure 7.2: Frequency of bridges
The frequency of bridges between the complexes is presented for the float-
ing chain model and the fixed chain model by red and blue symbols respec-
tively. In both cases the occurrence of bridges decays exponentially with
increasing distance. The number of observed bridges is slightly smaller in
the case of the floating chain model for all core-core separations.
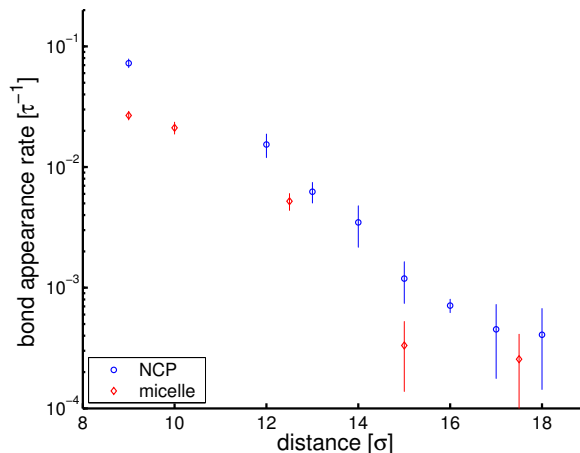
Figure 7.3: Formation rate for new bridges
The floating chain model is represented by red symbols while the results for the fixed chain model are given by the blue symbols for comparison. In both cases the appearance rate decreases exponentially with the distance. For the floating chain model the appearance of new bridges is slightly below those of the fixed chain model.

Apparently for the floating chain model the number of bridges is slightly smaller than in the case of the fixed chain model for all separations between the cores.

The formation rate of new bridges is presented in fig. 7.3 as a function of the core separation. The floating chain model is represented by the red symbols. The blue symbols give the results from the fixed chain model for comparison. In both cases the appearance of new bonds decreases exponentially with the core separation. As in the case of the frequency of occurrence discussed above, the appearance rate for new bridges for the floating chain model is slightly lower than for the fixed chain model.

Fig. 7.4 presents the mean life time of bridges for the floating chain model. Again the results for the fixed chain model are given for comparison, as indicated in the legend. In both cases the life time decreases with increasing core separation. For core separations lower than 12 σ the life time for bridges in the floating chain model appears to be slightly higher than the life time of those in the fixed chain model. For larger core separations no difference can be detected.

Up to here there seem to be only minor difference between the setups. We will now present a quantity that shows a drastic difference for the cases: The time correlation function

$$C(T) = \langle P_B{}^i(t) \cdot P_B{}^i(t+T) \rangle / \langle P_B{}^i \rangle^2 \tag{7.1}$$

of a bridge formed by a *given* tail. $P_B{}^i(t)$ denotes the probability, to find the ith tail of a complex to form a bridge at the time t. $P_B{}^i(t)$ is the ovrall probability to find the tail i to form a bridge. We present this function in fig. 7.5 for the floating and the fixed chain model. The correlation of the floating chain model decays much faster than in the case of the fixed chain model. For the floating chain model the correlation
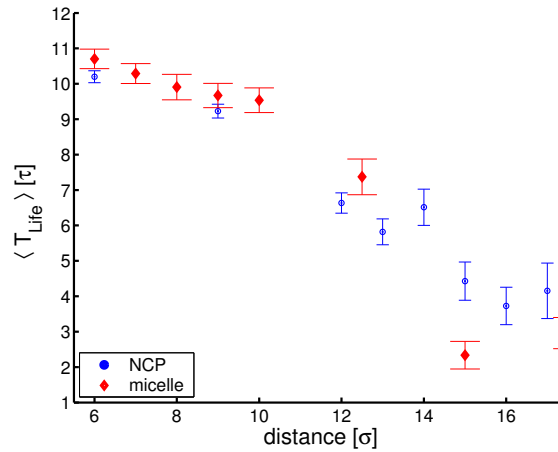
Figure 7.4: Life time of bridges

Here the life time of the bridges is presented as a function of the core separations. The results from the floating chain model are represented by the red symbols, those from the fixed chain model are given by the blue symbols for comparison. In both cases the mean life time decreases with increasing core separation. For core separations smaller than 12 σ the life time of the bridges appears to be smaller for the floating chain model than in the case of the fixed chain model.
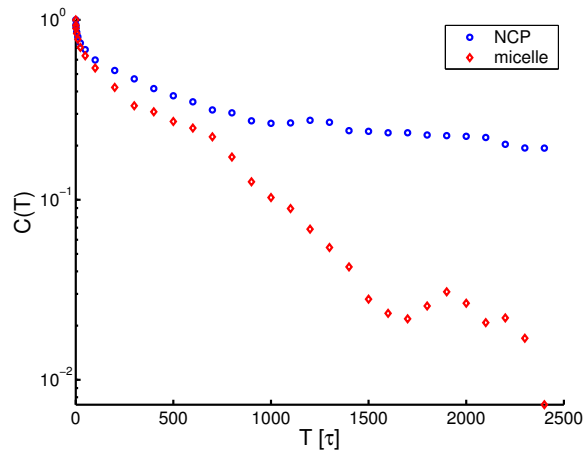
Figure 7.5: Correlation of bridge appearance

The time correlation function of the appearance of bridges is shown for the fixed and the floating chain model as a function of the LJ time τ for the core-core distance 9 σ at $\kappa = 0.4 \ \sigma^{-1}$. The correlations of the fixed chain system appear to be considerably larger than in the case of the floating chain model.

function approaches zero at about 1500 τ, while for the fixed chain model correlations are still present at periods up to 2500 τ.

In case of the floating chain model, the single chains can move independently from each other on the surface of their sphere. For the fixed chain model, this is not true anymore. Here the grafted monomers form a cube on the surface of the sphere. Therefore at least six of the grafted monomers with the eight chains attached to them have to move together. For this reason the positions of the grafted ions are much less mobile in the fixed chain model. When a bridging tail separates from the neighboring core, in the case of the fixed tail model the tail monomers might on average stay longer in the interaction zone of the neighboring core than in case of the floating tail model due to that lower mobility. This increase in the time of residence might in turn be responsible for the correlations in the bridge formation observed as well as for the slightly increased bridge frequency and consequently for the slight difference in the pair potentials.

7.3 Polarization of the grafting points

In the previous section we saw that the pair interaction and the bridging is very similar in the case of the floating chain model and that of the fixed chain model. Only the comparison of the correlations of bridges of a given tail revealed a dramatic difference. Here we present another observable, which differs for both models: The polarization of the grafting points.

In order to obtain this quantity, we determine the unit vector pointing from the center of one sphere to a grafting point on its surface. From this vector we take the projection on the connecting line between both complexes. If the projection lies between the complexes, the contribution is counted positive, otherwise negative. Now the polarization can be obtained by averaging over all grafting points on both complexes. The result is shown in fig. 7.6 as a function of the core-core separation for $\kappa = 0.4\ \sigma^{-1}$. For low separations the polarization is around 0.25. By increasing the separation, this value remains constant until the core-core separation reaches about 7 σ. For higher separations the polarization decreases slightly, to about 0.15 at a separation of 15 σ. By investigating the polarization of a pair of complexes of the fixed chain model with the same κ, the polarization turns out to be of the order of 10^{-4} with a statistical error of about 10^{-3} for the whole range of the core-core separation. In principle, this value should be exactly zero but the large, yet finite, spring constants of the "match potentials" allow small fluctuations.

Polarization can also be observed for the monomer cloud of the whole complexes. Fig. 7.7 presents the deviation of the CM of the monomers from the center of the sphere as a function of the core separation analogous to the study presented in section 4.1.3. For low core separations the polarization of the monomers is maximal. Here the deviation of the CM adds up to about 1.5 σ. It should be noted, that for the fixed chain model we also observe a polarization at this value of κ, but there its value is smaller by a factor of three. As in the case of the fixed chain model a linear decay with increasing distance until $d \approx 15\ \sigma$ can be detected.
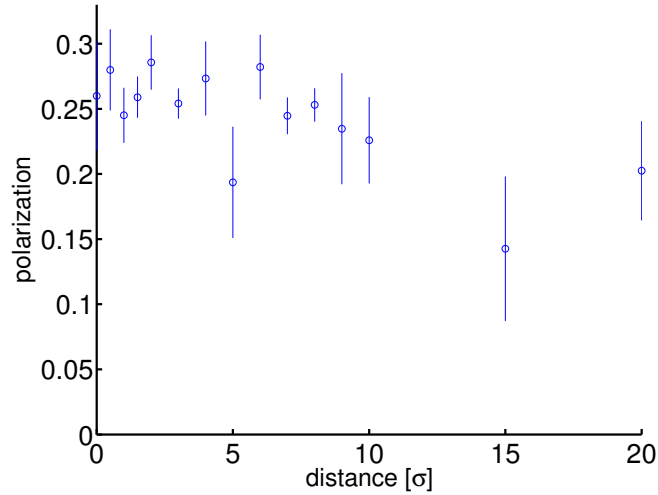
Figure 7.6: Polarization for the floating tail model

For low core-core separations the polarization is constant at about 0.25 until $d \approx 7\ \sigma$. By increasing the distance beyond this value, a slight decrease in the polarization to about 0.15 at a distance of 15 σ can be detected. For the fixed chain model the polarization turns out to be of the order of 10^{-4} with an statistical error of about 10^{-3} for the whole range of d.
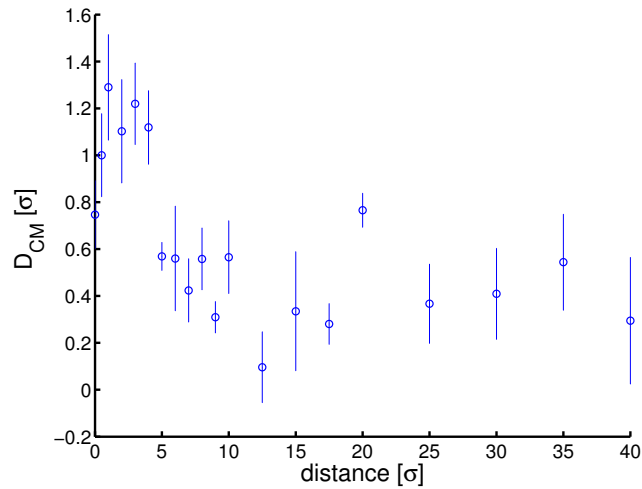
Figure 7.7: CM position of the monomer cloud of one complex

The maximum deviation of the CM of the monomer clout from the center of the sphere can be found at low core separations. With increasing core separation, the deviation decreases until the distance between the complexes reaches a value about 15 σ. The observed effect is about three times as distinct as in the case of the fixed chain model.
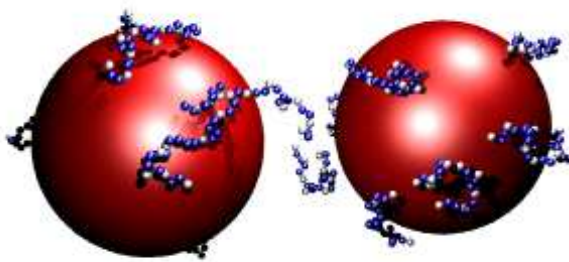
Figure 7.8: A configuration of the floating chain model at $d = 9 \, \sigma$

Fig. 7.8 shows a typical configuration of the floating chain model at a core-core separation of 9 σ at $\kappa = 0.4 \, \sigma^{-1}$. Since the relative positions of the grafting points are not fixed anymore, the chains can move freely on the surface of the sphere. Apparently the chains are distributed over the entire surface of both cores, indicating that the interaction with the neighbor complex is not dominating here.

7.4 Configuration of the tails

This section is devoted to the configuration of the chains grafted on the surface of the sphere. We compare the findings for the floating chain model to the results obtained for the fixed chain model, which we already presented in section 4.1.6. Analogous to the study regarding the fixed chain model, we investigated the tails facing towards the neighbor complex, i.e., those chains whose grafting points lie between the two sphere centers.

Fig. 7.9 presents the end-to-end distance R_{EE} of the single chains as a function of the core separation. R_{EE} appears to be slightly larger for the floating chain model than for the fixed chain model for the entire range of the core separation. While for the fixed chain model R_{EE} is constant for the entire range of d, the floating chain model shows a slight variation. Here R_{EE} is for low values of d approximately 11.3 σ. With increasing d R_{EE} decreases, until it reaches about 11.0 σ at a core separation of about 5 σ.

For the radius of gyration R_{G} as a function of the core separation d, which is presented in fig. 7.10, we find qualitatively a very similar behavior. For the fixed chain model R_{G} is constant at approximately 4.1 σ. In case of the floating chain model, R_{G} is about 4.22 σ for very low core separations. With increasing d the radius of gyration decreases until it reaches a value of about 4.15 σ at a core separation of about 5 σ. As the end-to-end distance, the radius of gyration for the floating chain model is larger than that for the fixed chain model over the entire range of d.

The ratio $R_{\mathrm{EE}}^2 / R_{\mathrm{G}}^2$ is presented as a function of the core separation in fig. 7.11. The blue circles correspond to the floating chain model, while the red squares represent the results obtained from the fixed chain model. For the entire range of the core separation, the ratio obtained from the floating chain model is above that from the fixed chain
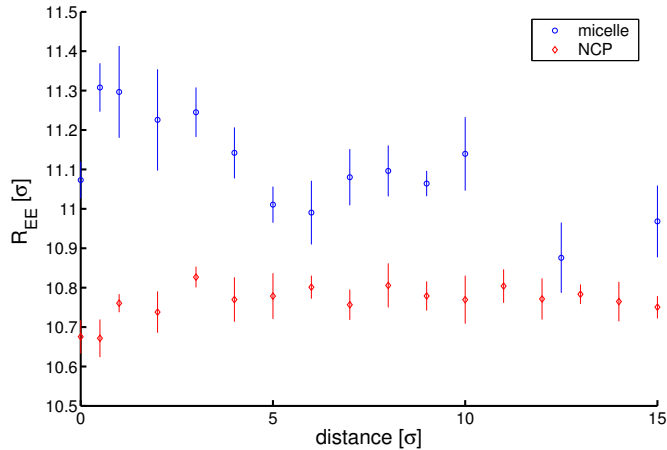
Figure 7.9: Comparison of R_{EE}
The end-to-end distance is shown as a function of the core separation for the floating and the fixed chain model. For the case of floating chains R_{EE} appears to be larger than for the case of the chains being fixed. While for the fixed chain model the end-to-end distance is constant for the entire range of the core separation, for the floating chain model R_{EE} is clearly higher for low separations than for high values of d.

model, indicating that the chains facing the neighbor complex prefer configurations which are more stretched with respect to those of the fixed chain model. This behavior is remarkable, since we observe a higher frequency of bridges in the case of the grafting points being fixed on the surface of the sphere than in the case of floating end monomers. Furthermore we find for both cases a slight decrease in $R_{\mathrm{EE}}^2/R_{\mathrm{G}}^2$ with increasing core separation. This behavior indicates a decreasing influence of the interaction of the chains with the neighbor complex with increasing core separation.

Summary

In this chapter we investigated a variation of the full chain model. In order to estimate the importance of the grafting positions on the interactions of the complexes, we allowed the chains to move freely on the surface of the core. For this floating chain model we measured the effective potential in the same way as described in chapter 4. We found that the pair potential measured for the floating chain model is slightly higher than in the case of the potential between two fixed chain complexes.

The frequency of bridges as well as the appearance rate of new bridges are slightly lower for the floating chain model than in the case of the fixed chain model. For small core separations the mean life time of bridges is higher in the case of the floating chain model than in the case of the fixed chain model, but also here there is only a minor difference between the setups.
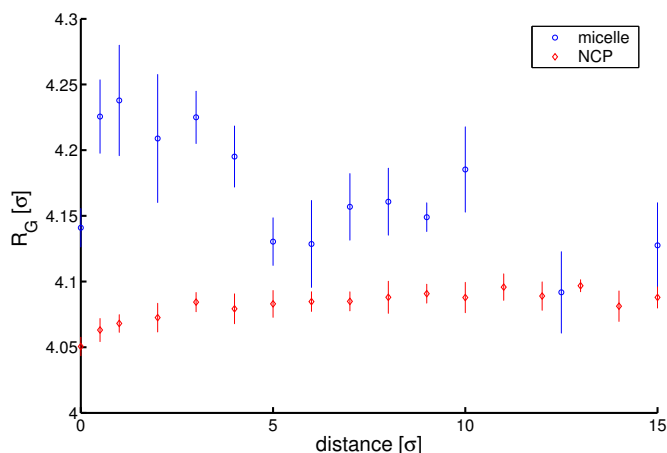
Figure 7.10: Comparison of R_G

The radius of gyration is presented as a function of the core separation for the floating and the fixed chain model. Just like in the case of the end-to-end distance, the radius of gyration appears to be larger in the case of the floating chain model than for the fixed chain model. While for the fixed chain model R_G does not vary with increasing core separation, for the floating chain model R_G is clearly larger for core separation smaller than about 5 σ than for larger ones.

The time correlation function of the occurrence of bridges was computed for both models. For the floating chain model the correlation function decays after about 1500 τ, in case of the fixed chain model correlations can be detected for time intervals $\geq 2500 \tau$. This dramatic difference might explain the weaker attraction observed in case of the floating chain model.

Another observable showing a considerable difference for both setups is the polarization of the grafting points of the complexes. In case of the floating chain model, the polarization is constant at about 0.25 for core-core separations smaller than about 7 σ. For higher values of the separation, a slight decrease of the polarization to about 0.15 at a distance of 15 σ can be observed. For the fixed chain model, the polarization is of the order of 10^{-4} with an statistical error of the order of 10^{-3}.
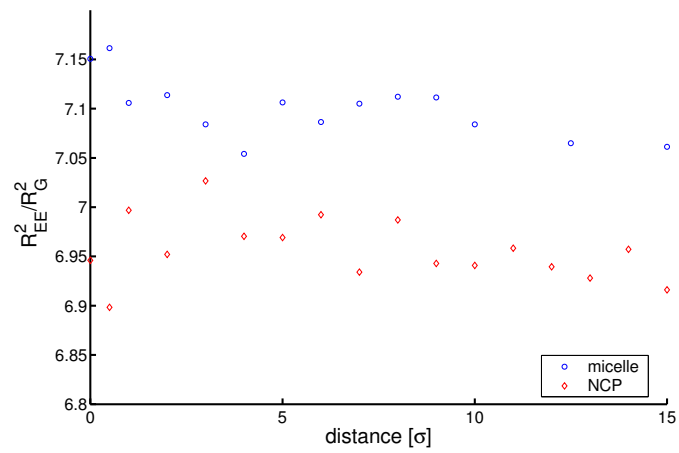
Figure 7.11: Comparison of R_{EE}^2/R_G^2

The ratio R_{EE}^2/R_G^2 is shown for the floating and the fixed chain model as a function of the core separation. For the floating chain model R_{EE}^2/R_G^2 appears to be larger than for the fixed chain model for the entire range of d. For both models R_{EE}^2/R_G^2 decreases slightly with increasing core separation. For the fixed and the floating chain model the errors are about 0.07 and 0.1 respectively. They are not shown here in order to increase the clarity of the plot.

Discussion

In this work we investigated the pair interaction of the multi sphere complex, which can possibly serve as a model system of the NCP. We found long ranged attraction between the complexes, which is due to the bridging of the tails, which are grafted on the surface of the core. This attraction can be regulated by changing the charge fraction of the chains. As we will see in this section, this possibility of tuning the interaction has extensive implications on the management of the genetic information of eukaryotes.

In the living cell the chromatin fiber is extremely heterogeneous [90], which can be due to various effects [18, 91–97]. A region of the fiber can either be condensed or decondensed. In the case of a condensed region, the information stored on the corresponding part of the DNA is not accessible, the chromatin is 'inactive'. When the fiber is decondensed, the information can be read out and the chromatin is 'active'. Condensation of the chromatin fiber, and therefore transcriptional control of the information stored on the DNA, is partly linked to the acetylation of the histone proteins [98, 99]. The histone tails contain the amino acid lysine, which is the target for this reaction. This amino group can be acetylated by an enzyme in the cell, the histone acetyletransferase (HAT). This reaction is reversible by an enzymatic activity in the cell called histone deacetylase (HDA). The process of acetylation is depicted in fig. 7.12: In the presence of the enzyme HAT one molecule of Acetyl-Coenzyme A can react with the lysine side chain. Now the Acetyl group gets attached to the lysine, forming an acetate. The charge and the Coenzyme A (HSCoA) are released into the solvent. In the presence of HDA this reaction can be reversed. During the acetylation, the lysine side chain becomes neutral by loosing one proton. Consequently, the positive charge of the histone tail is reduced.

In regions of active chromatin, the histones show high levels of acetylation, which corresponds to a low charge content of the histone tails [16]. Fig I.2 in the introduction shows several cases of active and inactive chromatin: In the case of the orange fiber the chromatin is condensed and therefore inactive. This state corresponds to a low level of acetylation. The case of high levels of acetylation is represented by the yellow nucleosomes in the figure. The shown region of the fiber is decondensed and active.

A recent Monte Carlo study [3] demonstrated a connection between the mutual attraction of nucleosomes and the condensation of the fiber. Simulations of the nucleosome fiber without mutual attraction of the nucleosome cores resulted in a decondensed fiber. However, by using a sufficiently attractive interaction potential of the Gay-Berne form, the fiber condensed into a hairpin, which is a very dense configuration of the chromatin fiber.
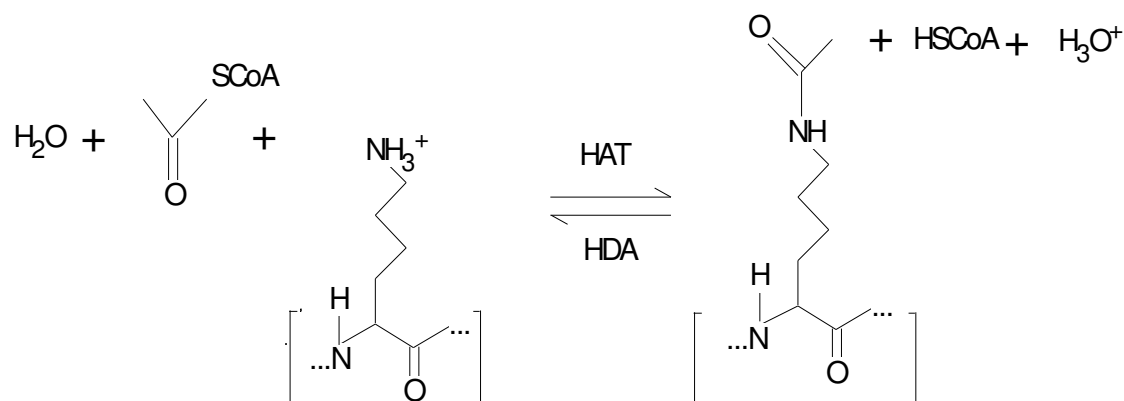
Figure 7.12: Acetylation of lysine

In the presence of the enzyme HAT one molecule of Acetyl-Coenzyme A
can react with the lysine side group. Now the Acetyl group gets attached to
the lysine, forming an acetate. The charge and the Coenzyme A (HSCoA)
are released into the solvent. In the presence of HDA this reaction can
be reversed. During the acetylation, the lysine side becomes neutral by
protonation of the solvent

Configurations like the ones presented in reference [3] can also be observed in experiments. Fig. I.3, which was already presented in the introduction, shows an image of highly compacted chromatin fibers forming a hairpin obtained with cryoelectron microscopy.

By reducing the charge fraction in our model, we observe decreasing and vanishing mutual interaction of the nucleosome cores. In the case of vanishing attraction, however, reference [3] also states decondensation of the fiber. So in this case, our simulations agree with the experimental outcome.

Apparently, one possibility to regulate the activity of genes could be to control the formation of highly dense chromatin. This could possibly be done by controlling the level of acetylation of the histone tails. According to our findings, the level of acetylation of the histone tails might be responsible for the interaction between the NCPs. Taking into account, that an attractive interaction between NCPs could lead to the formation of e.g. a hairpin, the tail mediated interaction of NCPs could indeed be an important ingredient of the management of the genetic information.

Conclusions

In this work the electrostatic contribution to the interaction of nucleosome core particles (NCPs) was studied. Here the histone tails were in the center of interest, since recent experiments suggest an involvement between the tails and the NCP-NCP interaction [1,2].

The models applied in theory and simulation, which were available up to now, neglected the tails. This led us to introduce the model of the multi chain complex. The histone core and the DNA wrapped around were modelled as a sphere carrying a central charge. The histone tails were represented by flexible polyelectrolyte chains. Each chain has one end monomer grafted on the surface of the sphere. The grafted monomers form the corners of a cube, their relative positions to each other are fixed.

By using MD simulations, the pair interaction of two multi chain complexes was investigated. This included the evaluation of the mutual force, the effective potential and the second virial coefficient. The interaction turned out to be attractive for an appropriate range of parameters with regard to the solution conditions and particle separation.

As effects capable to theoretically explain such an attraction, correlations of charge patches and tail bridging have been proposed in the recent literature. We set up different models in order to isolate both effects. The interaction due to charge patches could be ruled out due to the shorter range as compared with the interaction of the multi chain model.

It was possible to prove the existence of tail bridging for the multi chain model by the investigating the distribution of the monomers. The formation rate of new bridges could be linked to the desorption energy of the tail bridging charged monomers. By discriminating between configurations that form bridges between the core particles, and those which did not, the attraction was shown to be solely due to the tail bridging.

The influence of the relative position of the tails was studied by allowing the tails to move freely on the sphere surface. We also studied the impact of the charge fraction on the interaction by varying the number of charged monomers on the tails.

Finally, we speculated about the role of tail bridging in the transcriptional control in chromatin. The process of acetylation of the histone tails (a process known to be linked to the formation of active chromatin) is equivalent to the reduction of the charge of the grafted tails. Subsequently, the attraction between the particles decreases and even vanishes with decreasing charge fraction of the tails. Together with recent MC simulations [3], these results suggest that the influence of bridging of the histone tails plays an important role in the compacting process of the chromatin fiber, and also could be responsible for the silencing of genes.

A The second virial coefficient

In the course of this thesis the second virial coefficient A_2 was used in order to describe the pair interaction of particles. Here we discuss the different ways to obtain A_2 either from an experiment dealing with a dilute solution of NCPs or from a computer simulation.

A.1 Experimental investigation of A_2

In section 1.3 the second virial coefficient was determined via an experiment dealing with a dilute solution of NCPs. Here we want to outline the procedure of obtaining A_2 used in reference [2]. These authors show also within this approach, that interactions involving three or more particles at the same time can indeed be neglected.

A definition of the osmotic coefficients was already given in equation 1.1 in section 1.3. By dividing both sides of this equation by the concentration of NCP, C_{NCP}, one gets

$$\frac{\Pi}{RTC_{\mathrm{NCP}}} = \frac{1}{M} + A_2 C_{\mathrm{NCP}} + A_3 C_{\mathrm{NCP}}^2 + \ldots \quad . \tag{A.1}$$

As in equation 1.1 the A_i represent the virial coefficients. As mentioned before, each A_i accounts for the contribution to the osmotic pressure Π of interactions involving i particles. In the case of negligible contributions of $A_3, A_4, A_5 \ldots$ one would expect a linear dependency of $\Pi/(RTC_{\mathrm{NCP}})$ and C_{NCP}.

Fig. A.1 shows $\Pi/(RTC_{\mathrm{NCP}})$ as a function of the concentration of NCPs as measured in reference [2]. Different symbols feature different salt concentrations. Obviously the linear dependence, which is necessary to safely neglect many body interactions, is fulfilled. This result verifies the assumption that higher order coefficients can be neglected. From top to bottom the relevant salt concentrations are 3.5 mM, 25 mM, 75 mM and 210 mM. The extrapolations of the obtained lines give the molecular weight of the nucleosome core particle within the error of determination. A_2 can now be obtained for any salt concentration by fitting a straight line through the relevant data and determining its slope.

A.2 Computer simulation to determine A_2

The method of obtaining A_2 experimentally for a dilute solution of nucleosome core particles was mentioned in the previous section. In the case of a computer simulation, A_2 can be obtained by using the measured potential of mean force. This was done in section 4.1.4 by using equation 4.3. This equation can be obtained from an expansion

A The second virial coefficient
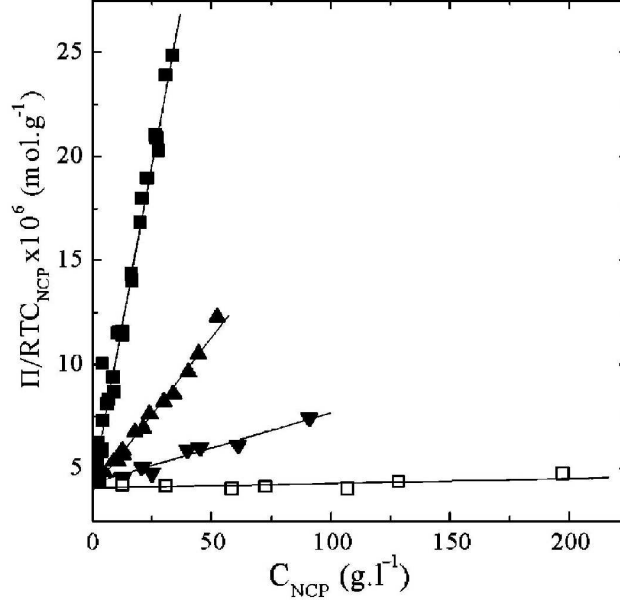
Figure A.1: Osmotic pressure divided by the concentration of NCPs
and by RT for different salt concentrations
The salt concentration varies for the different curves and determines the
determines the slope of the curves. From the top to the bottom the salt
concentrations are 3.5 mM, 25 mM, 75 mM and 210 mM. The different
gradients of the lines represent different A_2 for the different salt concentrations. (Taken from [2])

of the free energy of a dilute system of particles [5, 79, 80]:

$$F = -kT \ln \int e^{-\frac{E(\vec{p}, \vec{r})}{kT}} d\Omega \quad . \tag{A.2}$$

Here E represents the energy depending on the positions $\vec{r}$ and momenta $\vec{p}$ of the
particles. $d\Omega$ represents a volume element of the phase space $d\vec{p} \, d\vec{r}$. Considering the
NCPs as classical particles with the total energy

$$E(\vec{p}, \vec{r}) = \sum_{i=1}^{N} \frac{\vec{p}_i^{\,2}}{2m} + V(\vec{r}_i) \tag{A.3}$$

equation A.2 can be written as

$$F = F_{\mathrm{id}} - kT \ln \frac{1}{v^N} \int \cdots \int e^{-\frac{V}{kT}} dv_1 \ldots dv_N \tag{A.4}$$

$$= F_{\mathrm{id}} - kT \ln\{\frac{1}{v^N} \int \cdots \int (e^{-\frac{V}{kT}} - 1) dv_1 \ldots dv_N + 1\} \tag{A.5}$$

with v being the volume of the system. Using $\ln(1+x) \approx x$ we obtain

$$F \approx F_{\mathrm{id}} - kT \frac{1}{v^N} \int \cdots \int (e^{-\frac{V}{kT}} - 1) dv_1 \ldots dv_N \tag{A.6}$$

with N being the number of NCPs in the system. F_{id} is the free energy of an ideal gas. $V(\vec{r}_i)$ is the potential energy of particle i located at $\vec{r}_i$. dv describes a volume element. Since we consider only pairwise interaction of nucleosomes, we can write the integral as

$$\frac{N(N-1)}{2} \int \cdots \int (e^{-\frac{V_{12}}{kT}} - 1) dv_1 \ldots dv_N \tag{A.7}$$

with V_{12} being the interaction potential of two nucleosomes. Since it only depends on the relative coordinates of the two particles involved in the interaction, the integration over the others can be carried out as well as the integration over the center of mass of the remaining pair. The integral over the particles gives a factor of $v^{(N-2)}$, integrating over the center of mass gives another v. N is large, so we can write $N(N-1) \approx N^2$ and get

$$F = F_{\text{id}} - \frac{kTN^2}{2v} \int (e^{\frac{-V_{12}}{kT}} - 1) dv. \tag{A.8}$$

So with $p = -\frac{\partial F}{\partial v}$ we obtain the pressure

$$p = \frac{NT}{v} + \frac{N^2 kT}{v^2} \int (1 - e^{\frac{-V_{12}}{kT}}) 4\pi dr. \tag{A.9}$$

Now by comparing equation A.9 to the two leading terms of equation 1.1 we get the result

$$A_2 = \frac{1}{2} \int_0^\infty (1 - \exp(-V(r)/kT)\, 4\pi r^2\, dr. \tag{A.10}$$

Since in our model the core can be described as a hard sphere potential with radius a, A.10 can be written as

$$A_2 = 2\pi \int_0^{2a} r^2 dr + 2\pi \int_{2a}^\infty (1 - \exp(-V(r)/kT) r^2 dr \tag{A.11}$$

$$= 4v_0 + 2\pi \int_{2a}^\infty (1 - \exp(-V(r)/kT) r^2 dr \quad . \tag{A.12}$$

This is the final result for a system of hard spheres with radius a and the volume v_0. It is applicable for the models presented in this study, since the structures can be seen as hard spheres with an additional Lennard Jones potential for larger distances than a, which is included in the effective interaction potential $V(r)$.

A The second virial coefficient

B The Debye-Hückel Theory

The electrostatic interactions in this thesis are treated on the Debye-Hückel level [100]. Our system consists of two basic charged particles: The nucleosome cores which are represented as spheres with radius a and the monomers, which are represented as point like charges with respect to the electrostatics as is the salt, which is responsible for the screening. The standard Debye-Hückel theory includes the interactions of ions with finite radii, however it does not include interactions of colloidal particles in an environment which is screened by ions with much smaller extension. This case, however, is given in our setup: We encounter mutual interaction of the spherical histone cores, interaction between a core and charged monomers and the interactions amongst the point like charged monomers. In reference [101] the solution of this problem is given as an approximation valid for large separations of the interacting particles, however a more direct approach to the interaction can be given by the equilibrium theory [102]. Here we want to provide a short outline of this approach and present the interactions applied in the simulations as a result.

B.1 Model

The model used for this derivation is an ionic solution of volume v and will be represented by the primitive model. The salt ions are modelled as N hard spheres, half of them bear a positive charge $q_1 = z$, the rest bears a charge q_2 of same magnitude and opposite sign. The definition of the unit charge as the elementary charge, as well as the other definitions are as in section 2.1.3. The diameters of the salt ions are equal: $d_1 = d_2 = d$. The macroions are represented by spheres with diameter $d_3 = D$ and a central charge of $q_3 = Q = Z$. The concentration $\rho_3 = N_3/v$ is assumed to be negligible to the concentrations of the salt ions $\rho_1 = \rho_2 = N/(2V)$. The fourth species of counterions, which outweighs the positive charge of the colloids, has the same properties as the corresponding salt ions. However their concentration $\rho_4 = Z\rho_3$ can be neglected as in the case of the colloids. The resulting interaction potential $v_{ij}(r)$ (in units of kT) of two particles of the species i and j is then given by

$$v_{ij}(r) = u_{ij}^0(r) + u_{ij}(r) \tag{B.1}$$

with

$$u_{ij}^0(r) = \begin{cases} \infty & \text{for } r \leq d_{ij} \\ 0 & \text{else.} \end{cases} \tag{B.2}$$

d_{ij} is half of the center-center separation of the involved particles:

$$d_{ij} = \frac{d_i + d_j}{2} \tag{B.3}$$

according to the defined values, $d_1 = d_2 = d$ and $d_3 = D$. The remaining potential is the Coulomb potential

$$u_{ij}(r) = l_B \frac{q_i q_j}{r}. \tag{B.4}$$

To simplify this expression, we will set $l_B = 1$ for the further course. The determination of the radial distribution function $g_{ij}(r)$ is equivalent to finding the potential of mean force V_{ij}, since

$$g_{ij}(r) = \exp(-V_{ij}(r)/kT). \tag{B.5}$$

However, it will be more convenient to use the correlation function

$$h_{ij}(r) = g_{ij}(r) - 1 \tag{B.6}$$

and

$$w_{ij}(r) = V_{ij}(r) - u_{ij}^0(r) \tag{B.7}$$

which is identical to the potential of mean force for $r > d_{ij}$. Equation B.5 can now be written as

$$g_{ij}(r) = \exp(-u_{ij}^0(r)/kT)\exp(-w_{ij}(r)/kT). \tag{B.8}$$

The Ornstein-Zernike integral equation

$$h_{ij}(r) = c_{ij}(r) + \sum_{k=1}^{3} \rho_k \int h_{ik}(|r - r'|)c_{kj}(r')\,dr' \tag{B.9}$$

can be used for $1 \leq i, j \leq 3$ [80]. Equation B.9 can be seen as the definition of the direct correlation function $c_{ij}(r)$. In order to transform equation B.9 into a closed equation, another relation between h_{ij} and c_{ij} is necessary. Two well known examples of closure relations are the hypernetted chain approximation

$$c_{ij}(r) = -u_{ij}(r)/kT + h_{ij}(r) - \ln(\exp(u_{ij}^0/kT)(1 + h_{ij}(r))) \tag{B.10}$$

and the mean spherical approximation

$$c_{ij} = -u_{ij}(r)/kT \qquad\qquad \text{for } r > d_{ij} \tag{B.11}$$

$$h_{ij} = -1 \qquad\qquad \text{for } r < d_{ij}. \tag{B.12}$$

The Ornstein-Zernicke equation can now be solved with one of these or another suitable closure. However, the mathematical problem simplifies considerably by using the limit $\rho_3 \to 0$ in which we are interested, as mentioned above. In this case equation B.9 becomes

$$h_{ij} = c_{ij} + \sum_{k=1}^{2} \rho_k \int h_{ik}(|r - r'|)c_{kj}(r')\,dr' \qquad\qquad \text{for } 1 \leq i, j \leq 2, \tag{B.13}$$

$$h_{3i} = c_{3i} + \sum_{k=1}^{2} \rho_k \int h_{3k}(|r - r'|)c_{ki}(r')\,dr' \qquad\qquad \text{for } 1 \leq i \leq 2, \tag{B.14}$$

$$h_{33} = c_{33} + \sum_{k=1}^{2} \rho_k \int h_{3k}(|r - r'|)c_{k3}(r')\,dr' \quad . \tag{B.15}$$

Since we now have a simpler version of the Ornstein-Zernike equation and also have suitable closures, we can actually start to compute the desired interactions.

B.2 Interaction of point like particles

In the case of interaction between point like salt ions, i.e. $d_1 = d_2 \to 0$, the closure relation of equation B.13 is given by

$$h_{ij}(r) = -\frac{q_i\, q_j}{kT}\frac{1}{r} \qquad\qquad \text{for } 1 \le i, j \le 2. \qquad\qquad (\text{B.16})$$

By inserting this into the Ornstein-Zernicke equation, one gets the Debye-Hückel correlation functions

$$h_{ij} = -\frac{q_i q_j}{kT}\frac{e^{-\kappa r}}{r} \qquad\qquad\qquad\qquad (\text{B.17})$$

with

$$\kappa^2 \equiv \frac{1}{\epsilon kT}\sum_{i=1}^{2}\rho_i q_i^2 \quad . \qquad\qquad\qquad\qquad (\text{B.18})$$

Since the Debye-Hückel theory assumes the linearization of equation B.5, one gets

$$g_{ij}(r) \equiv 1 + h_{ij}(r) = e^{\frac{-V_{ij}(r)}{kT}} \approx 1 - \frac{V_{ij}(r)}{kT} \quad . \qquad\qquad (\text{B.19})$$

Comparison with equation B.16 yields the Debye-Hückel potential for point like particles

$$V_{ij}(r) = q_i\, q_j\frac{e^{-\kappa r}}{r} \qquad\qquad \text{for } 1 \le i, j \le 2 \quad . \qquad\qquad (\text{B.20})$$

Inserting the unity monomer charge and putting back l_B, we get equation 2.16, which describes the interaction between two monomers:

$$V_{\mathrm{mm}}(r) = l_B\frac{e^{-\kappa r}}{r} \quad . \qquad\qquad\qquad\qquad (\text{B.21})$$

B.3 Interaction of ions with colloidal particles

In the case of interaction between a core particle of diameter D and a point like ion, or $d_1 = d_2 = 0, d_3 = D$, equation B.14 has to be used. By applying the closure relation B.16 for the point like ions, one obtains

$$h_{3j} = c_{3j} - \sum_{k=1}^{2}\int h_{3k}(|r - r'|)\frac{q_k\, q_j}{kT}\frac{1}{r'}\, dr' \quad . \qquad\qquad (\text{B.22})$$

The appropriate closure relations for the core ion interaction are

$$c_{3j}(r) = -Q\, q_j\frac{1}{r} \qquad\qquad\qquad \text{for } r > D/2 \qquad\qquad (\text{B.23})$$

$$h_{3j}(r) = -1 \qquad\qquad\qquad\qquad\quad \text{for } r < D/2 \quad . \qquad\qquad (\text{B.24})$$

Now it is possible to solve equation B.22 for $c_{ij}(r)$ for $r < D/2$ and $h_{ij}(r)$ for $r > D/2$ respectively. After some analysis one obtains

$$h_{3j}(r) = -\frac{1}{kT}\frac{Q\,q_j}{(1+\kappa D/2)}\frac{e^{-\kappa(r-D/2)}}{r} \qquad \text{for } r > D/2 \qquad (\text{B.25})$$

$$c_{3j}(r) = -(1 + \frac{Q\,q_i}{kT}\frac{\kappa}{(1+\kappa D/2)}) \qquad \text{for } r < D/2 \qquad (\text{B.26})$$

Due to the Debye-Hückel approximation one finds

$$h_{ij}(r) = g_{ij}(r) - 1 \approx -\frac{V_{ij}(r)}{kT} \qquad \text{for } r > D/2 \quad . \qquad (\text{B.27})$$

applied in equation B.25 yields the desired interaction for the interaction between salt ions and core particles

$$V_{3j}(r) = \frac{Q\,q_j}{(1+\kappa D/2)}\frac{e^{-\kappa(r-D/2)}}{r} \qquad \text{for } r > D/2 \quad . \qquad (\text{B.28})$$

By using $D = 2\,a$ and $Q = Z$, which is the notation used in section 2.1.3, and putting back l_B, we finally get equation 2.17, which describes the interaction between a charged monomer and one core:

$$V_{\text{cm}}(r) = Z l_B \frac{e^{\kappa a}}{1+\kappa a}\frac{e^{-\kappa r}}{r} \quad . \qquad (\text{B.29})$$

The last remaining task to do is to compute the interaction amongst the core particles. This will be done in the next section.

B.4 Interaction of colloidal particles

In the case of the core-core interaction, equation B.15 has to be solved. Analogous to equation B.27 we can write

$$h_{33}(r) \approx -\frac{V_{33}(r)}{kT} = -\frac{w_{33}(r)}{kT} \qquad \text{for } r > D \qquad (\text{B.30})$$

when using the mean sphere approximation. The corresponding closure relations are in this case

$$c_{33}(r) = -Q^2\frac{1}{r} \qquad \text{for } r > D \qquad (\text{B.31})$$

$$h_{33}(r) = -1 \qquad \text{for } r < D \quad . \qquad (\text{B.32})$$

By applying them in equation B.15 we obtain

$$h_{33}(r) = -\frac{w_{33}(r)}{kT} = -\frac{Q^2}{kT}\frac{1}{r} + \sum_{k=1}^{2}\rho_k \int h_{3k}(|r-r'|)c_{k3}(r')dr' \qquad \text{for } r > D \qquad (\text{B.33})$$

where h_{3k} and c_{k3} are the results from the equations B.25 and B.26, respectively. Finally, by using the same analysis as by obtaining the equations B.25 and B.26, we get the result

$$V_{33}(r) = w_{33}(r) = \frac{Q^2}{(1 + \kappa D/2)^2} \frac{e^{-\kappa(r-D)}}{r} \qquad \text{for } r > D \quad . \tag{B.34}$$

Using the notation from section 2.1.3 and l_B, we finally get equation 2.16, which describes the core-core interaction:

$$V_{cc}(r) = Z^2 l_B \frac{e^{2\kappa a}}{(1 + \kappa a)^2} \frac{e^{-\kappa r}}{r} \quad . \tag{B.35}$$

B The Debye-Hückel Theory

C Fit functions and parameters

In this appendix the fit functions $f_\kappa(x)$ for the force fit for the multi-chain model are presented. For each values of κ ten sets of data were produced, the resulting fit parameters are also tabulated here.

$\kappa = 0.2 \ \sigma^{-1}$:

$$f(x) = \frac{a + bx + cx^2}{1 + dx^2} \exp(mx)$$

a	b	c	d	m
12.9658	5.92551	-2.97243	0.0210881	-0.539500
12.8664	7.82366	-3.47135	0.0344458	-0.540079
13.2843	4.56831	-2.22543	0.0068880	-0.564507
14.4910	-5.45426	0.326390	0.0488500	-0.108881
13.5433	8.88779	-4.06855	0.0205875	-0.605049
13.0299	6.52403	-3.13286	0.0549676	-0.478248
13.1339	5.33845	-2.88847	0.0363655	-0.473782
13.6354	3.34166	-2.29562	0.0899598	-0.397946
14.1753	6.71193	-3.67403	0.0359525	-0.567802
12.8538	5.69793	-2.87028	0.0291177	-0.528898

$\kappa = 0.3 \ \sigma^{-1}$:

$$f(x) = a + bx^2 \exp(mx)$$

a	b	m
11.5702	-0.860432	-0.479839
11.0119	-0.803320	-0.455269
10.5970	-0.572533	-0.445440
10.8411	-1.00904	-0.497306
10.9077	-0.731522	-0.464454
11.8498	-0.914075	-0.489443
12.1388	-0.910436	-0.506669
11.3395	-0.860077	-0.472293
10.8505	-0.796293	-0.488027
12.5783	-1.06858	-0.5251450

C Fit functions and parameters

$\kappa = 0.4 \ \sigma^{-1}$:

$f(x) = a + bx^2 \exp(mx)$

a	b	m
8.71756	-0.539813	-0.420449
9.13542	-0.554371	-0.428946
8.64511	-0.577621	-0.422804
9.29454	-0.734043	-0.503144
9.08536	-0.636210	-0.464171
8.94787	-0.538415	-0.424573
8.86288	-0.665290	-0.437953
8.58309	-0.528360	-0.465464
9.33563	-0.547414	-0.473850
8.47211	-0.581500	-0.494981

$\kappa = 0.6 \ \sigma^{-1}$:

$f(x) = a + bx^2 \exp(mx)$

a	b	m
5.29245	-0.289448	-0.422386
5.35447	-0.288945	-0.422498
5.11516	-0.267327	-0.429623
4.95162	-0.252450	-0.435586
5.14753	-0.252766	-0.434270
5.52607	-0.302447	-0.417221
5.15364	-0.270175	-0.428528
5.32499	-0.288675	-0.422544
5.07671	-0.329609	-0.424397
4.95338	-0.233740	-0.441908

Bibliography

[1] S. MANGENOT, A. LEFORESTIER, P. VACHETTE, AND F. LIVOLANT. 'Salt-induced conformation and interaction changes of nucleosome core particles'. *Biophys. J.*, **82**; p. 345, 2002.

[2] S. MANGENOT, E. RASPAUD, C. TRIBET, L. BELLONI, AND F. LIVOLANT. 'Interaction between isolated nucleosome core particles: A tail-bridging effect?' *Eur. Phys. J.*, **7**; p. 221, 2002.

[3] B. MERGELL, H. SCHIESSEL, AND R. EVERAERS. 'Influence of the nucleosome interaction on the elasticity of chromatin fibers'. *to appear in Phys. Rev. E*.

[4] R. PODGORNICK. 'Two-body polyelectrolyte-mediated bridging interactions'. *JCP*, **118**; p. 11286, 2003.

[5] L. P. LANDAU AND E. M. LIFSCHITZ. *Lehrbuch der theoretischen Physik, Bd. V Statistische Physik Teil 1*. Technische Universität Dresden, 1987.

[6] F. THOMA, T. KOLLER, AND A. KLUG. 'Involvement of histone-H1 in the organization of the nucleosome and of the salt-dependent superstructures of chromatin'. *J. Cell. Biol.*, **83**; p. 403, 1979.

[7] J. WIDOM. 'Physicochemical studies of the folding of the 100-A nucleosome filament into the 300-A filament - cation dependence'. *J. Mol. Biol.*, **190**; p. 411, 1986.

[8] J. T. FINCH AND A. KLUG. 'Solenoidal model for superstructure in chromatin'. *Proc. Natl. Acad. Sci. USA*, **73**; p. 1897, 1976.

[9] J. WIDOM AND A. KLUG. 'Structure of the 300 A chromatin filament - X-ray-diffraction from oriented samples'. *Cell*, **43**; p. 207, 1985.

[10] J. BEDNAR, R. A. HOROWITZ, S. A. GRIGORYEV, L. M. CARRUTHERS, J. C. HANSEN, AND C. L. WOODCOCK. 'Nucleosomes, linker DNA, and linker histone form a unique structural motif that directs the higher-order folding and compaction of chromatin'. *Proc. Natl. Acad. Sci.*, **95**; p. 14173, 1998.

[11] R. A. HOROWITZ, D. A. AGARD, J. W. SEDAT, AND C. L. WOODCOCK. 'The 3-dimensional architecture of chromatin in-situ - electron tomography reveals fibers composed of a continuously variable zigzag nucleosomal ribbon'. *J. Cell. Biol.*, **125**; p. 1, 1994.

Bibliography

[12] S. H. LEUBA, G. YANG, C. ROBERT, B. SAMORI, K. VAN HOLDE, AND C. BUSTAMANTE. '3-dimensional structure of extended chromatin fibers as revealed by tapping-mode scanning force microscopy'. *Proc. Natl. Acad. Sci. USA*, **91**; p. 11621, 1994.

[13] H. SCHIESSEL, W. M. GELBART, AND R. F. BRUINSMA. 'DNA folding: Structural and mechanical properties of the two-angle model for chromatin'. *Biophys. J.*, **80**; p. 1940, 2001.

[14] C. L. WOODCOCK, S. A. GRIGORYEV, R. A. HOROWITZ, AND N. WHITATKER. 'A chromatin folding model that incorporates linker variability generates fibers resembling the native structures'. *Proc. Natl. Acad. Sci. USA*, **90**; p. 9021, 1993.

[15] H. SCHIESSEL. 'Physics of Chromatin'. *J. Phys.: Condens. Matter*, **15**; p. 699, 2003.

[16] B. ALBERS, D. BRAY, J. LEWIS, M. RAFF, K. ROBERTS, AND J. D. WATSON. *Molecular biology of the cell*. Garland Publishing, 1994.

[17] P. J. HORN AND C. L. PETERSON. 'Chromatin higher order folding: Wrapping up transcription'. *Science*, **297**; p. 1824, 2002.

[18] S. GRIGORYEV, J. BEDNAR, AND C. L. WOODCOCK. 'MENT, a heterochromatin that mediates higher order chromatin folding, is a new serpin family member'. *JBC*, **274**; p. 5626, 1999.

[19] J. C. EISSENBERG AND S. C. ELGIN. 'The HP1 protein family: getting a grip on chromation'. *Curr. Opin. Genet. Devel.*, **10**; p. 204, 2000.

[20] T. JENUWEIN AND C. D. ALLIS. 'Translating the histone code'. *Science*, **293**; p. 1074, 2001.

[21] E. PENNISI. 'Behind the scenes of gene expression'. *Science*, **293**; p. 1064, 2001.

[22] J. M. HARP, B. L. HANSON, D. E. TIMM, AND G. J. BUNICK. 'Asymmetries in the nucleosome core particle at 2.5 angstrom resolution'. *Acta Cryst. D*, **56**; p. 1513, 2000.

[23] K. LUGER, A. W. MÄDER, R. K. RICHMOND, D. F. SARGENT, AND T. J. RICHMOND. 'Crystal structure of the nucleosome core particle at 2.8 å resolution'. *Nature*, **389**; p. 251, 1997.

[24] P. D. CARY, T. MOSS, AND E. M. BRADBURY. 'High-resolution proton-magnetic-resonance studies of chromatin core part'. *Eur. J. Biochem.*, **89**; p. 475, 1978.

[25] P. R. HILLARD, R. M. SMITH, AND R. L. RILL. 'Natural abundance carbon-13 nuclear magnetic resonance studies of histone and DNA dynamics in nucleosome cores'. *J. Biol. Chem.*, **261**; p. 5992, 1986.

[26] R. M. SMITH AND R. L. RILL. 'Mobile histone tails in nucleosomes - assignments of mobile segments and investigations of their role in chromatin folding'. *J. Biol. Chem.*, **264**; p. 10574, 1989.

[27] S. N. KHRAPUNOV, A. I. DRAGAN, A. V. SIVOLOB, AND A. M. ZAGARIYA. 'Mechanisms of stabilizing nucleosome structure. study of dissociation of histone octamer from dna'. *Biochim. Biophys. Acta*, **1351**; p. 213, 1997.

[28] D. M. J. LILLEY, J. R. PARDON, AND B. M. RICHARDS. 'Structural investigations of chromatin core protein by nuclear magnetic resonance'. *Biochemistry*, **16**; p. 2853, 1977.

[29] S. ICHIMURA, K. MILTA, AND M. ZAMA. 'Essential role of arginine residues in the folding of deoxyribonucleic acid into nucleosome cores'. *Biochemistry*, **21**; p. 5329, 1982.

[30] J. K. STRAUSS AND L. J. MAHER. 'DNA bending by asymmetric phosphate neutralization'. *Science*, **266**; p. 1829, 1994.

[31] S. Y. PARK, R. F. BRUINSMA, AND W. M. GELBART. 'Spontaneous overcharging of macro-ion complexes'. *Europhys. Lett.*, **54**; p. 454, 1999.

[32] E. GUROVITCH AND P. SENS. 'Adsorption of polyelectrolyte onto a colloid of opposite charge'. *Phys. Rev. Lett.*, **82**; p. 339, 1999.

[33] E. M. MATEESCU, C. JEPPESEN, AND P. PINCUS. 'Overcharging of a spherical macroion by an oppositely charged polyelectrolyte'. *Europhys. Lett.*, **46**; p. 493, 1999.

[34] V. I. PEREL AND B. I. SHKLOVSKII. 'Screening of a macroion by multivalent ions: a new boundary condition for the Poisson-Boltzmann equation and charge inversion'. *Physica A*, **274**; p. 446, 1999.

[35] A. Y. GROSBERG, T. T. NGUYEN, AND B. I. SHLOVSKII. 'The physics of charge inversion in chemical and biological systems'. *Rev. Mod. Phys.*, **74**; p. 329, 2002.

[36] R. MESSINA, C. HOLM, AND K. KREMER. 'Strong attraction between charged spheres due to metastable ionized states'. *PRL*, **85**; p. 872, 2000.

[37] R. MESSINA, C. HOLM, AND K. KREMER. 'Strong electrostatic interactions in spherical colloidal systems'. *Phys. Rev. E*, **64**; p. 021405, 2001.

[38] W. H. BRAUNLIN, T. J. STRICK, AND M. T. RECORD. 'Equilibrium dialysis studies of polyamine binding to DNA'. *Biopolymers*, **21**; p. 1301, 1982.

[39] D. HARRIES, S. MAY, W. M. GELBART, AND A. BEN-SHAUL. 'Structure, stability, and thermodynamics of lamellar DNA-lipid complexes'. *Biophys. J.*, **75**; p. 159, 1998.

Bibliography

[40] I. KOLTOVER, T. SALDITT, AND C. R. SAFINYA. 'Phase diagram, stability, and overcharging of lamellar cationic lipid-DNA self-assembled complexes'. *Biophys. J.*, **77**; p. 915, 1999.

[41] D. P. MASCOTTI AND T. M. LOHMANN. 'Thermodynamic extent of counterion release upon binding oligolysines to single-stranded nucleic-acids'. *Proc. Natl. Acad. Sci. USA*, **87**; p. 3142, 1990.

[42] J. O. RÄDLER, I. KOLTOVER, T. SALDITT, AND C. R. SAFINYA. 'Structure of DNA - cationic liposome complexes dna intercalation in multilamenar membranes in distinct interhelical packing regimes'. *Science*, **275**; p. 810, 1999.

[43] M. T. RECORD, C. F. ANDERSON, AND T. M. LOHMANN. 'Thermodynamic analysis of ion effects on binding and conformational equilibria of proteins and nucleic-acids - roles of ion association or release,screening, and ion effects on water activity'. *Q. Rev. Biophys.*, **11**; p. 103, 1978.

[44] P. SENS AND J.-F. JOANNY. 'Counterion release and electrostatic adsorption'. *Phys. Rev. Lett.*, **84**; p. 4862, 2000.

[45] G. S. MANNING. 'Limiting laws and counterion condensation in polyelectrolyte solutions II. self-diffusion of the small ions'. *J. Chem. Phys.*, **51**; p. 954, 1969.

[46] R. F. BRUINSMA. 'Electrostatics of DNA cationic lipid complexes: isoelectric instability'. *Eur. Phys. J. B*, **4**; p. 75, 1998.

[47] H. SCHIESSEL, R. F. BRUINSMA, AND W. M. GELBART. 'Electrostatic complexation of spheres and chains under elastic stress'. *J. Chem. Phys.*, **115**; p. 7245, 2001.

[48] R. R. NETZ AND J.-F. JOANNY. 'Complexation between a semiflexible polyelectrolyte and oppositely charged sphere'. *Macromolecules*, **32**; p. 9026, 1999.

[49] T. T. NGUYEN AND B. I. SHKLOVSKII. 'Overcharging of a macroion by an oppositely charged polyelectrolyte'. *Physica A*, **293**; p. 324, 2001.

[50] T. T. NGUYEN AND B. I. SHKLOVSKII. 'Complexation of a polyelectrolyte with oppositely charged spherical macroions: Giant inversion of charge'. *J. Chem. Phys.*, **114**; p. 5905, 2001.

[51] T. T. NGUYEN AND B. I. SHKLOVSKII. 'Complexation of DNA with positive spheres: Phase diagram of charge inversion and reentrant condensation'. *J. Chem. Phys.*, **115**; p. 7298, 2001.

[52] E. BRAUN, Y. EICHEN, U. SIVAN, AND G. BEN-YOSEPH. 'DNA-templated assembly and electrode attachment of a conducting silver wire'. *Nature*, **391**; p. 775, 1998.

[53] N. GÖTTING, H. FRITZ, M. MAIER, J. VON STAMM, T. SCHOOFS, AND E. BAYER. 'Effects of oligonucleotide adsorption on the physicochemical characteristics of a nanoparticle-based model delivery system for antisense drugs'. *Colloid Polym. Sci.*, **277**; p. 145, 1999.

[54] H. W. WALKER AND S. B. GRANT. 'Factors influencing the flocculation of colloidal particles by a model anionic polyelectrolyte'. *Colloids Surf.*, **119**; p. 229, 1996.

[55] Y. LI, P. DUBIN, H. A. HAVEL, S. L. EDWARDS, AND H. DAUTZENBERG. 'Complex formation between polyelectrolyte and oppositely charged mixed micelles: Soluble complexes vs coacervation'. *Langmuir*, **11**; p. 2486, 1995.

[56] Y. WANG, K. KIMURA, P. L. HUANG, Q DUBIN, AND W. JAEGER. 'Effects of salt on polyelectrolyte-micelle coacervation'. *Macromolecules*, **32**; p. 7128, 1999.

[57] Y. WANG, K. KIMURA, AND P. DUBIN. 'Polyelectrolyte-micelle coacervation: Effects of micelle surface charge density, polymer molecular weight, and polymer/surfactant ratio'. *Macromolecules*, **33**; p. 3324, 2000.

[58] H. M. EVANS, A. AHMAD, T. PFOHL, A. MARTIN-HERRANZ, AND C. R. SAFINYA. 'Charge induced structural transitions of dendrimer: DNA complexes with applications to gene delivery'. *Biophys J*, **80**; p. 2567, 2001.

[59] V. A. KABANOV, V. G. SERGEYEV, O. A. PYSHKINA, A. A. ZINCHENKO, A. B. ZEZIN, J. G. H. JOOSTEN, J. BRACKMAN, AND K. YOSHIKAWA. 'Interpolyelectrolyte complexes formed by DNA and astramol poly(propylene imine) dendrimers'. *Macromolecules*, **33**; p. 9587, 2000.

[60] A. AKINESIA AND P. LINES. 'Monte Carlo simulations of polygon-macroion complexes. 1. Equal absolute polygon and macroion charges'. *Macromolecules*, **35**; p. 5183, 2002.

[61] P. CHODANOWSKI AND S. STOLL. 'Polyelectrolyte adsorption on charged particles in the Debye-Hückel approximation. a Monte Carlo approach'. *Macromolecules*, **34**; p. 2320, 2001.

[62] J. DZUBIELLA, A. G. MOREIRA, AND P. A. PINCUS. 'Polyelectrolyte-colloid complexes: Polarizability and effective interaction'. *Macromolecules*, **36**; p. 1741, 2003.

[63] P. HARONSKA, T. A. VILGIS, R. GROTTENMÜLLER, AND M. SCHMIDT. 'Adsorption of polymer chains onto charged spheres: Experiment and theory'. *Macrom. Theory Simul.*, **7**; p. 241, 1998.

[64] M. JONSSON AND P. LINSE. 'Polyelectrolyte-macroion complexation. I. Effect of linear charge density, chain length and macroion charge'. *J. Chem. Phys.*, **115**; p. 3406, 2001.

[65] M. Jonsson and P. Linse. 'Polyelectrolyte-macroion complexation. II. Effect of chain flexibility'. *J. Chem. Phys.*, **115**; p. 10975, 2001.

[66] R. Messina, C. Holm, and K. Kremer. 'Conformation of a polyelectrolyte complexed to a like-charged colloid'. *Phys. Rev. E*, **65**; p. 41805, 2002.

[67] R. Messina, C. Holm, and K. Kremer. 'Like-charge colloid-polyelectrolyte complexation'. *J. Chem. Phys.*, **117**; p. 2947, 2002.

[68] T. Sakaue, S. H. Yoshikawa, and K. Takeyasu. 'Histone core slips along DNA and prefers positioning at the chain end'. *Phys. Rev. Lett.*, **87**; p. 78105, 2001.

[69] T. Wallin and P. Linse. 'Monte Carlo simulations of polyelectrolytes at charged micelles. 1. Effects of chain flexibility'. *Langmuir*, **12**; p. 305, 1996.

[70] T. Wallin and P. Linse. 'Monte Carlo simulations of polyelectrolytes at charged micelles. 2. Effects of linear charge density'. *J. Phys. Chem.*, **100**; p. 17873, 1996.

[71] T. Wallin and P. Linse. 'Monte Carlo simulations of polyelectrolytes at charged micelles. 3. Effects of surfactant tail length'. *J. Phys. Chem.*, **101**; p. 5506, 1997.

[72] T. Wallin and P. Linse. 'Monte Carlo simulations of polyelectrolytes at charged hard spheres with different numbers of polyelectrolyte chains'. *J. Chem. Phys.*, **109**; p. 5089, 1998.

[73] D. A. Beard and T. Schlick. 'Modelling salt-mediated electrostatics of macromolecules: The discrete surface charge optimization algorithm and its application to the nucleosome'. *Biopolymers*, **58**; p. 106, 2001.

[74] D. A. Beard and T. Schlick. 'Computational modelling predicts the structure and dynamics of chromatin fiber'. *Structure*, **9**; p. 105, 2001.

[75] T. Schneider and E. Stoll. 'Molecular-dynamics study of a three-dimensional one-component model for distortive phase transitions'. *Phys. Rev. B*, **17**; p. 1302, 1978.

[76] B. Dünweg. 'Molecular Dynamics algorithms and hydrodynamic screening'. *J. Chem. Phys.*, **99**; p. 6977, 1993.

[77] D. Frenkel and B. Smit. *Understanding molecular simulation*. Academic press, 2002.

[78] G. S. Grest and K. Kremer. 'Molecular dynamics simulation for polymers in the presence of a heat bath'. *Phys. Rev. A*, **33**; p. 3628, 1986.

[79] J.-P. Hansen and I. R. McDonald. *Theory of simple liquids*. Academic press, 1986.

[80] D. A. MCQUARRIE. *Statistical mechanics*. University Science Books, 2000.

[81] J.-L. BARRAT AND J.-F. JOANNY. 'Theory of polyelectrolyte solutions'. *Adv. Chem. Phys.*, **95**; p. 1, 1996.

[82] E. ALLAHYAROV, H. LÖWEN, A. A. LOUIS, AND J. P. HANSEN. 'Discrete charge patterns, Coulomb correlations and interactions in protein solutions'. *Europhys. Lett.*, **57**; p. 731, 2002.

[83] I. ROUZINA AND V. A. BLOOMFIELD. 'Macroion attraction due to electrostatic correlation between screening counterions. 1. Mobile surface-adsorbed ions and diffuse ion clouds'. *J. Chem. Phys.*, **100**; p. 9977, 1996.

[84] R. MESSINA, C. HOLM, AND K. KREMER. 'Ground state of two unlike charged colloids: An analogy with ionic bonding'. *Europhys. Lett.*, **51**; p. 461, 2000.

[85] H. BOROUDJERI AND R. R. NETZ. 'Interactions between polyelectrolyte-macroion complexes'. *Europhys. Lett.*, **64**; p. 413, 2003.

[86] P. PINCUS. 'Collois stabilization with grafted polyelectrolytes'. *Macromolecules*, **24**; p. 2912, 1991.

[87] M. K. GRANFELDT, B. JÖNNSON, AND C. E. WOODWARD. 'A Monte Carlo simulation study of the interaction between charged colloids carrying adsorbed polyelectrolytes'. *J. Phys. Chem.*, **95**; p. 4819, 1991.

[88] J. ENNIS, L. SJÖSTRÖM, T. ÅKESSON, AND J. BO. 'Attractive osmotic pressure in an electric double layer with grafted polyelectrolytes'. *J. Phys. Chem. B*, **102**; p. 2149, 1998.

[89] M. DOI AND S. F. EDWARDS. *The theory of polymer dynamics*. Oxford Science Publications, 1986.

[90] E. HEITZ. *Jahrb. Wissench. Bot.*, **69**; p. 762, 1928.

[91] M. COCKELL, F. PALLADINO, T. LAROCHE, T. KYRION, C. LIU, A. J. LUSTIG, AND S. M. GASSER. 'The carboxy termini of SIR4 and RAP1 affect SIR3 localization - evidence for a multicomponent complex required for yeast telomeric silencing'. *J. Cell. Biol.*, **129**; p. 909, 1995.

[92] S. C. ELGIN. 'Heterochromatin and gene regulation in Drosophila'. *Curr. Opin. Genetic Devel.*, **6**; p. 193, 1996.

[93] A. HECHT, T. LAROCHE, S. STRAHL-BOLSINGER, S. GASSER, AND M. GRUNSTEIN. 'Histone H3 and H4 N-termini interact with SIR3 and SIR4 proteins - a molecular-model for the formation of heterochromatin in yeast'. *Cell*, **80**; p. 583, 1995.

[94] S. HENIKOFF. 'Nuclear organization and gene expression: Homologous pairing and long-range interactions'. *Curr. Opin. Cell Biol.*, **9**; p. 388, 1997.

Bibliography

[95] A. Lohe and A. J. Hilliker. 'Return of the h-word (heterochromatin)'. *Curr. Opin. Genet. Dev.*, **5**; p. 746, 1995.

[96] M. T. Madireddi, R. S. Coyne, J. F. Smothers, K. M. Mickey, M. C. Yao, and C. D. Allis. 'Pdd1p, a novel chromodomain-containing protein, links heterochromatin assembly and DNA elimination in Tetrahymena'. *Cell*, **87**; p. 75, 1996.

[97] P. B. Singh and N. S. Huskisson. 'Chromatin complexes as aperiodic microcrystalline arrays that regulate genome organisation and expression'. *Dev. Genet.*, **22**; p. 85, 1998.

[98] L. Alland, R. Muhle, H. Hou Jr, J. Potes, L. Chin, N. Schreiber-Agus, and R. A. DePinho. 'Role for N-CORR and histone deacetylase in Sin3-mediated transcriptional repression'. *Nature*, **387**; p. 43, 1997.

[99] T. Heinzel, R. M. Lavinsky, T.-M. Mullen, M. Söderström, C. D. Laherty, J. Torchia, W. M. Yang, G. Brard, S. D. Ngo, J. R. Davie, E. Seto, R. N. Eisenmann, D. W. Rose, C. K. Glas, and M. G. Rosenfeld. 'A complex containing N-CoR, mSin3 and histone deacetylase mediates transcriptional repression'. *Nature*, **387**; p. 49, 1997.

[100] P. Debye and W. Hückel. 'Zur Theorie der Elektrolyte. I. Gefrierpunktserniedrigung und verwandte Erscheinungen'. *Phys. Z.*, **24**; p. 185, 1923.

[101] E. J. W. Verwey and J. T. G. Overbeek. *Theory of the stability of lyophobic colloids*. Dover Publications Inc., 1999.

[102] M. Medina-Noyoloa and D. A. McQuarrie. 'On the interaction of spherical double layers'. *J. Chem. Phys.*, **73**; p. 6279, 1980.

Acknowledgments

First I like to thank Kurt Kremer and Christian Holm, who allowed me to work on this interesting topic.

Furthermore I thank Helmut Schiessel for raising my interest on the exiting field of chromatin physics. He was open to many fruitful discussions and shared his broad knowlegde with me.

I am also grateful to Markus Deserno and Burkhard Dünweg, whose advice helped me out of numerous problems.

Harald Bopp, Thorsten Stühn and the people from the RZG in Garching helped me a lot with the computer equipment, wherefore I like to thank.

Especially I want to thank Zuowei Wang and his family for the friendship and hospitality they offered me. Here I also want to mention Doris Kirsch, who always had an encouraging word for me.

Finally I want to thank the members of my family, who were always there, when I needed them.

Acknowledgments

132

Curriculum Vitae

Personal data

	Frank Mühlbacher
	Nahestraße 2
	55118 Mainz
	born November 7, 1975, in Würzburg

Education

1986-1995	Friedrich-Koenig-Gymnasium Würzburg
	Abitur in June 1995
1996-1999	studies of physics at the Julius-Maximilians-Universität Würzburg
1999-2001	studies of physics at the State University of New York at Stony Brook, USA
	graduation in May 2001 (M.A.)
2000-2001	Graduate Research Assistant of the State University of New York at Stony Brook
2001-2004	doctorate at the Max-Planck-Institute for polymer research, Mainz
	graduation in July 2004 (PhD; Dr. rer. nat.)